Master's thesis

NTNU
Norwegian University of Science and Technology
Faculty of Engineering
Department of Marine Technology

Mahé Hermile

# Atmospheric Stability Effects on a Spar-Type Floating Wind Turbine

Master's thesis in Wind Energy
Supervisor: Erin Bachynski-Polić
Co-supervisor: Axelle Viré
August 2021

NTNU
Norwegian University of Science and Technology

TU Delft
Delft University of Technology

Mahé Hermile

# Atmospheric Stability Effects on a Spar-Type Floating Wind Turbine

Master's thesis in Wind Energy
Supervisor: Erin Bachynski-Polić
Co-supervisor: Axelle Viré
August 2021

Norwegian University of Science and Technology
Faculty of Engineering
Department of Marine Technology

NTNU
Norwegian University of
Science and Technology

Master of Science Thesis

# Atmospheric Stability Effects on a Spar-Type Floating Wind Turbine

Mahé Hermile

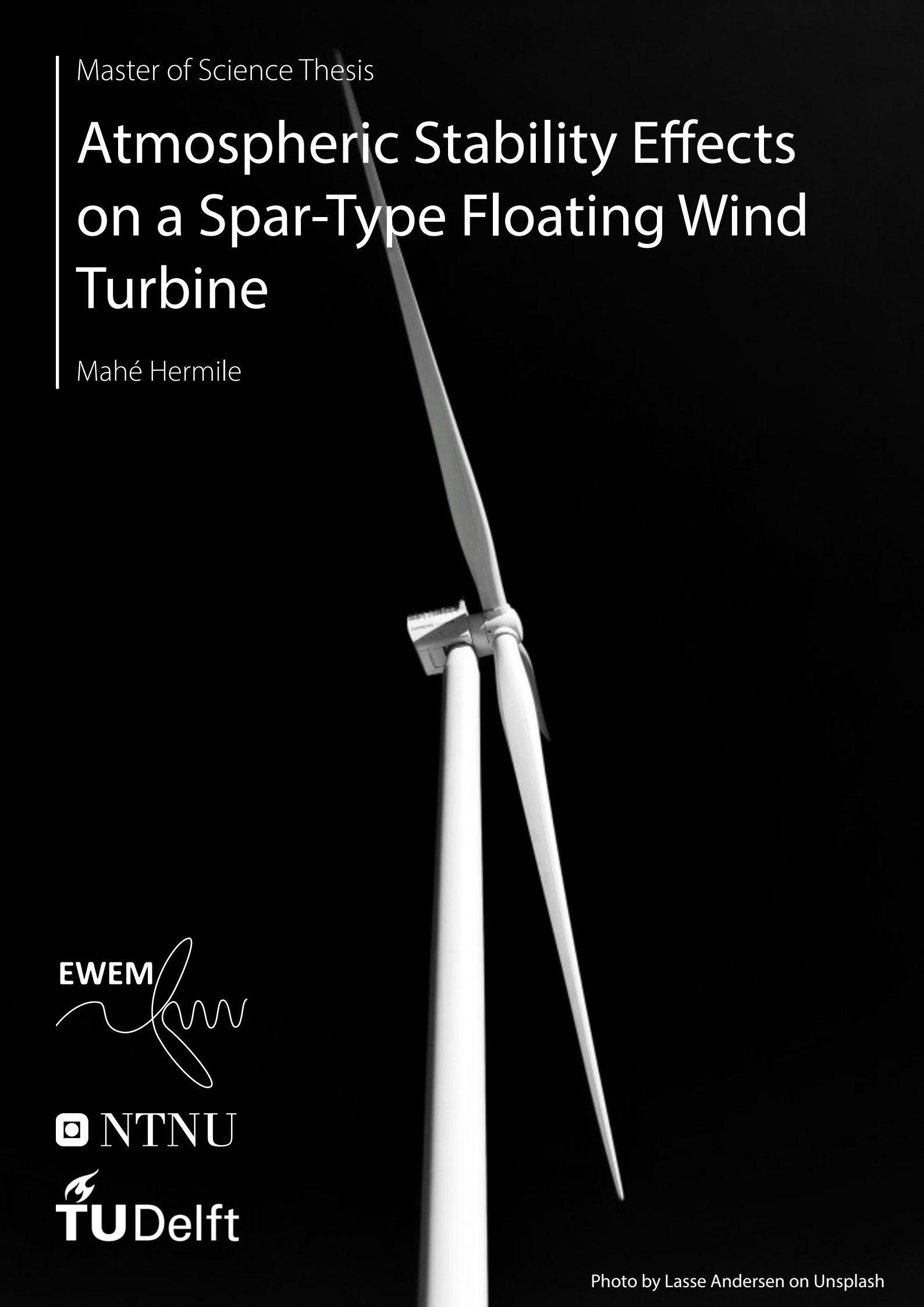

EWEM

NTNU

TUDelft

Photo by Lasse Andersen on Unsplash

# Abstract

Simulations of a spar-type floating wind turbine supporting the DTU 10 MW reference turbine[1] under fitted atmospheric conditions are performed. Atmospheric conditions are modelled using the turbulent models recommended by the IEC:[2] the Mann model and the IEC Kaimal and exponential coherence model. Model parameters are fitted to measurements at the FINO-1 platform[3] to generate turbulent boxes that are as close as possible to measurements. The simulations are carried out using OpenFAST[4] for three mean wind speeds: 7.5, 12 and 16 m/s and the power law wind profile is used with fitted shear exponent. The motions, wind, loads spectra are quantified using the WAFO toolbox and the loads are assessed with short-term damage-equivalent loads using MLife.[5] Depending on the wind model, global motions differ by up to 52%. Generally, Kaimal resulted in higher surge and pitch motions, and the opposite was found for the yaw motions. The influence of atmospheric stability on global motions was found to be important as well, unstable conditions giving the largest motions and stable conditions the lowest. It was observed that the wind model influenced the fairlead tension and tower top loads. Mann resulted in up to 35% higher loads on the tower top yaw moment and Kaimal resulted in up to 30% higher fairlead tension loads. Tower base fore-aft bending moment and blade root out-of-plane moment were not very sensitive to the choice of wind model. Atmospheric stability had an influence on all loads by up to 30%. Unstable conditions led to the most damage while stable conditions generally led to the least. Whether the choice of the wind model or the change in atmospheric stability has more influence on the global motions of the platform and the loads depended on the wind speed, the degree of freedom or the load considered. It was found that wind models should always consider atmospheric conditions, not only neutral. Finally, impact of Mann turbulence model parameter variations on the wind, global motions and loads was investigated. It was found that turbulence intensity is influenced by the three parameters and has a bigger impact than the differences in coherence.

# Acknowledgements

I would like to express my gratitude to all the professors from the Technical University of Denmark (DTU), Delft University of Technology (TU Delft), and the Norwegian University of Science and Technology (NTNU) I had the chance to discuss with and learn from during the European Wind Energy Master (EWEM).
I am also very thankful for my two supervisors for this work, Professor Erin Bachynski-Polić of NTNU and Professor Axelle Viré who provided me with great expertise, kindness and passion. Their patience and abundant knowledge was key to the success of this thesis.
I would like to thank Irene Rivera Arreba for her incredible help during this thesis. She gave very useful insights and discussion that helped me understood my work better.
Finally, I would like to extend my appreciation for RAVE as data was made available by the RAVE (research at alpha ventus) initiative, which was funded by the German Federal Ministry of Economic Affairs and Energy on the basis of a decision by the German Bundestag and coordinated by Fraunhofer IWES (see: www.rave-offshore.de).

# Contents


**I Introduction** **10**
- I.1 Background . . . 10
- I.2 Research Objectives and Questions . . . 12
- I.3 Thesis Structure . . . 12

**II Theory** **14**
- II.1 Atmospheric Boundary Layer . . . 14
  - II.1.1 Atmospheric stability and turbulence . . . 15
  - II.1.2 Wind profiles . . . 17
  - II.1.3 Turbulence . . . 19
  - II.1.4 Offshore atmospheric stability . . . 21
- II.2 Turbulence models . . . 22
  - II.2.1 Mann uniform shear model . . . 23
  - II.2.2 Kaimal spectrum and coherence model . . . 25
  - II.2.3 Coherence . . . 25
  - II.2.4 Atmospheric stability effect on the two turbulence models . . . 27
- II.3 Floating wind turbine dynamics . . . 28
  - II.3.1 Effects of turbulence model choice on FWT . . . 28
  - II.3.2 Effects of atmospheric stability on wind turbines . . . 29

**III Floater** **31**
- III.1 Spar . . . 33
- III.2 Natural frequencies study . . . 34

**IV Environmental conditions** **35**
- IV.1 Wave . . . 35
- IV.2 Wind . . . 36
  - IV.2.1 FINO-1 platform available data . . . 36
  - IV.2.2 Data processing . . . 37
  - IV.2.3 Atmosphere stability classification . . . 39
  - IV.2.4 Power law fitting . . . 39
  - IV.2.5 High-frequency extraction . . . 40
  - IV.2.6 Standard deviation computation . . . 41
  - IV.2.7 Mann parameters . . . 43
  - IV.2.8 Coherence fitting . . . 44

**V Modeling** **49**
- V.1 OpenFAST . . . 49
- V.2 Inflow turbulence generation . . . 49

V.2.1 TurbSim . . . 50
V.2.2 DTU 64bit turbulence generator . . . 51
V.2.3 Size of the box . . . 51
V.2.4 Mann model . . . 52
V.2.5 Kaimal model . . . 53
V.2.6 TIMESR . . . 53
V.3 Response . . . 53
V.3.1 Spectra computation . . . 53
V.3.2 Fatigue analysis . . . 53
V.4 Summary . . . 54

**VI Results** **56**
VI.1 Wind fields . . . 56
VI.1.1 Wind spectra . . . 58
VI.1.2 Wind coherence . . . 61
VI.1.3 Lateral coherence . . . 64
VI.2 Global motions . . . 66
VI.2.1 Influence of the turbulence model . . . 66
VI.2.2 Influence of atmospheric stability . . . 69
VI.2.3 Design standard models or stability conditions . . . 70
VI.3 Load response . . . 72
VI.3.1 Influence of the turbulence model . . . 72
VI.3.2 Influence of atmospheric stability . . . 75
VI.3.3 Design standard models or stability conditions . . . 76
VI.4 Mann parameters sensitivity analysis . . . 77
VI.4.1 Influence of $\alpha\epsilon^{2/3}$ . . . 77
VI.4.2 Influence of $L$ . . . 80
VI.4.3 Influence of $\Gamma$ . . . 83

**VII Conclusions and recommendations** **87**
VII.1 Conclusions . . . 87
VII.2 Recommendations . . . 89

**A Spar decay tests** **91**

**B Wind spectra** **92**

**C Coherence** **95**

**D Quad-coherence** **98**

**E Lateral coherence** **100**

**F PSDs motions** **102**

**G Platform motion percent differences for stability conditions** **104**

**H Damage equivalent loads with filtering** **105**

**Bibliography** **105**

# List of Figures


I.1 *Evolution of distance to shore and depth of offshore wind farms throughout the years*[6] . . 11

II.1 *Atmosphere vertical structure*[7] . . . . . 14
II.2 *Wind profiles for different atmospheric stability*[8] . . . . . 16
II.3 *Turbulence intensity depending on wind speed at 90 m height for the period September 2003 – August 2007 by Tuerk et al.*[9] . . . . . 20
II.4 *Turbulence intensity as a function of wind speed for two different design standards*[10,2] . . 20
II.5 *Distribution of observations by stability class sampled by hour of the day, month, wind direction and wind speed at the FINO-1 offshore platform*[11] . . . . . 21
II.6 *Distribution of atmospheric stability as a function of wind speed at FINO-1 with different classification method* . . . . . 22
II.7 *Distribution at three offshore sites (a-c) and an onshore site (d)*[12] . . . . . 23
II.8 *Coherence between two points (0,119) and ($\delta_y$, 119) at a fixed x-plane in the u-velocity direction for the IEC Model at 16m/s* . . . . . 26
II.9 *Three main floating wind turbine concepts*[13] . . . . . 29

III.1 *Computational model of the spar with lines representing the blades visualized in MATLAB. The tower and rotor are colored in black while the hydrodynamic members are colored in yellow* . . . . . 32
III.2 *Mooring system layout for the floater*[14] . . . . . 33
III.3 *Floating support structure stability triangle*[15] . . . . . 34
III.4 *Decay test for the spar floater surge motion* . . . . . 34

IV.1 *Map of FINO-1*[3] . . . . . 36
IV.2 *Map of data usage* . . . . . 38
IV.3 *Atmosphere stability distribution* . . . . . 39
IV.4 *Wind profile for each wind speed of interest at hub height and atmospheric stability. The circles represent the cup anemometers measurements* . . . . . 40
IV.5 *Power law coefficient statistical variation as a function of wind speed. The dark shapes denote the average of the cases while the transparent diamonds denote the different cases* 41
IV.6 *High-frequency measurements extraction* . . . . . 41
IV.7 *Turbulence intensity as a function of wind speed and stability conditions* . . . . . 42
IV.8 *Mann parameters as a function of wind speed and atmospheric stability* . . . . . 44
IV.9 *Statistical variation of the Mann parameters. The transparent diamonds denote the different cases* . . . . . 45
IV.10 *Mann parameters as a function of height from de Maré*[16] . . . . . 46
IV.11 *IEC coherence model for all components as a function of wind speed and stability conditions* 47
IV.12 *Davenport coherence model for all components as a function of wind speed and stability conditions* . . . . . 48

V.1 *OpenFAST organization* . . . 50
V.2 *TurbSim computational time as a function of grid dimension, by Bonnie Jonkman*[17] . . . 51
V.3 *Work objectives* . . . 54
V.4 *Simulations for each work objective* . . . 55

VI.1 *Longitudinal standard deviation as a function of wind speed and atmospheric conditions. The triangle shape represent the target standard deviation and the transparent shapes denote the different seeds* . . . 57
VI.2 *Lateral standard deviation as a function of wind speed and atmospheric conditions. The triangle shape represent the target standard deviation* . . . 58
VI.3 *Vertical standard deviation as a function of wind speed and atmospheric conditions. The triangle shape represent the target standard deviation* . . . 59
VI.4 *Power spectral density at hub centre at 12 m/s mean wind speed* . . . 60
VI.5 *Wind speed at hub height in stable conditions for a 12 m/s mean wind speed* . . . 61
VI.6 *Coherence of three velocity components between hub height and 20 meters below the hub at 12 m/s as a function of reduced frequency* . . . 62
VI.7 *Quad-coherence in the longitudinal direction between hub height and 20 meters below the hub at 12 m/s as a function of reduced frequency* . . . 64
VI.8 *Lateral coherence in the longitudinal direction at 1/2 diameter separation distance at 12 m/s as a function of reduced frequency* . . . 64
VI.9 *Lateral quad-coherence in the longitudinal direction at 1/2 diameter separation distance at 12 m/s as a function of reduced frequency* . . . 65
VI.10 *Platform pitch, surge, and yaw motion standard deviations as a function of* $\overline{u}_{hub}$ . . . 66
VI.11 *Platform roll, sway and heave motion standard deviations as a function of* $\overline{u}_{hub}$ . . . 68
VI.12 *Platform motions PSDs at 16 m/s* . . . 69
VI.13 *Platform pitch, surge, and yaw motion percent difference standard deviations between stability conditions and neutral conditions as a function of* $\overline{u}_{hub}$ . . . 70
VI.14 *Platform pitch, surge, and yaw motion percent difference standard deviations between wind models as a function of* $\overline{u}_{hub}$ . . . 71
VI.15 *Damage-equivalent loads as a function of* $\overline{u}_{hub}$ . . . 72
VI.16 *Mooring line 2 tension spectra at each wind speed* . . . 73
VI.17 *Tower base fore-aft bending moment spectra at each wind speed* . . . 73
VI.18 *Tower top yaw moment spectra at each wind speed* . . . 74
VI.19 *Blade root out-of-plane moment spectra at each wind speed* . . . 74
VI.20 *Damage-equivalent loads percent difference between stability conditions and neutral conditions for all generation methods at each wind speed* . . . 75
VI.21 *Damage-equivalent loads percent difference between Kaimal and Mann for all stability conditions at each wind speed* . . . 77
VI.22 *Influence of* $\alpha\epsilon^{2/3}$ *on the longitudinal standard deviation* . . . 78
VI.23 *Influence of* $\alpha\epsilon^{2/3}$ *on the power spectral density at hub centre* . . . 78
VI.24 *Influence of* $\alpha\epsilon^{2/3}$ *on the lateral coherence of the longitudinal wind component between (0,0,119) and (0,89.15,119)* . . . 79
VI.25 *Influence of* $\alpha\epsilon^{2/3}$ *on the platform pitch, surge and yaw motions* . . . 79
VI.26 *Influence of* $\alpha\epsilon^{2/3}$ *on the platform motion responses* . . . 79
VI.27 *Influence of* $\alpha\epsilon^{2/3}$ *on the damage-equivalent loads* . . . 80
VI.28 *Influence of* $L$ *on the longitudinal standard deviation* . . . 80
VI.29 *Influence of* $L$ *on the power spectral density at hub centre* . . . 81
VI.30 *Influence of* $L$ *on the lateral coherence of the longitudinal wind component between (0,0,119) and (0,89.15,119)* . . . 81
VI.31 *Influence of* $L$ *on the platform pitch, surge and yaw motions* . . . 82

VI.32 *Influence of $L$ on the platform motion responses* . . . 82
VI.33 *Influence of $L$ on the damage-equivalent loads* . . . 83
VI.34 *Influence of $\Gamma$ on the longitudinal standard deviation* . . . 83
VI.35 *Influence of $\Gamma$ on the power spectral density at hub centre* . . . 84
VI.36 *Influence of $\Gamma$ on the lateral coherence of the longitudinal wind component between (0,0,119) and (0,89.15,119)* . . . 84
VI.37 *Influence of $\Gamma$ on the platform pitch, surge and yaw motions* . . . 85
VI.38 *Influence of $\Gamma$ on the platform motion responses* . . . 85
VI.39 *Influence of $\Gamma$ on the damage-equivalent loads* . . . 86

A.1 *Heave spar decay test* . . . 91
A.2 *Sway spar decay test* . . . 91

B.1 *Power spectral density at hub centre at 7.5 m/s mean wind speed* . . . 93
B.2 *Power spectral density at hub centre at 7.5 m/s mean wind speed* . . . 94

C.1 *Coherence in three directions between hub height and 20 meters below the hub at 7.5 m/s as a function of reduced frequency* . . . 96
C.2 *Coherence in three directions between hub height and 20 meters below the hub at 16 m/s as a function of reduced frequency* . . . 97

D.1 *Quad-coherence in the longitudinal direction between hub height and 20 meters below the hub at 7.5 m/s as a function of reduced frequency* . . . 98
D.2 *Quad-coherence in the longitudinal direction between hub height and 20 meters below the hub at 16 m/s as a function of reduced frequency* . . . 99

E.1 *Lateral coherence in the longitudinal direction at 1/2 diameter separation distance at 7.5 m/s as a function of reduced frequency* . . . 100
E.2 *Lateral coherence in the longitudinal direction at 1/2 diameter separation distance at 16 m/s as a function of reduced frequency* . . . 101

F.1 *Platform motions PSDs at 7.5 m/s* . . . 102
F.2 *Platform motions PSDs at 12 m/s* . . . 103

G.1 *Platform roll, sway, and heave motion percent difference standard deviations between stability conditions and neutral conditions as a function of $\overline{u}_{hub}$* . . . 104

H.1 *Damage-equivalent loads in the low frequency range as a function of $\overline{u}_{hub}$* . . . 105
H.2 *Damage-equivalent loads in the low frequency range plus the wave frequency as a function of $\overline{u}_{hub}$* . . . 106

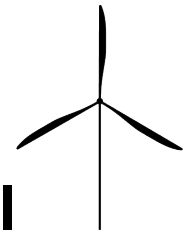

# CHAPTER I

# Introduction

## I.1 Background

The global wind power capacity has reached 623 GW in 2019[18] and 5% of it has been produced by offshore wind turbines. Although this part is small, the offshore sector has increased its capacity by a factor of 13 in the last decade while the onshore sector has increased its capacity by a factor of 4.[18] While increasing the offshore sector capacity, offshore wind farm distance to shore increases every year (Figure I.1a). With increasing distance to shore, water depth increases (Figure I.1b) leading to bigger and more expensive bottom-fixed structures.

In areas with deep water depth but large wind resources, floating wind turbines have been developed to tackle the water depth issue. Different type of floating wind turbines (FWTs) have been modeled or manufactured, such as semi-submersibles, spars and tension-leg platforms and so far, two full-scale floating wind farms have been installed: Hywind Scotland[19] with spar-type floaters and WindFloat Atlantic in Portugal[20] with two semi-submersible floaters. One of the structural differences between bottom-fixed turbines and floating wind turbines resides in the natural periods. Since FWTs have greater natural periods, they become more influenced by the low frequency part of the wind spectrum.

Design innovations have allowed wind turbine to be exposed to higher wind speeds at higher altitudes. As a consequence, wind turbines are more exposed to different atmospheric conditions (unstable, neutral or stable). Previous research has shown the influence of atmospheric conditions on wind turbine loads.[12,21] Sathé et al.[12] found that atmospheric stability could have a strong effect on the loads on a fixed wind turbine. Doubrawa et al.[21] performed simulations using computational fluid dynamics (CFD) solver Simulator fOr Wind Farm Applications (SOWFA) to study the effect of turbulent atmospheric flows on a spar floater and found that loads on the mooring system are most sensitive to atmospheric stability in low winds and that loads on the blade root are most sensitive to atmospheric stability in high winds. More recently, Jacobsen and Godvik[22] showed, based on measurements at Hywind Scotland, that a decrease in FWT motions happened with stable atmospheric conditions.

Two wind models are recommended by the standards for the design of offshore wind turbines:[2] the Kaimal spectrum and coherence model (hereinafter called "Kaimal") and the Mann model (hereinafter

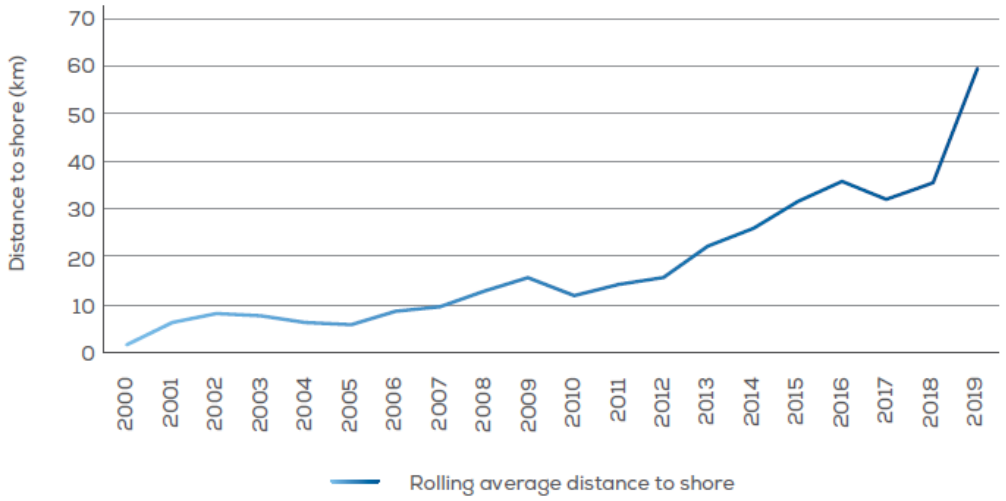


(a) *Rolling average distance to shore, from the 2019 Offshore Wind in Europe*[6]

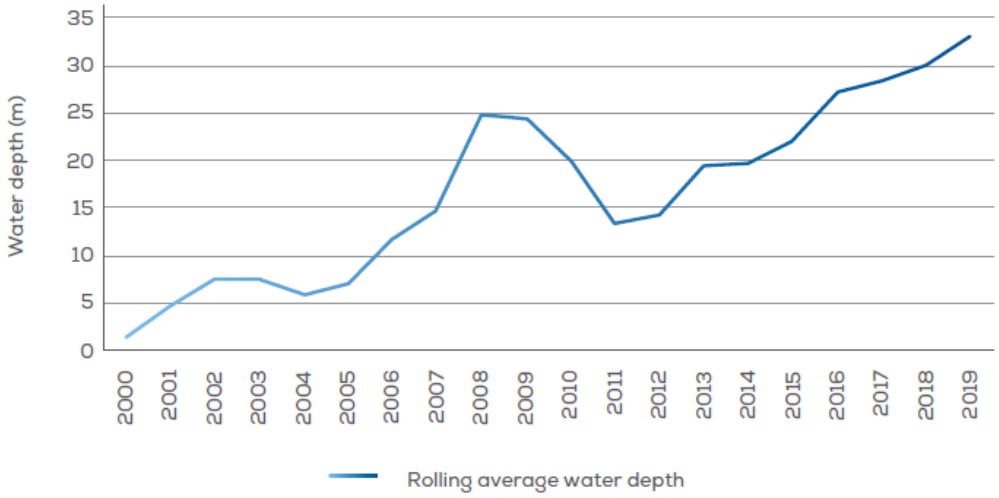


(b) *Rolling average water depth, from the 2019 Offshore Wind in Europe*[6]

Figure I.1: *Evolution of distance to shore and depth of offshore wind farms throughout the years*[6]

called "Mann"). Although both models should give similar results for onshore or bottom-fixed turbines, uncertainties and differences in load responses have been found for floating wind turbines. Bachynski and Eliassen[23] found that the most differences in the FWT motion responses were in the low-frequency range. While the Kaimal model gave larger surge and pitch responses, the Mann model resulted in larger yaw, sway and roll responses. The explanation was found in the coherent structures differences between the two models. Furthermore, increased mooring line fatigue on a spar FWT design has been found by Godvik[24] when using the Mann model.

While both models give different results, they both assume neutral atmospheric stratification. However, atmospheric stability influences the turbulence intensity or the behaviour of eddies structures in the atmosphere. Typically, the more stable the atmosphere, the lower the turbulence and the smaller the eddies. Peña[25] showed a fit of the Mann model parameters to atmospheric conditions to match required atmospheric stability. This was achieved by spectral analysis of time series of wind speed fluctuations measured over flat and homogeneous terrain in Denmark. Even though these measurements were made onshore, Peña's work gives an idea on how to derive the parameters for the required atmospheric condition. To match different atmospheric stability conditions, Nybø[26] used data from the FINO-1 platform to fit Kaimal and Mann models to measurements. Turbulence intensities and wind profiles were fitted to the measurements for each stability condition and wind speed studied. Re-

cently, Cheynet[27] developed an algorithm that fit the Mann model parameters to measurements in the least-square sense.

The need for models that fit offshore conditions arises and this thesis proposes a fit of the Mann and Kaimal models parameters. This fit allows for a turbulent box generation that is close to what can be found offshore.

## I.2 Research Objectives and Questions

Differences in atmospheric stability lead to different responses for bottom-fixed turbines and spar-type FWTs. Kaimal and Mann models, although recommended by the standards, give different global responses. To understand the impact of wind models and atmospheric stability on FWT dynamics, the main research question of this work is raised:

*"To what extent does atmospheric stability influence floating wind turbines dynamics?"*

This question can be divided in three other questions

1. To what extent are wind fields influenced by wind models and atmospheric stability?
2. To what extent are FWT dynamics influenced by wind models?
3. To what extent are FWT dynamics influenced by atmospheric stability? i.e. How important is atmospheric stability for wind turbine loads/motions?
4. How does lateral coherence influence FWT loads?
5. Is changing the atmospheric stability more influential than the choice of the wind model?
6. How does each Mann parameter influence the FWT dynamics?

From these questions and the literature, six objectives can be defined:

1. To confirm the differences between Kaimal and Mann models and compare with what was found in the literature,[28,29]
2. To generate accurate turbulent wind fields that match specific atmospheric conditions based on measurements,
3. To assess the impact of atmospheric stability on a spar-type floater and compare the results with literature,[22]
4. To assess the impact of lateral coherence on FWT dynamics,
5. To estimate how much atmospheric stability should be taken into account when modelling and designing FWTs,
6. To perform an accurate sensitivity analysis of the Mann parameters.

## I.3 Thesis Structure

This paper is divided into three parts. The first part provides the required background information such as relevant literature and explanation of the different concepts. A general introduction to wind energy, turbulence, atmospheric stability and turbulence models is provided in Chapter II. The floater is subsequently presented in Chapter III. The second part focuses on the generation of the wind fields and the OpenFAST files. The generation of the environmental conditions is explained in Chapter IV.

Chapter V presents how the OpenFAST simulation were done. Finally, conclusions are drawn and recommendations for future research are presented in Chapter VII.

# CHAPTER II

# Theory

This chapter defines the concepts related to the atmospheric boundary layer. First, a presentation of the ABL is proposed in Section II.1. The two main wind profiles are then presented, a definition of how turbulence is treated is proposed and atmospheric stability is presented. Then, the different models are presented in Section II.2: Mann and Kaimal.

## II.1 Atmospheric Boundary Layer

The lowest portion of the atmosphere is called the atmospheric boundary layer (ABL). Its thickness is variable in space and time. Typically occupying the bottom 10 to 20% of the troposphere (1 to 2 km), it can range from tens of meters to 4 km or more.[30]

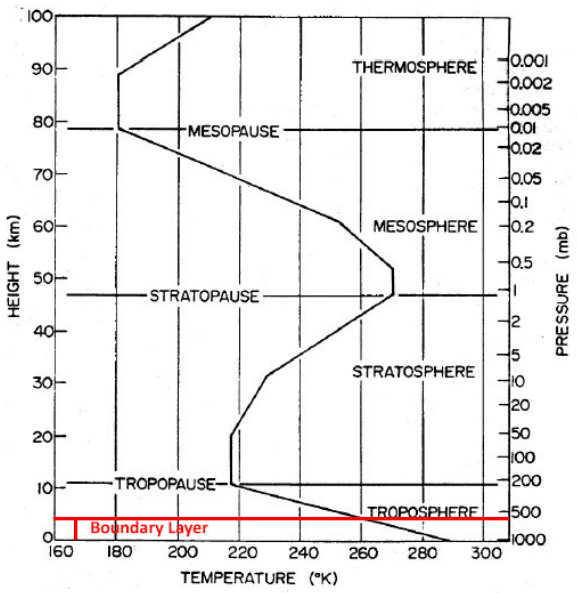


Figure II.1: *Atmosphere vertical structure*[7]

This layer is particularly influenced by the Earth's surface. It is characterized by well developed turbulence generated by frictional drag as the atmosphere moves across the surface of the Earth, and by a thermal mixing from the heated surface. The Earth surface roughness, characterized by the roughness length ($z_0$), influences the ABL thickness: a greater roughness leads to a thicker ABL. The ABL thickness is also influenced by the atmospheric stability; the more positive the heat flux, the thicker the ABL.[31]

## II.1.1 Atmospheric stability and turbulence

Atmospheric stability is related to heat flux direction and height. The stability of the air is how it responds to small disturbances. The atmosphere stability can be classified in three categories: neutral, stable, unstable.

- **Neutral stratified atmosphere** typically occurs during strong winds, on a cloudy day or twilight. The air parcel that is disturbed from its location will then stay at its new position leading to little temperature change at the surface.
- With **stable atmospheric condition**, once disturbed, the air parcel will return to its original position. This typically occurs at nighttime when the ground is cool. In this case, turbulence is mechanically-generated and balanced by negative buoyancy.
- In an **unstable atmospheric condition**, the air parcel will continue to move away once disturbed. It occurs when the ground is hotter than the air above, typically during daytime, this will produce positive buoyancy.

Related to turbulence, unstable atmospheric conditions have the most turbulence compared to neutral and stable atmospheric conditions. Both high turbulence and unstable atmosphere are correlated with higher positive heat flux.

Commonly, the atmospheric stability is described by the Obukhov length $L$.[32] The length scale is used to classify the atmospheric stability and is defined as the height above the surface where thermally-(or buoyancy-) generated turbulence dominates over mechanically-generated turbulence. It is the ratio of the shear friction effect to the buoyancy effect. A negative value implies unstable atmosphere and buoyancy-generated turbulence, while a positive value classifies a stable atmosphere with mechanically-generated turbulence. The Obukhov length is defined as:

$$L = \frac{-\overline{\theta_v} u_*^3}{\kappa g (\overline{w'\theta'})_s} \tag{II.1}$$

where $(\overline{w'\theta'})_s$ is the surface kinematic eddy heat flux, $\overline{\theta_v}$ is the virtual potential temperature, $u_*^3$ the friction velocity defined as $u_* = \sqrt{\overline{u'w'}^2 + \overline{v'w'}^2}$, $g$ the gravitational acceleration, and where the apostrophe denotes the fluctuation.

The stability classification based on this parameter varies in the litterature. Gryning et al.[33] proposed the classification presented in Table II.1.

In the case of buoyancy-generated turbulence, the wind shear gradient will be the lowest, typically in unstable conditions. The opposite is true under stable conditions. This difference in wind shear gradient shows the influence of atmospheric stability on the wind speed profile as seen in Figure II.2.

| Stability | Range [m] |
|---|---|
| Very stable | $10 < L < 50$ |
| Stable | $50 < L < 200$ |
| Near stable | $200 < L < 500$ |
| Neutral | $\|L\| > 500$ |
| Near unstable | $-500 < L < -200$ |
| Unstable | $-200 < L < -100$ |
| Very unstable | $-100 < L < -50$ |

Table II.1: *Stability classification based on Obukhov length*[33]

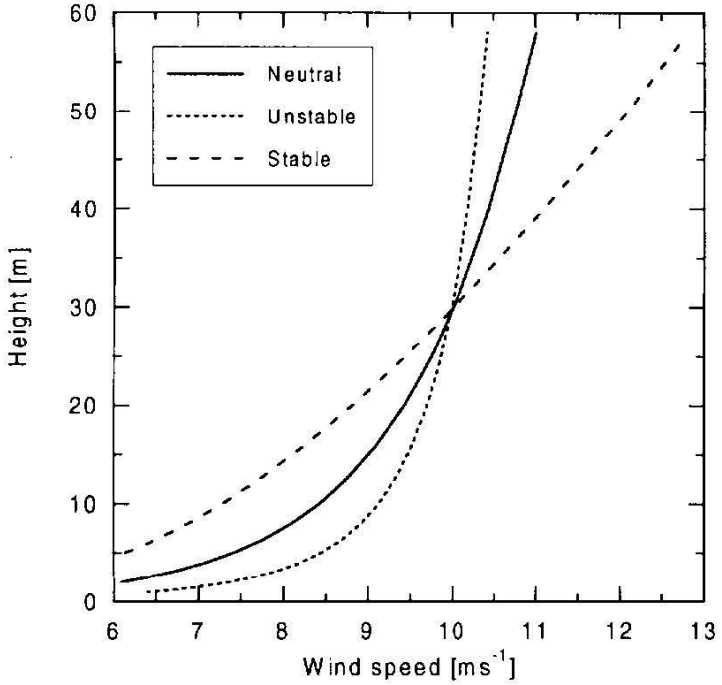


Figure II.2: *Wind profiles for different atmospheric stability*[8]

DNV-RP-C205 standard[34] presents a simpler form to obtain the Obukhov length based on the Richardson number, $R_i$.[35]

$$R_i = \frac{z}{L} \cdot \frac{1}{\varphi} \tag{II.2}$$

where $\varphi$ is the non-dimensional temperature profile and should be determined from empirical data. The profile is a function of $\xi = z/L$. The Richardson number is defined as:

$$R_i = \frac{g}{\rho_0} \frac{\frac{d\rho_0}{dz}}{\left(\frac{dU}{dz}\right)^2} \tag{II.3}$$

where $\rho_0$ is the unperturbed density, $\frac{d\rho_0}{dz}$ is the vertical density gradient and $\frac{dU}{dz}$ is the vertical gradient of the horizontal wind speed. Table II.2 presents the relation between the Richardson number and the Obukhov length.

| **Stability conditions** | Stable | Neutral | Unstable |
|---|---|---|---|
| $\xi$ | $\xi > 0$ | $\xi = 0$ | $\xi < 0$ |
| **Richardson number** | $0 < R_i < 0.2$ | - | $R_i < 0$ |
| **Obukhov length** | $L = z\left(\frac{1-5R_i}{R_i}\right)$ | - | $L = \frac{z}{R_i}$ |

Table II.2: *Relation between Obukhov length and Richardson number as a function of stability conditions*[34]

Another classification used in this work is the gradient Richardson number, $R_{ig}$,[35] defined as:

$$R_{ig} = \frac{g}{\overline{T}} \frac{(\Delta\theta/\Delta z)}{(\Delta u/\Delta z)^2} \tag{II.4}$$

where $\theta$ is the potential temperature and $\overline{T}$ is the mean temperature. $\Delta$ denotes a variation of the variable at different heights. The conditions were then classified by Golder[36] according to stability classes using the limits shown in Table II.3.

| **Atmospheric stability** | **Gradient Richardson Number** |
|---|---|
| Very unstable | $R_{ig} < -5.34$ |
| Unstable | $-5.32 \leq R_{ig} < -2.26$ |
| Weakly unstable | $-2.26 \leq R_{ig} < -0.569$ |
| Neutral | $-0.569 \leq R_{ig} < 0.083$ |
| Weakly stable | $0.083 \leq R_{ig} < 0.196$ |
| Stable | $0.196 \leq R_{ig} < 0.49$ |
| Very stable | $0.49 \leq R_{ig}$ |

Table II.3: *Stability classification gradient Richardson number*[36]

In the thesis, *unstable conditions* will denote the union of "very unstable", "unstable" and "weakly unstable" conditions and *stable conditions* will denote the union of "very stable", "stable" and "weakly stable" conditions.

## II.1.2 Wind profiles

The horizontal velocity of air flow near the surface is near zero and will change with height: it is defined as a wind profile. Obstacles on the surface and heat fluxes create a sheared profile causing atmospheric turbulence. Wind speed consists of a mean part and a fluctuating part (turbulence) but the wind speed profile representation is expressed using the mean part only.

In the wind energy field, two wind profile models are recommended by design standards:[2] the power law and the logarithmic law. They are both valid in the *surface layer* which accounts for about 10% of the ABL. When these models were developed, most of the wind turbines operated in this layer, now most of them operate above. Besides, the surface layer height will vary according to atmospheric stability and will be even smaller over sea as more neutral conditions are present offshore. Larsen et al.[37] found that the wind above the surface layer had a tendency to increase more than logarithmically as a result of either the boundary length scale or the influence of atmospheric stability. This calls for an extended wind profile. Furthermore, the power law and the logarithmic law are both valid for neutral atmospheric conditions and have been developed with onshore measurements. Offshore design standards[2] still recommend these two profiles.

## Power law

Due to its practicality, the power law is used in many wind engineering applications.[35] It is defined as:

$$U(z) = U_{ref}\left(\frac{z}{z_{ref}}\right)^{\alpha} \tag{II.5}$$

where $U_{ref}$ is the undisturbed mean wind speed at a reference height, $z_{ref}$, and $\alpha$ is the power law or shear exponent. The shear exponent accounts for both atmospheric stability and roughness length. Typically, higher values of $\alpha$ denote higher shear observed in stable conditions. This model assumes neutral stability based on a constant roughness length of 0.002 m to be used over the sea. The power law exponent is given by the standards[2] as $\alpha = 0.14$ for all wind speeds and for both onshore and offshore conditions. In this thesis, a fit will be performed to compute the power law exponent for each stability conditions at each hub height mean wind speeds.

## Logarithmic wind profile

The logarithmic wind profile originates from a similarity theory[38] in meteorology. It is expressed as:

$$U(z) = \frac{u_*}{\kappa}\left[\ln\left(\frac{z}{z_0}\right) - \psi\right] \tag{II.6}$$

where $u_*$ denotes the friction velocity, $\kappa$ the von Kármán constant, $z_0$ the surface roughness length, and $\psi$ is a function used to account for non-neutral conditions and will be discussed below. In neutral conditions, the function is zero.

## Atmospheric stability in wind profiles

Standard wind models (Kaimal and Mann, ref section II.1.2) assume neutral stability conditions. However, as shown in Figure II.5, neutral conditions are not representative offshore, therefore stability should be implemented in wind profile models, turbulence intensity, and wake calculation. In the power law the $\alpha$ exponent accounts for the effect of surface roughness $z_0$, and the atmospheric stability.[10] However, it is important to distinguish both for offshore conditions as the roughness length varies. As shown in Equation II.6, the logarithmic law separates the atmospheric stability and roughness length. The $\psi$ function depends on the sign of $\xi$ and takes different values for different stability conditions as shown in Table II.4.

| Atmospheric stability | Stability-dependent function value |
|---|---|
| Stable ($\xi > 0$) | $\psi = -4.8\xi$ |
| Neutral | $\psi = 0$ |
| Unstable ($\xi < 0$) | $\psi = 2\ln(1+x) + \ln(1+x^2) - 2\tan^{-}1(x)$ |

Table II.4: *Stability-dependent function values*[34]

Even though this thesis will use a surface-layer model (power law), the limits of these models should be presented. The importance of using a boundary-layer wind profile model has been highlighted in Sathe et al.[12] work. They observed that if blade and rotor loads, particularly for stable sites, are calculated assuming only the surface-layer wind profile model, the calculated blade and rotor loads will be larger in comparison with those obtained using a boundary-layer wind profile model. The main cause of this increase in loading is the infinite increase of the wind profile length scale in the surface-layer wind profile model, leading to large wind gradients. The boundary-layer wind profile model by Gryning et

al.[33] limits the growth of this length scale using the boundary layer height, leading to smaller wind shear in comparison with the surface-layer model.

## II.1.3 Turbulence

Atmospheric turbulent flow is a superposition of irregular swirls of many scales. These swirls are also called eddies. The large eddies are broken down into smaller eddies, a process called turbulent cascade[30] where some of the large eddies energy is transferred to the smaller eddies. Turbulence can be generated by frictional drag (mechanical turbulence) and by thermal mixing from the Earth surface (thermal turbulence). Mechanical turbulence happens when there is shear in the wind that can be caused by frictional drag which causes a lower wind speed near the ground. Its intensity increases with surface roughness length and wind speed but decreases with height.[39] Thermal turbulence happens because of temperature gradients. It consists of warm air that rises or cold air that sinks because of buoyancy forces.

### Turbulence intensity

The wind speed fluctuation about its mean value is measured by turbulence intensity. Considering a component of the wind (longitudinal, lateral and vertical), turbulence intensity is defined as the ratio of the standard deviation to the mean velocity for the time period and height chosen. Design standards[2] recommend conservative turbulence intensity values depending on the wind turbine class and the hub height wind speed. These values correspond to the $90^{th}$ percentile of turbulence intensity in neutral conditions. According to the IEC standards,[2] the longitudinal standard deviation is defined as:

$$\sigma_1 = I_{ref}(0.75U_{hub} + b) \tag{II.7}$$

where $I_{ref}$ denotes the turbulence intensity value at 15 m/s (see Table II.5), $b$ denotes a constant taken as 5.6 m/s.

| **Wind turbine class** | $I_{ref}$ |
|---|---|
| A | 0.16 |
| B | 0.14 |
| C | 0.12 |
| S | Specified by the designer |

Table II.5: *Turbulence intensity values according to wind turbine class (IEC 61400-1)[2]*

This IEC standard[2] turbulence intensity formulation corresponds to onshore neutral conditions and assumes the turbulence intensity to decrease while asymptotically approaching a constant value with increasing wind speed. Offshore, specifically at FINO-1, turbulence intensity decreases towards a minimum then increases (see Figure II.3).

IEC 61400-3[10] suggest a modification of Equation II.7 for offshore conditions:

$$\sigma_1 = \frac{U_{hub}}{\ln(z_{hub}/z_0)} + 1.28 \cdot d \cdot I_{ref} \tag{II.8}$$

where $z_0$ denotes the surface roughness, $d$ is a constant taken as 4 m/s. The surface roughness is derived from the Charnock expression for near-neutral atmospheric conditions:

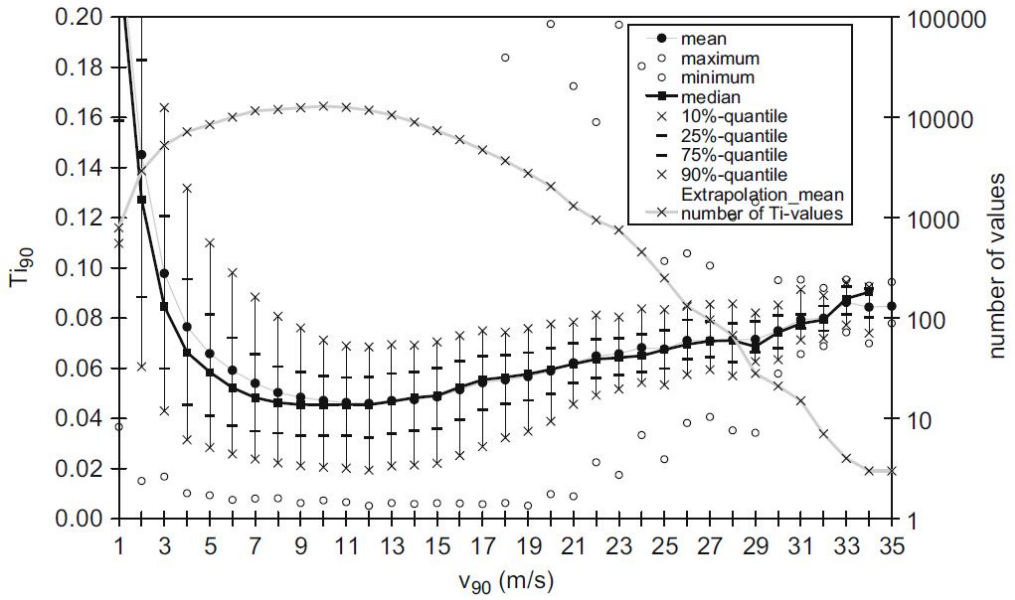


Figure II.3: *Turbulence intensity depending on wind speed at 90 m height for the period September 2003 – August 2007 by Tuerk et al.*[9]

$$z_0 = \frac{A_c}{g}\left[\frac{\kappa \cdot U_{hub}}{\ln(z_{hub}/z_0)}\right]^2 \tag{II.9}$$

where $\kappa$ denotes the von Karman's constant (0.4), and $A_c$ the Charnock's constant taken as 0.011 for open sea.

Figure II.4 shows a comparison of Equation II.8 and II.7 with the same $I_{ref} = 0.12$ at $z_{hub} = 119$ meters.

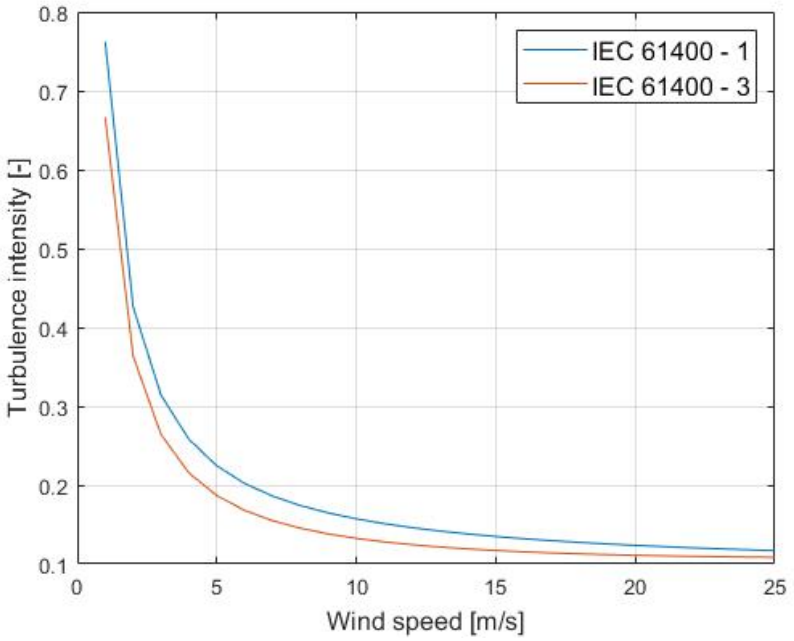


Figure II.4: *Turbulence intensity as a function of wind speed for two different design standards*[10,2]

From Figure II.4, it can be seen that offshore turbulence intensity is lower than onshore turbulence

intensity but follows the same logarithmic decrease with increasing wind speeds. The choice of either of the formulation for our work is explained in Section IV.2.

### II.1.4 Offshore atmospheric stability

Onshore, a given site is associated to a constant roughness hence a constant friction velocity for a fixed wind speed. It allows the atmospheric boundary layer to be defined with stationary parameters. Offshore, the air-water interface (waves) is a function of time and space. This variability induces a characterisation of the atmospheric boundary layer by non-stationary parameters. Waves give friction to the wind, changing the wind profile. This friction is characterized by the surface roughness $z_0$. The higher the surface roughness, the more mechanically-generated turbulence dominates, hence the more neutral conditions dominate.[40] The DNV-RP-C205 standard[34] recommends a $z_0$ value between 0.0001 and 0.001 meters for open sea with waves. This is a first limitation of the wind models developed for onshore sites but used offshore: with small values of $z_0$ the surface layer extends less, increasing the chance of having the wind turbine rotor above it.

Furthermore, offshore, atmospheric stability is more sensitive to seasonal cycles. Barthelmie et al.[11] found a dominance of stable atmospheric conditions in the spring and unstable atmospheric conditions in fall, as shown in Figure II.5.

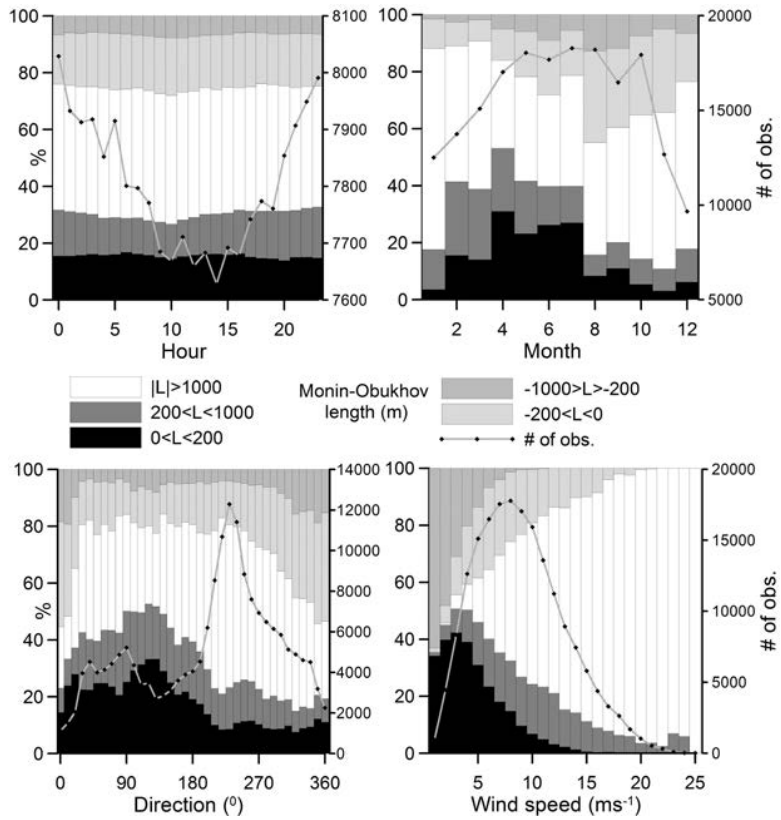


Figure II.5: *Distribution of observations by stability class sampled by hour of the day, month, wind direction and wind speed at the FINO-1 offshore platform*[11]

#### Measurements

The North Sea is where most of the measurements related to offshore wind energy come from. Sathé et al.,[12] Nybø et al.[41] and Obhrai et al.[42] studied the influence of different wind fields on wind turbines with wind measurements in the North Sea. Figure II.6 shows the distribution of stability as a function of wind speed at FINO-1 using different classification methods.

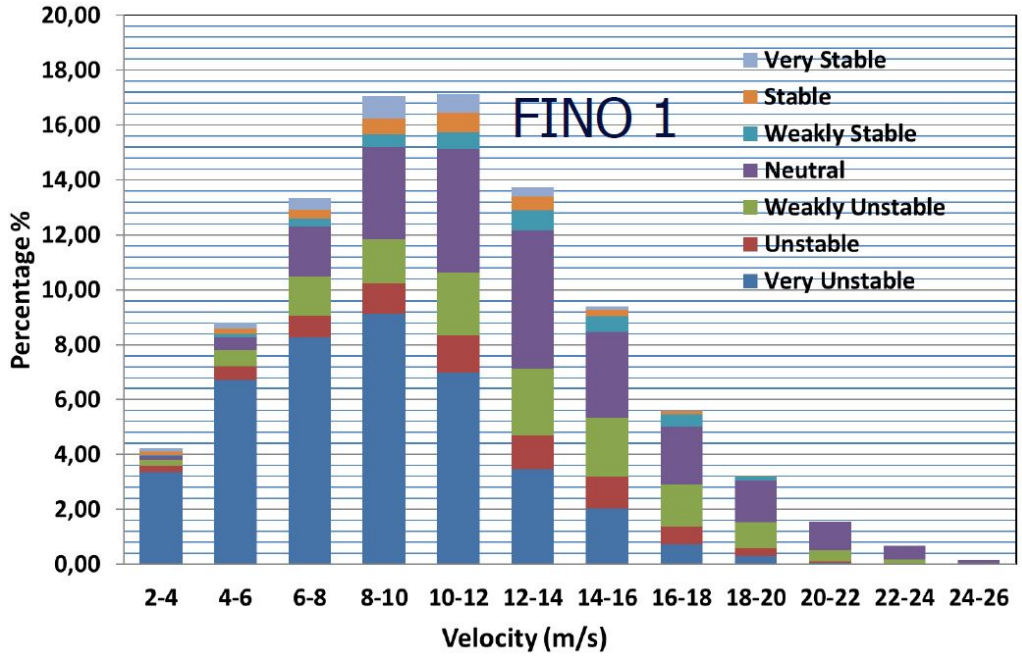


(a) *Distribution at FINO-1 using gradient Richardson number classification*[42]

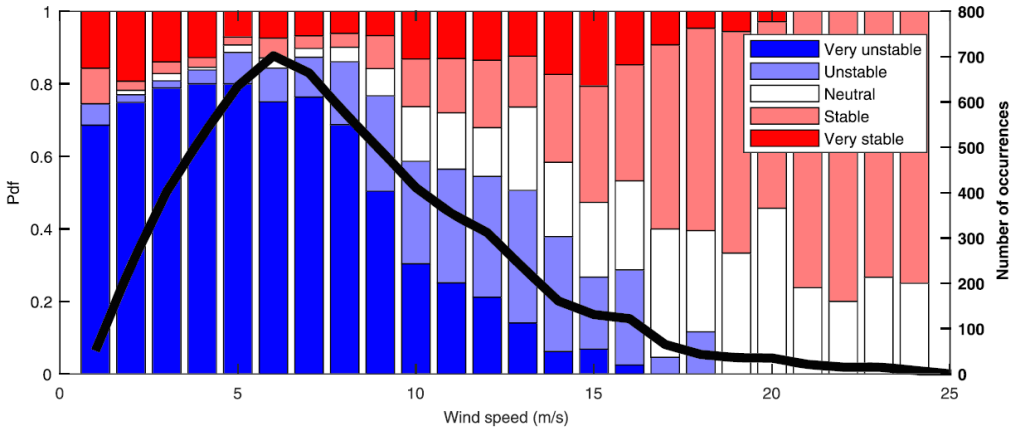


(b) *Distribution at FINO-1 using Obukhov length classification*[41]

Figure II.6: *Distribution of atmospheric stability as a function of wind speed at FINO-1 with different classification method*

The measurements presented in the work of Nybø et al. (Figure II.6b) and Obhrai et al. (Figure II.6a) correspond to the FINO- 1 platform, located in the North Sea. It is observed that with increasing wind speeds, neutral conditions dominate, whereas for lower wind speeds, unstable conditions dominate. The shift in the wind distribution peak might be due to the fact that the time periods selected were different. Data from Sathé et al. (Figure II.7) correspond to three offshore wind farms and one onshore. The findings for offshore sites are consistent with the observations at FINO-1: as wind speed increases, near-neutral conditions dominate. These observations could be related to the fact that with high wind speeds waves are higher hence the surface roughness. Therefore, more mechanically-generated turbulence than buoyant-generated turbulence would be present, meaning stable conditions govern.

## II.2 Turbulence models

The International Electrotechnical Commission recommends the use of two turbulence models.[2] One is the Kaimal spectral and exponential coherence model,[43] the other is the Mann spectral model,[44,45]

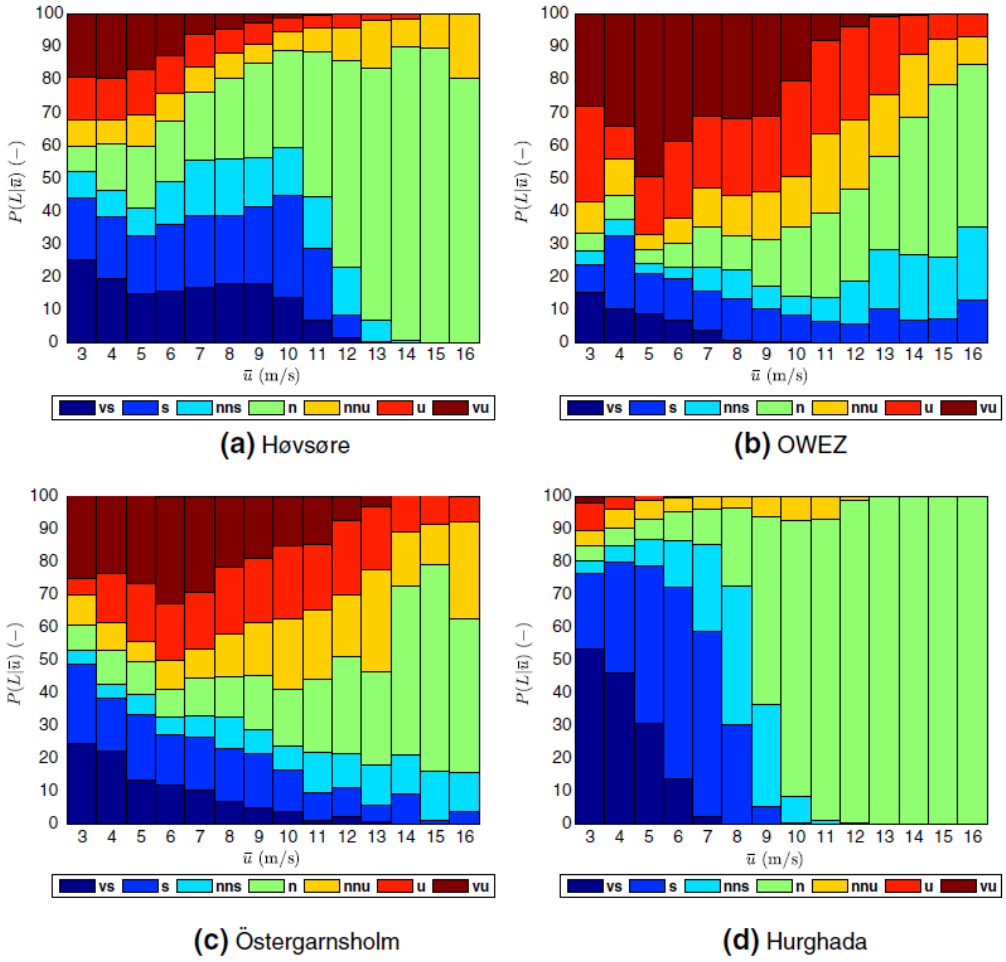


Figure II.7: *Distribution at three offshore sites (a-c) and an onshore site (d)*[12]

hereafter denoted as Kaimal and Mann, respectively. The frequency content of Mann and Kaimal follow that of the Kaimal spectrum[2] (Equation II.13). The two models are defined differently: Kaimal defines turbulence by a one-point spectrum and a coherence function, while Mann takes advantage of spectral velocity tensor. Both simulated wind fields, from the use of these turbulence models, can provide similar information about turbulent wind spectra, but the coherence between points in the fields may differ.

Studies investigated the performances of these models and how they affect the dynamics of offshore wind turbines.[29,28] It has been concluded that, as the models differ in the representation of turbulent structures, the impact on the offshore wind turbines will be slightly different.

Both models are included with standardized parameters[2] and are developed for small onshore wind turbines. The different representation of spatial distribution of turbulence was not crucial for small turbine rotors, but as the size of the wind turbines rotor increases, the need for accurate wind models follows.

## II.2.1 Mann uniform shear model

Mann[44,45] developed a spectral tensor turbulence model which can be used to simulate wind fields with particular turbulence characteristics.[25] Thus, it is now used for inflow turbulence generation with the DTU Mann 64bit turbulence generator.[46] The Mann model looks at the spectral tensor of atmospheric turbulence at neutral stability state. It contains all information on spectra, cross-spectra and coherences

that are required for engineering applications in wind energy, and is defined as:

$$\phi_{ij}(k) = \frac{1}{(2\pi)^2} \int R_{ij}(r) \exp(-ik \cdot r) dr \tag{II.10}$$

where,

$$\int dr = \int_{-\infty}^{\infty} \int_{-\infty}^{\infty} \int_{-\infty}^{\infty} dr_1 dr_2 dr_3$$

and $R_{ij}(r)$ denotes the covariance between time series $u_i$ and $u_j$ at a separation $r$ and $k$ is the wave vector. The velocity field can be defined as:

$$u(x) = \int \exp(ik \cdot x) dZ(k) \tag{II.11}$$

where $Z$ is a stochastic vector field with uncorrelated increments connected to the spectral tensor via Equation II.12:

$$\langle dZ_i^*(k) dZ_j(k) \rangle = \phi_{ij}(k) dk_1 dk_2 dk_3 \tag{II.12}$$

where $^*$ denotes complex conjugation. Cross-spectra and relation to the Mann coherence will be discussed in the Mann coherence subsection.

The model involves three adjustable parameters:

- $\alpha\epsilon^{2/3}$ is the measure of *dissipation rate* at which wind turbulence kinetic energy (TKE) is converted to heat as the eddies break down into smaller eddies.
- $L$, a length scale that defines the *size of the turbulent eddies* with the most energy. It characterizes the atmospheric stability condition. Higher values of L imply higher energy in the low frequency range.[47]
- $\Gamma$, a non-dimensional parameter to estimate the *eddy lifetime*. This parameter describes shear deformation of turbulence eddies, and also affects the ratio between the standard deviations of the wind speed in $u-$, $v-$ and $w-$ directions. A positive value of $\Gamma$ results in larger ratio between the three directional turbulence ($\sigma_u^2 > \sigma_v^2 > \sigma_w^2$).

The Mann model assumes neutral atmospheric stability but these parameters can be modified to match a corresponding stability. Sathe et al.[12] investigated the influence of atmospheric stability on wind turbine loads of a fixed turbine by fitting the Mann model to site-specific parameters including atmospheric stability and Peña et al.,[25] proposed a way to modify the Mann model to account for atmospheric stability.

The IEC standard[2] suggests fitted values, presented in Table II.6, that were obtained by fitting the Mann model to the Kaimal spectra. The length scale increases linearly with height up to 60 meters, but remains constant above that height. The IEC standard[2] recommends a $\Gamma$ parameter value of 3.9 while measurements onshore by Sathe et al.[12] found values closer to $\Gamma = 3.16$.

The selection of these parameters for the different stability conditions will be discussed in Section IV.2.

| $\alpha\epsilon^{2/3}$ | $L$ | $\Gamma$ |
|---|---|---|
| $\frac{55}{18} \cdot 0.4754 \cdot \sigma_{iso}^2 \cdot L^{-2/3}$<br><br>where $\sigma_{iso} = 0.55 \cdot \sigma_1$ | L = $\begin{cases} 0.56z & z < 60 \text{ m} \\ 33.6 & z \geq 60 \text{ m} \end{cases}$ | 3.9 |

Table II.6: Standard Mann model parameters. $z$ denotes the wind turbine hub height.

## II.2.2 Kaimal spectrum and coherence model

Another turbulent wind model that will be used is the Kaimal spectrum with exponential coherence model, referred to here as Kaimal.[43] The generated turbulent wind field according to IEC Kaimal spectrum & coherence model is computed based on the calculated Kaimal Spectrum (Equation II.13) in the longitudinal, lateral, and vertical directions; respectively u-, v- and w-components. The computed synthetic wind field is assumed stationary with zero-mean Gaussian process.[2]

$$\frac{fS_K(f)}{\sigma_K^2} = 4\frac{\frac{fL_K}{U_{hub}}}{1 + 6\frac{fL_K}{U_{hub}}} \tag{II.13}$$

where f is the frequency, $S_K(f)$ is the one-sided wind spectrum, $\sigma_K$ is the standard deviation of the wind velocity, $U_{hub}$ is the wind speed at hub height, $L_K$ is the wind integral scale parameter and K = u, v or w refers to the specific velocity component. Parameter values can be found in IEC 61400-1.[2] TurbSim,[48] by NREL, will be used to generate the inflow turbulence.

## II.2.3 Coherence

As said before, both Mann and Kaimal follow the frequency content of the Kaimal spectrum but differ in the spatial variation. Cross-spectra provide information on how mutually coherent velocity fluctuations are at two points. The spectra consist of two parts, a real-part, the co-spectrum capturing the different frequency component appearances, and an imaginary part (quad-coherence) capturing the phases between these points. Saranyasoontorn & Veers[49] show that the imaginary part was negligible for bottom founded turbines but Nybø[26] show that the non-negligible quad-coherence leads to a phase shift that will have an impact on the dynamic response of offshore wind turbines. The high importance of lateral coherence of the longitudinal wind component ($u$) (over that of $v$ or $w$) on bottom-fixed wind turbine loads was observed in a sensitivity study[50] performed with the Kaimal model.

Coherence is the normalized cross-spectrum but the term coherence will now refer to the co-coherence, the cross-spectrum real part's normalized form. For two spatially separated processes *i* and *j*, the magnitude-squared coherence is defined as:

$$\gamma_{i,j_K}(f) = \frac{|S_{ij}|}{\sqrt{S_i(f) \cdot S_j(f)}} \tag{II.14}$$

### IEC Kaimal coherence

Within the Kaimal model, coherence is added to the generated points using an exponential functions based on empirical formulations.[2] It is defined as:

$$\gamma_{i,j_K}(\delta, f) = \exp\left(-a_K\sqrt{\left(\frac{f\delta}{\overline{u}_{hub}}\right)^2 + (\delta b_K)^2}\right) \tag{II.15}$$

where $\delta$ is the separation distance between time-series *i* and *j*, $a_K$ is the coherence decrement parameter and $b_K$ is the coherence offset parameter. Nonetheless, in the IEC standard, the coherence model is only applied to the u-velocity component and does not provide values of $a_K$ and $b_K$ for the lateral and vertical velocity components.

| **Parameters** | $a_u[-]$ | $b_u[m^{-1}]$ |
|---|---|---|
| **Value** | 12.0 | $3.5273 \cdot 10^{-4}$ |

Table II.7: IEC spatial coherence parameters

Figure II.8 shows the coherence for the IEC Model with the parameters from Table II.7 in the longitudinal direction for three different lateral separation distances at 16 m/s with D = 178 m. It can be seen that coherence increases with smaller separation distance.

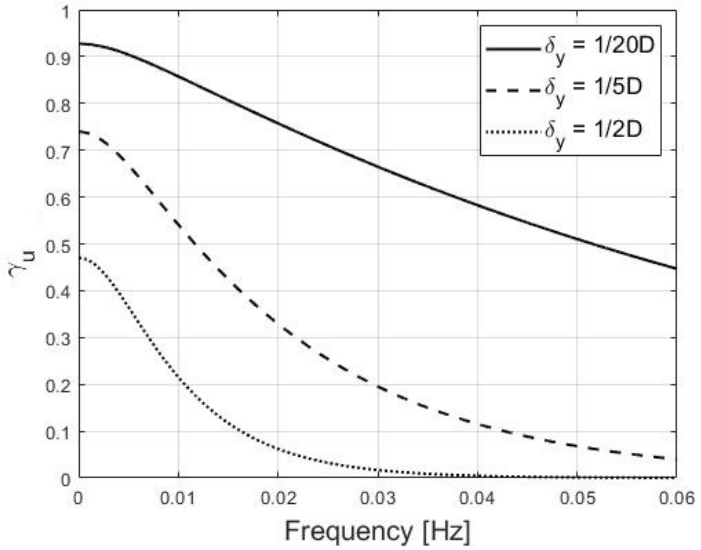


Figure II.8: *Coherence between two points (0,119) and ($\delta_y$, 119) at a fixed x-plane in the u-velocity direction for the IEC Model at 16m/s*

In this thesis, $a_K$ and $b_K$ will be fitted to measurements for u-, v- and w-components to allow for vertical and lateral coherence.

## Mann coherence

Spatial coherence is inherent to the Mann model and given by the integral of the spectral tensor $\phi_{i,j}$ as a function of the nondimensional separation distance and spatial wave number. The cross-spectrum is defined as:

$$\chi_{ij}(k_1, \Delta y, \Delta z) = \int_{-\infty}^{\infty}\int_{-\infty}^{\infty} \phi_{ij}(k) \exp i(k_2\Delta y + k_3\Delta z)dk_2dk_3 \tag{II.16}$$

where $\Delta y$ and $\Delta z$ are the separation distances of the two points in the lateral and vertical directions and $k_2$ and $k_3$ are the spatial wave numbers corresponding to the lateral and vertical directions. The

one-point spectrum is obtained by setting $\Delta y = \Delta z = 0$ and $i = j$: $\chi_{ij}(k_1, 0, 0) = F_i$. The vertical coherence is then defined as:

$$\gamma_{ij}(k_1, \overline{L}, \overline{\Gamma}, \Delta z) = \frac{\left|\chi_{ij}(k_1, \alpha\epsilon^{2/3}, \overline{L}, \overline{\Gamma}, \Delta z)\right|^2}{F_i(k_1, \alpha\epsilon^{2/3}, \overline{L}, \overline{\Gamma}) F_j(k_1, \alpha\epsilon^{2/3}, \overline{L}, \overline{\Gamma})} \tag{II.17}$$

$\overline{L}$ and $\overline{\Gamma}$ are the average of the $L$ and $\Gamma$ parameters values at the two points, $k_1 = 4\pi f/(u_1 + u_2)$. Chougule[47] explained that the coherence computed by the Mann model is independent of $\alpha\epsilon^{2/3}$. In order to compute the coherence, Cheynet's[27] Matlab function will be used in this thesis. With the three Mann parameters, Cheynet's function extracts a spectral tensor useful for the coherence computation.

### Davenport coherence

Davenport[51] proposed that the coherence spectrum of the longitudinal turbulence component for different vertical separations could be described by an exponential function with a decay parameter, $C$, as follows:

$$\gamma(\delta, f) = \exp\left(-C \cdot \frac{f\delta}{\overline{u}_{hub}}\right) \tag{II.18}$$

As can be seen from Equation II.18, the Davenport coherence model cannot model negative coherence. Secondly, even though this model was proposed for the longitudinal turbulence component, it will be used to compute the three wind components coherence, as Nybø et al.[26] did for the TIMESR turbulence generation (explained in the next sections). In the TurbSim implementation, the decay coefficient is dependent upon the velocity component, but independent of the separation direction. Nonetheless, the decay coefficients obtained via fitting will take into account the separation distance. More advanced coherence models may be considered, but as highlighted by Chougule,[47] the Davenport model seems to fit quite well to the u-coherence and v-coherence at FINO1.

## II.2.4 Atmospheric stability effect on the two turbulence models

The Kaimal and Mann models are both valid only for neutral conditions. Using these models for non-neutral atmospheric conditions may lead to inaccurate results. Nonetheless, both models have parameters that could be changed in order to approach a desired atmospheric condition.

### Mann parameters

Sathe et al.[12] and Peña et al.[25] performed a $\chi^2$ fit to get the three parameters values for different atmospheric stability. Cheynet et al.[52] developed an algorithm to estimate the parameters of the model in the least-square sense. Cheynet's algorithm will be used for this thesis as it is a simple Matlab function.

Going through the literature, there appear to be trends for each of the Mann's parameters but also differences depending on the measurement site.

**$\alpha\epsilon^{2/3}$ parameter**

Since this parameter shows the turbulence energy content, it should decrease with stability. The more stable the atmosphere, the lower the value of the parameter. Nonetheless, fitting of this parameter at Høvsøre from Peña et al.[25] and Chougule[47] show that $\alpha\epsilon^{2/3}$ value for neutral is higher than the values for unstable conditions and stable conditions, in contradiction with the hypothesis. Offshore, de

Maré and Mann[16] showed the same trend. Twidell and Gaudiosi[40] showed that under neutral stability conditions, turbulence was purely mechanically generated which explains the fact that $\alpha\epsilon^{2/3}$ for neutral conditions is the highest since it characterizes shear turbulence according to Chougule.[47]

**$L$ parameter**

Sathe et al.,[12] Peña et al.,[25] Chougule[47] and de Maré and Mann[16] all agree upon the fact that from stable to unstable conditions, $L$ increases. According to Chougule, this parameter is the measure of buoyant generated turbulence as it is increasing for unstable condition indicating that unstable conditions have the largest eddy size.

**$\Gamma$ parameter**

$\Gamma$ value should decrease with decreasing stability since it is a measure of the stretching of eddies due to wind shear. Sathe et al.[12] found that for all wind speeds, $\Gamma$ was largest for neutral stability condition followed by stable and unstable and Peña et al.[25] results follow the theory. However, de Maré & Mann,[16] offshore, and Chougule,[47] at Høvsøre, found the opposite behaviour, $\Gamma$ decreases as stability increases.

### Coherence

Chougule et al.[47] computed vertical coherence from the Høvsøre measurements using Mann Model and showed that u-, v- and w- vertical coherences are affected by atmospheric stability such that from stable to unstable, the coherence is increasing. The w-component is the most affected while the longitudinal u-component is the least affected by variation in atmospheric stability. This is in agreement with the theory that under different atmospheric stability, eddy length is the most influenced parameter which defines how much the eddies extend vertically.

## II.3 Floating wind turbine dynamics

Before presenting the floaters, an overview of the literature will be proposed in this section. Floating wind turbines are attached to the sea bed via mooring lines or taut lines. Since their natural frequencies are lower than the bottom-fixed wind turbines, FWTs are more likely to be influenced by the lower frequency range of the wind spectrum which contain the most energy. Different floater types have been developed: buoyancy stabilized, mooring line stabilized and ballast stabilized floaters (see Figure II.9).

The LIFES50+ project,[53] for instance, developed a semisubmersible concept and the Hywind Scotland[19] farm uses ballast stabilized floater (spar-type). All concepts have perks that will not be discussed in this work. According to Jonkman and Matha,[54] buoyancy stabilized concepts have the highest loads for all wind conditions. Differences between ballast and mooring line stabilized platforms are only significant in the tower loads, which are greater for the ballast stabilized platforms. From this study, no conclusion was drawn about the best floating wind turbine concept but rather study to what extent a platform choice could impact the turbine loads.

### II.3.1 Effects of turbulence model choice on FWT

The differences between the two turbulence models (Kaimal and Mann) for the response of bottom fixed and onshore turbines are very small but are relevant in the case of floating wind-turbines.[41,21]

Doubrawa et al[21] compared the Mann and the Kaimal models to large eddy simulations (LES) and measurements. It has been found that the Mann model matched the LES and the measurements better for low wind speed and that, for higher wind speeds, the Kaimal model matched the LES more while

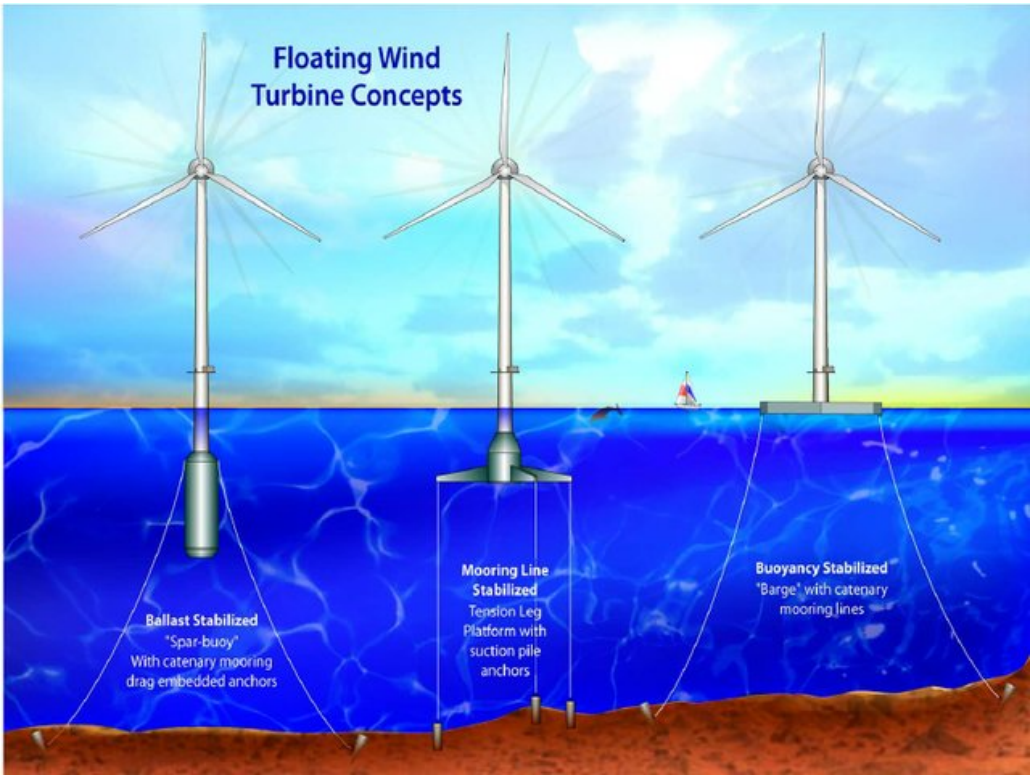


Figure II.9: *Three main floating wind turbine concepts*[13]

the Mann model showed results closer to the measurements. Furthermore, both models were found to overpredict fatigue loading in high-wind speed scenarios and to underpredict it in low-wind speed scenarios. These results are pertinent because the choice of the wind model affects the FWTs dynamics, as reported in the works of Eliassen and Bachynski[28] and Wise and Bachynski.[14]

Eliassen and Bachynski[28] studied the effect of the two models on three different FWT concepts using a 5 MW turbine. Kaimal was found to result in larger surge and pitch responses while Mann resulted in larger yaw, sway and roll motions. The difference in coherent structures between the two models explained these differences. Tower and mooring lines loads were also influenced by the model choice. Indeed, Mann resulted in larger damage equivalent loads in the tower top while Kaimal was found to result in more damages in the mooring line for the semisubmersible and spar platforms. Myrtvedt and Nielsen[29] found the same results with a DTU 10 MW turbine on spar-type floater.

As of now, no conclusion has been drawn on the best turbulent model but extensive measurements data would be required.

### II.3.2 Effects of atmospheric stability on wind turbines

While this thesis will study the effects of atmospheric stability on FWT using fitted parameters, previous work has been done on fixed wind turbine and spar-type floaters. Concerning the influence of atmospheric stability on wind turbine loads, Sathe et al.[12] carried out simulations on a fixed wind turbine and based on offshore measurements. A fitting of the Mann model to the turbulence measurements has been performed to obtain the three model parameters required for different atmospheric stabilities. It was observed that under stable conditions, the tower loads are influenced mainly by turbulence, blade loads by a combination of wind profile and turbulence, and rotor loads mainly by wind profile. The calculated tower loads are up to 17% smaller using stable wind conditions in comparison with those obtained under neutral conditions. The corresponding blade loads are up to 3% smaller, whereas the rotor loads are up to 12% larger than those obtained assuming only neutral conditions.

These results also show that modelling of site wind conditions need to take into account atmospheric stability, turbulence intensity and shear to be as close as possible to reality. However this study has been carried out with a fixed wind turbine.

Doubrawa et al.[21] only fitted turbulence intensity to atmospheric stability for the two standard wind models but mainly used SOWFA simulations to study the effect of atmospheric stratification on a spar-type FWT. It was found that loads on the mooring system are most sensitive to atmospheric stability in low winds and that loads on the blade root are most sensitive to atmospheric stability in high winds.

Jacobsen and Godvik[22] studied the influence of atmospheric stability on the Hywind Scotland floater. With stable atmospheric conditions, a decrease in FWT motions has been observed compared with unstable and neutral conditions. Jacobsen and Godvik supposed that the decrease was due to both the reduction in turbulence intensity and the reduction of the sizes of the turbulent eddies.

Putri et al.[55] modelled a spar floater with unstable conditions and found that the DEL of tower top torsion is estimated to be higher than in neutral conditions, similarly for the tower base side-side bending DEL. It was also found that the use of an appropriate wind model (Kaimal or Højstrup in this work) for unstable conditions can produce up to 40% higher turbulence intensity (TI) compared to neutral conditions. This works show the importance of accounting for atmospheric stability for FWT and to develop a suitable turbulent wind model in the offshore boundary layer.

# CHAPTER III

# Floater

This chapter contains a description of the floater used in this thesis. It will first present the spar-type floater, then go through a natural frequencies study.

The wind turbine used will be the DTU 10 MW reference turbine[56] whose main characteristics can be found in Table III.1. First designed for onshore, the DTU 10 MW turbine has been modified for offshore models. For instance, the tower design has been changed to avoid resonance at the 3P frequency because of the increase in the tower bending frequency for FWTs. The wind turbine will be installed on top of the considered floater: a spar type floater. The hub height for the FWT is 119 meters above the still water line (SWL). Visualizations of the FWT can be seen in Figure III.1 and more details on the floater can be found in Subsection III.1.

| **Parameter** | **Value** |
|---|---|
| Rated power [MW] | 10 |
| Rotor orientation and configuration | Upwind, three blades |
| Rotor, hub diameter [m] | 178.3 and 5.6 |
| Cut-in, rated and cut-out wind speed [m/s] | 4.0, 11.4 and 25.0 |
| Cut-in, rated rotor speed [rpm] | 6.0 and 9.6 |
| Rotor, nacelle mass | 230.7 and 446.0 tonnes |

Table III.1: *Main characteristics of the DTU 10 MW reference turbine*[56]

The blade pitch controllers have been modified to avoid negative feedback at the platform pitch natural frequency.[57] Furthermore, to limit low-frequency dynamic responses, the floater use a constant generator torque strategy in above-rated conditions. The wind turbine controller characteristics are listed in Table III.2.

Tables III.3 and III.4 present some of the floater characteristics and their mooring system properties, respectively. Tables have been extracted from Wenfei's work.[1]

Figure III.2 shows the mooring layout of the floater. The mooring line 2 will be studied for the fatigue analysis as it is the one facing the wind.

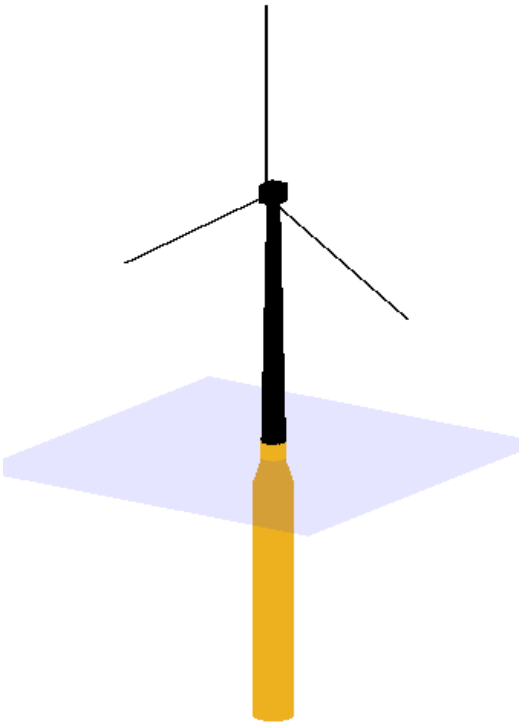

Figure III.1: *Computational model of the spar with lines representing the blades visualized in MATLAB. The tower and rotor are colored in black while the hydrodynamic members are colored in yellow*

| **Parameter** | **Onshore** | **Spar** |
|---|---|---|
| Blade pitch controller natural frequency [Hz] | 0.06 | 0.02 |
| Blade pitch $K_I$ [rad/(rad/s)] | 0.141233 | 0.015693 |
| Blade pitch $K_P$ [rad/(rad/s)] | 0.524485 | 0.174828 |
| Above-rated strategy | Constant power | Constant torque |

Table III.2: *Wind turbine controller characteristics*[57]

| **Parameter** | **Spar** |
|---|---|
| Water depth [m] | 320 |
| Draft [m] | 120.0 |
| Displacement [tonnes] | 13 350 |
| Platform pitch inertia about SWL [$kgm^2$] | $6.53 \cdot 10^9$ |
| Platform yaw inertia about SWL [$kgm^2$] | $2.49 \cdot 10^9$ |

Table III.3: *Floating wind turbine characteristics*[1,53]

| Parameter | Spar |
|---|---|
| Number of lines [-] | 3 |
| Radius to anchors [m] | 849.5 |
| Unstretched mooring line length [m] | 902.20 |
| Equivalent mooring line mass density [kg/m] | 233.1 |
| Equivalent mooring line axial stiffness [N] | $384.243 \cdot 10^6$ |
| Fairlead depth below SWL [m] | 70 |
| Additional yaw spring stiffness [Nm/rad] | $1.47 \cdot 10^8$ |
| Pretension [kN] | 2600 |

Table III.4: *Floating wind turbine mooring system properties*[1,53]

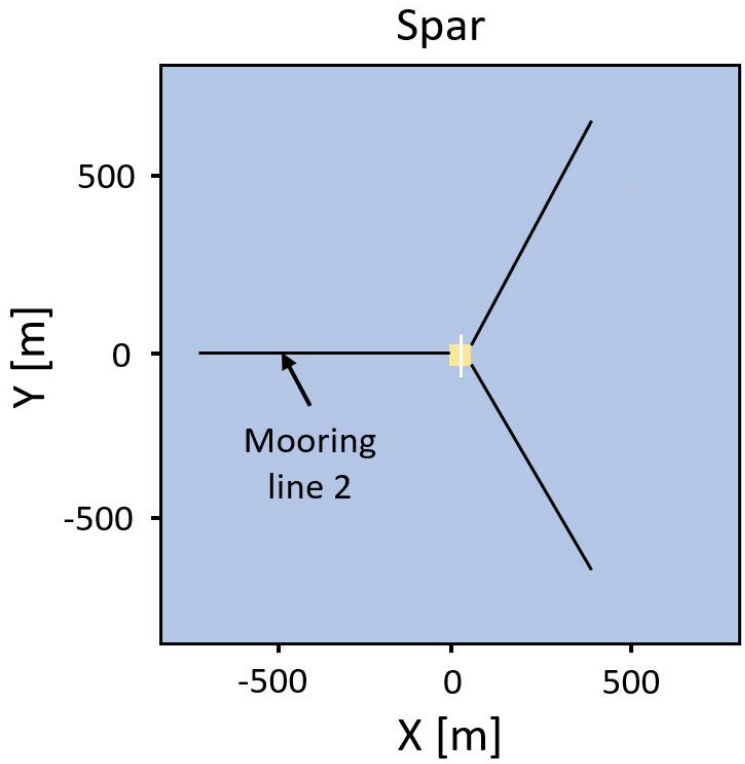


Figure III.2: *Mooring system layout for the floater*[14]

# III.1 Spar

The spar[1] was developed by the Norwegian University of Science and Technology (NTNU) in SINTEF Ocean's SIMA software and converted to the FAST framework. As seen in Figure III.3 it is ballast stabilized, leading to a small natural frequency in surge and a high natural frequency in yaw compared to the other natural frequencies due to its small inertia (see Table III.5 in Section III.2).

The NTNU 10 MW spar platform is based on the 5 MW OC3-Hywind:[58] it has the same draft of 120 m and is similarly designed for a water depth of 320 m, but the diameter of the column has been increased to provide additional buoyancy for the heavier 10-MW turbine and to match the tower base diameter. Furthermore, its displacement is of $13,350$ tonnes. Three catenary mooring lines are used in the mooring system. To simplify the modelling, the delta connection usually used to connect the fairleads with the hull is not modelled. This delta connection provides additional yaw stiffness. To provide a sufficient yaw restoring force, an additional yaw spring stiffness of $1.48 \cdot 10^8 Nm/rad$ is added to the model. This concept connects to the tower at 10 m above the SWL requiring the tower

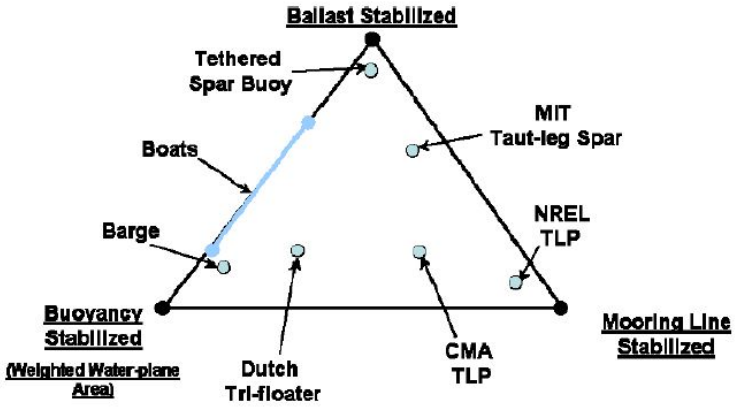


Figure III.3: *Floating support structure stability triangle*[15]

to be shortened to achieve a hub height of 119 m. The tower needs to be redesign as the tower natural frequency lies within the 3P range.

# III.2 Natural frequencies study

To determine the natural frequencies of the floater, free decay tests have been performed with OpenFAST.[4] In ElastoDyn, only the degree of freedom that was of interest was activated, aerodynamics and hydrodynamics loads were deactivated. An arbitrary initial position was set for each decay test (1 meter or 1 degree depending on the degree of freedom) and the simulation started. The duration of the simulation was chosen to be 3600 seconds in order to let the structure motions decay. A smaller duration could have been chosen but since the simulation were computationally inexpensive, this value was picked by default. The wind turbine structure will then oscillate around its initial position and the motions will be damped within a natural period. As an example, Figure III.4 shows the decay test for the spar surge motion. Other decay plots can be found in Appendix A. The turning points are shown as black dots and are used to compute the natural period. Results of decay tests for other degrees of freedom can be found in Table III.5.

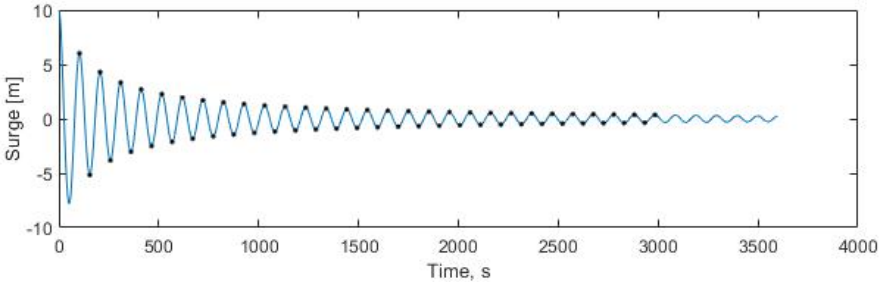


Figure III.4: *Decay test for the spar floater surge motion*

| Degree of freedom | Natural period [s] | Natural frequency [Hz] |
|---|---|---|
| Surge | 102.4 | 0.010 |
| Heave | 31.3 | 0.032 |
| Pitch | 35.1 | 0.029 |
| Yaw | 8.1 | 0.1235 |
| Tower | 2.5 | 0.399 |

Table III.5: NTNU spar natural periods and frequencies in OpenFAST

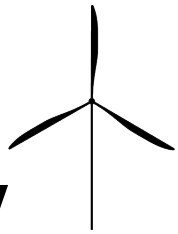

# CHAPTER IV

# Environmental conditions

Determining the right environmental conditions for the simulations is crucial when the main topic of the work is the atmosphere. Wind measurements from the FINO-1 platform[3] and wave measurements from Norway-5[59] were used to obtain relevant environmental conditions for the simulations. In this thesis, three wind speeds were selected to cover the different wind turbine regimes: below-rated, rated and above rated. 7.5, 12 and 16 m/s were chosen to investigate the FWT dynamics in its different regimes of operation. Below rated wind speed, the turbine is designed for maximum aerodynamic efficiency while the mean thrust has its maximum at rated wind speed. The below rated case is chosen at a typical wind speed at FINO-1, close to 7.5 m/s.[21] 12 m/s is chosen in order to avoid being at the interface between two regions where the controller would jump between modes due to turbulence. Above rated wind speed, the wind speed with the same mean thrust as for the below rated scenario has been chosen, 16 m/s.

## IV.1 Wave

Wave conditions could not be derived from FINO-1 measurements because of the shallow water depth at this site. Li et al.[59] presented long-term joint distribution of wind speed ($U_w$), significant wave height ($H_s$) and peak period ($T_p$) at five different sites in Northern Europe. The site Norway 5 has been chosen as it corresponds to deep-water conditions. With a depth of 202 meters, Norway 5 was more representative for the floater. 10-year wind and wave statistics are generated using hindcast data of 1-hour averaged wind and sea states. For this specific site, Li et al.[59] proposed parameters for the joint distribution:

$$f_{U_w,H_s,T_p}(u,h,t) = f_{U_w}(u) \cdot f_{H_s|U_w}(h|u) \cdot f_{T_p|H_s}(t|h) \tag{IV.1}$$

where the conditional distribution,

$$
\begin{aligned}
f_{U_w}(u) &= \frac{\alpha_U}{\beta_U}\left(\frac{u}{\beta_U}\right)^{\alpha_U-1}\exp\left[-\left(\frac{u}{\beta_U}\right)^{\alpha_U}\right], \\
f_{H_s|U_w}(h|u) &= \frac{\alpha_{HC}}{\beta_{HC}}\left(\frac{h}{\beta_{HC}}\right)^{\alpha_{HC}-1}\exp\left[-\left(\frac{h}{\beta_{HC}}\right)^{\alpha_{HC}}\right], \\
f_{T_p|H_s}(t|h) &= \frac{1}{\sqrt{2\pi}\sigma_{LTC}t}\exp\left(-\frac{1}{2}\left(\frac{\ln(t)-\mu_{LTC}}{\sigma_{LTC}}\right)^2\right)
\end{aligned}
\tag{IV.2}
$$

with $\mu_{LTC}$ and $\sigma_{LTC}$ the mean value and standard deviation of $\ln(t)$ at each combination of wave-wind class.

Table IV.1 presents the wave conditions used. Since the focus of the work is on the influence of atmospheric conditions, the sea conditions do not vary with atmospheric stability in our study.

| **Hub height wind speed [m/s]** | $H_s$ **[m]** | $T_p$ **[s]** |
|---|---|---|
| 7.5 | 1.8 | 9.6 |
| 12 | 2.4 | 10.1 |
| 16 | 3.2 | 10.6 |

Table IV.1: Wave conditions

# IV.2 Wind

## IV.2.1 FINO-1 platform available data

The FINO-1 platform[3] is located in the immediate vicinity of areas where wind farms are being built or are already in operation, 45 km off the coast of Germany (see Figure IV.1). The platform is equipped with meteorological sensors for wind, temperature and humidity at levels between 30 and 102 m and marine sensors. FINO-1 is part of the RAVE database,[60] an initiative carrying research work in Alpha Ventus, the first German offshore test field, since 2009.

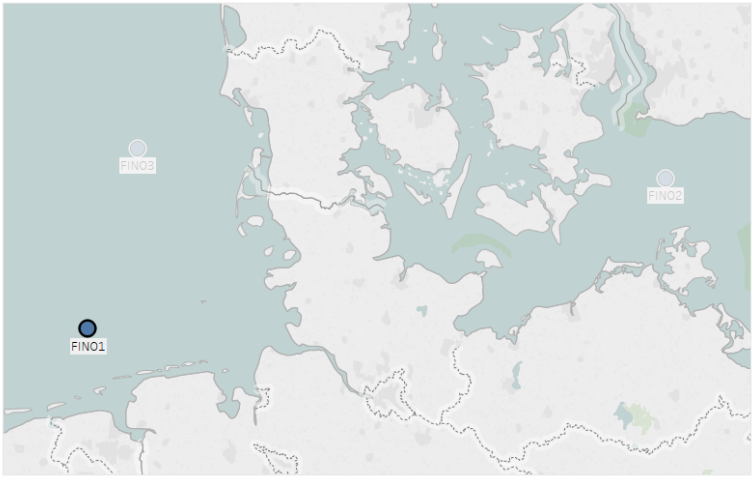


Figure IV.1: *Map of FINO-1*[3]

High frequency wind measurement (20 Hz) by ultrasonic anemometers are performed at 40, 60 and 80 m and cup anemometers measurements (10-minutes averaged) are available from 34 to 102 meters, every ten meters approximately. The sonic raw data are stored in 10-minutes duration blocks, as commonly used in wind research and engineering. This thesis uses wind direction, wind speed in three directions from January 1st, 2016 to December 31st, 2017. This period was chosen due to the common availability of high-frequency measurements (sonic anemometers) and 10-minutes averaged measurements (cup anemometers).

Data measurements were used to fit turbulence intensities and power law wind profile for each hub height wind speed of interest (7.5, 12 and 16 m/s) and for each stability conditions (stable, neutral and unstable). It was also used to fit the Mann model parameters and the Kaimal model to the required stability conditions. Finally, measurements provided data for TIMESR simulations with TurbSim (explained below).

## IV.2.2 Data processing

Data was extracted from different sources presented in Table IV.2:

| Device | Type of measurements |
|---|---|
| Sonic anemometer (40, 60, 80 meters) [Wind speed and direction] | 20-Hz |
| Cup anemometers (34, 41, 51, 61, 71, 81, 91, 102 meters) [Wind speed] | 10-min averaged |
| Wind direction (62 meters) [Wind direction] | 10-min averaged |

Table IV.2: Device used and measurements extracted

Ten minutes averaged measurements were extracted for computational reasons. Indeed, data processing following Nybø's[61] method with high-frequency measurement was too expensive. Using only a personal laptop, Matlab would run out of memory while processing the data. In this thesis, the 10-min averaged measurements were processed following Nybø's[61] method (presented below) and the high-frequency measurements were extracted from the time-period given by the processed 10-min averaged measurements.

### Processing method

- Removal of missing measurements (NaN and -999 values),
- Spike detection and removal,
- Removal of data due to rain,
- Exclusion geographical zone (45 to 225 degrees) due to mast shadow, wind parks proximity and nearby land,
- Organizing in 1-hour periods,
- Delete non-stationary periods.

Each of the 10-min averaged measurements were processed following this method. The geographical exclusion zone is defined to avoid the mast shadow when the wind blows from South and East. Concerning the stationarity assessment, Cheynet et al.'s method was used:[62] the first step checks that the wind speed time serie slope over an hour is lower than 20% (Equation IV.3), the second step requires the maximum moving mean and maximum moving standard deviation to be less than a threshold value, here 40% (Equation IV.4).

$$\frac{|\Delta U_{\Delta t}|}{\overline{U_{\Delta t}}} \leq 0.2 \tag{IV.3}$$

$$max\left(\frac{|\overline{U_{60Min}} - \overline{U_{10Min}}|}{\overline{U_{60Min}}}\right) \leq 0.4 \text{ and } max\left(\frac{|\overline{\sigma_{10Min}} - \sigma_{10Min}|}{\overline{\sigma_{10Min}}}\right) \leq 0.4 \tag{IV.4}$$

where $|\Delta U_{\Delta t}|$ is the absolute difference between the wind speed values at the end and beginning of the period considered.

Details for the method can be found in Nybø's work.[61] The "rotation" step of Nybø's method was performed only after extraction of the high-frequency data for the computation of the turbulence intensity, the Mann parameters fitting and the coherence fitting. The rotation step is the process of rotating the wind speed time series in the mean flow direction. It is done with the double rotation method.[63] This method depends on both a fixed tilt angle of the anemometer and the wind direction, leaving a zero mean vertical wind speed in all 1-hour periods.

## Usage of data

After the data processing, all 1-hour periods were sorted following the gradient Richardson number classification[35] then were used to generate a wind profile following the power law. This process allowed us to identify the atmospheric conditions for all 1-hour periods. The corresponding wind speed high-frequency time series were then extracted and used to compute the turbulence intensity, to fit the Mann model and to fit the coherence models. A map of the data usage is presented in Figure IV.2.

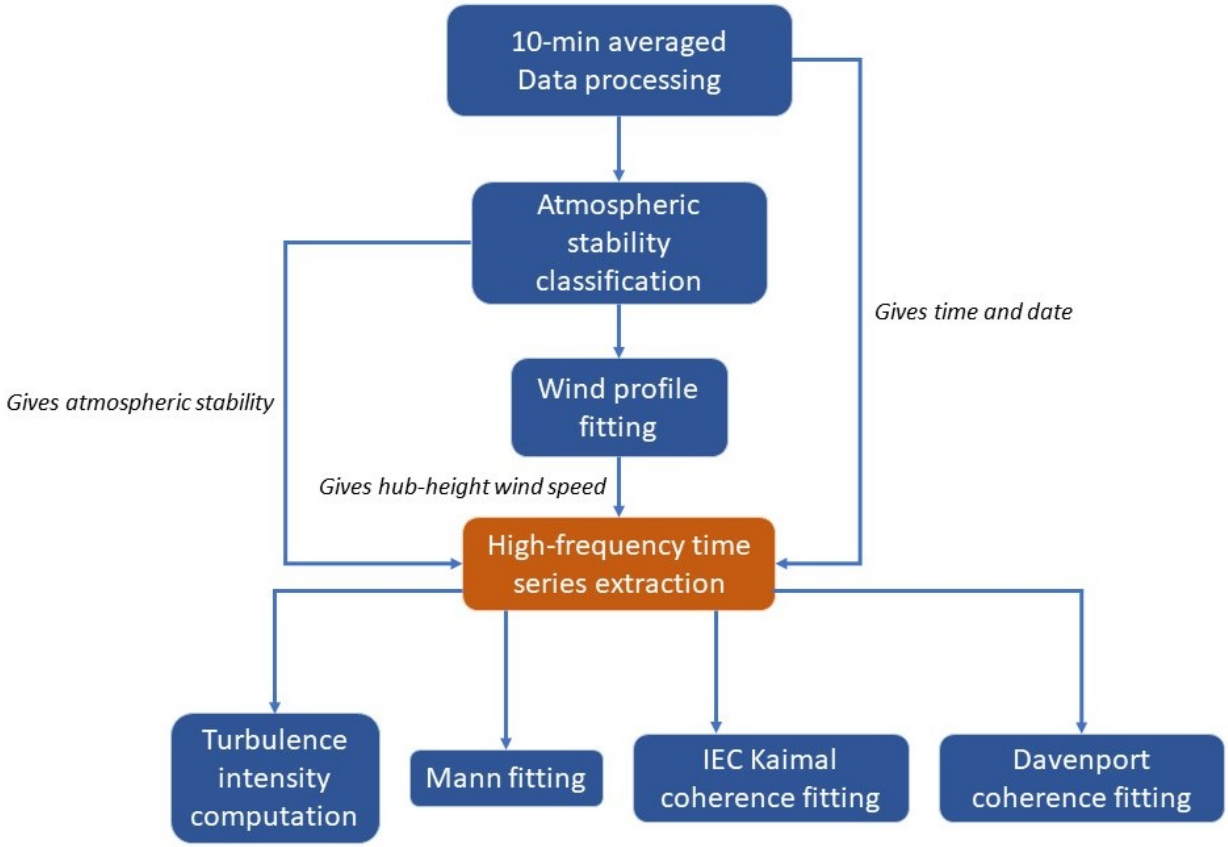


Figure IV.2: *Map of data usage*

## IV.2.3 Atmosphere stability classification

Eliassen and Obhrai[28] chose the gradient Richardson number to measure atmospheric stability at FINO-1 and FINO-3.[35] In this thesis, temperature at 72 and 42 meters and wind speed at 91 and 71 meters were used. It is to be noted that only 10-min averaged measurements are used here for the classification.

Figure IV.3 shows the resulting atmospheric stability distribution. It can be seen that the distribution followed that found by Nybø[41] and Obhrai[42] (see Figure II.6). With increasing wind speed, neutral conditions were more frequent and, consistently with Cheynet et al.,[64] unstable conditions were common at low wind speeds at FINO-1.

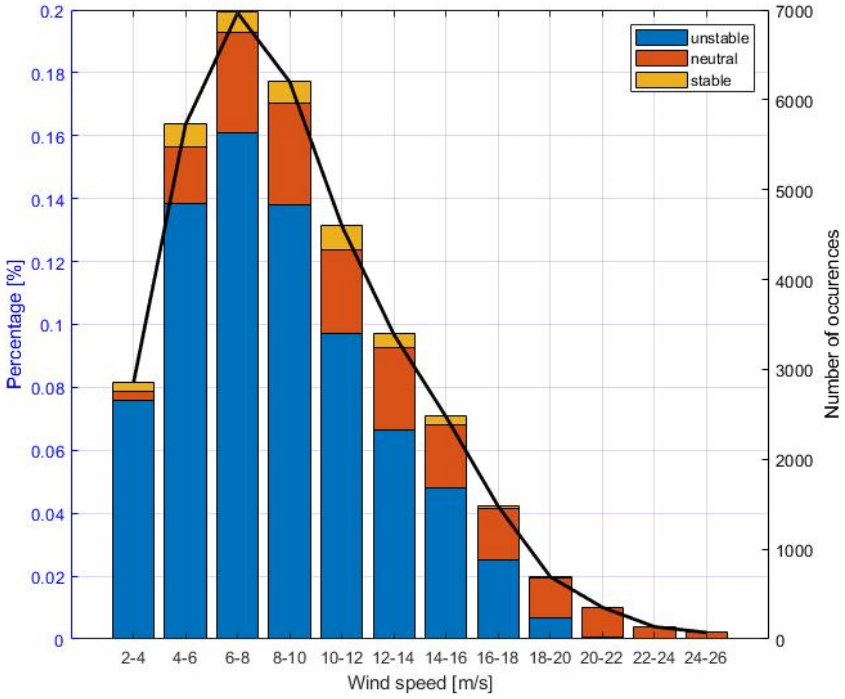


Figure IV.3: *Atmosphere stability distribution*

Following the atmospheric stability classification, all 1-hour period were sorted based on their stability conditions.

## IV.2.4 Power law fitting

The wind speed at 119 meters was found by fitting the power law to the measurements. For each of the stability conditions, a fitting using anemometers cups at 34, 41, 51, 61 and 71 was performed. From the fitting, Figure IV.4 was obtained where each power law exponent was computed from the average of 15 cases per situation. 15 cases were used to limit the uncertainties on the value. Figure IV.4 shows clearly the expected stability dependency of the wind profiles, with an increase in vertical wind shear from unstable to stable atmospheric conditions. Additionally, Figure IV.5 shows the statistical variations of the 15 cases. Measurements at 81, 91 and 102 meters were not used because, according to Emeis and Türk,[65] offshore wind profiles above 80 meters are already above the surface layer for the stability conditions considered, within which the power law is valid. Figure IV.4 still shows the cup anemometers measurements for these three heights. It can be seen that, above 81 m, the measured wind speeds under neutral conditions decreased with height at 7.5 and 12 m/s mean hub height wind

speed. Generally, measurements at 81, 91 and 102 meters for stable and unstable conditions followed the fit.

The power law coefficient variation shows a few negative coefficient in the neutral case and the variation was the smallest for unstable and stable conditions at 12 and 16 m/s mean wind speeds.

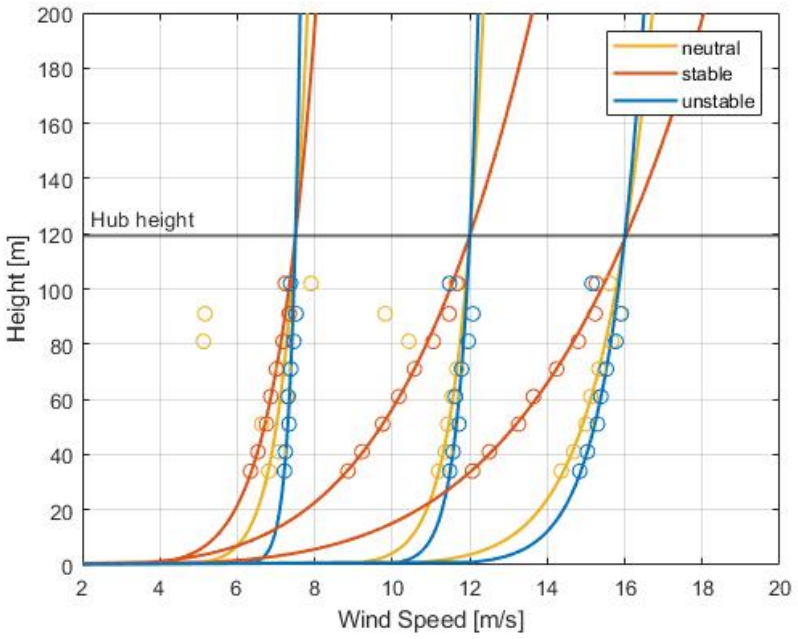


Figure IV.4: *Wind profile for each wind speed of interest at hub height and atmospheric stability. The circles represent the cup anemometers measurements*

| **Stability condition** | Stable | | | Neutral | | | Unstable | | |
|---|---|---|---|---|---|---|---|---|---|
| **Wind Speed [m/s]** | 7.5 | 12 | 16 | 7.5 | 12 | 16 | 7.5 | 12 | 16 |
| **Power law exponent** [-] | 0.13058 | 0.119383 | 0.228589 | 0.078433 | 0.054724 | 0.083265 | 0.03104 | 0.03443 | 0.058519 |

Table IV.3: Power law exponent values

## IV.2.5 High-frequency extraction

From the previous steps, all 1-hour periods were sorted in atmospheric stability and hub height mean wind speed. The data used for the rest of the modelling was the 20-Hz ultra sonic anemometers measurements at 40, 60 and 80 meters. To limit uncertainties, 15 different timeseries (hereafter called "cases") were used for each situation (each wind speed and stability conditions). Figure IV.6 summarizes it.

After the extraction, all time series were rotated following the double rotation method at all heights but the 40 and 60 meters data were rotated back to the mean flow direction at 80 meters as done by Nybø.[61]

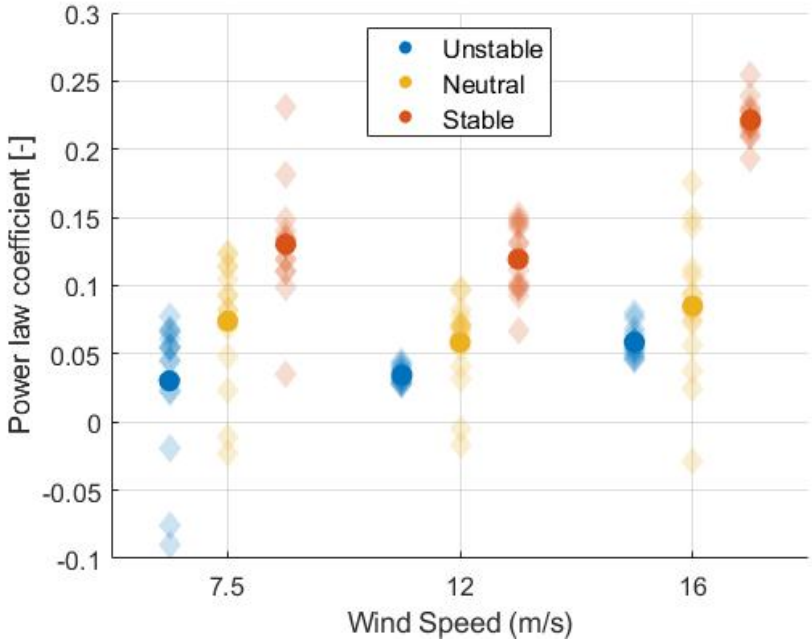


Figure IV.5: *Power law coefficient statistical variation as a function of wind speed. The dark shapes denote the average of the cases while the transparent diamonds denote the different cases*


Figure IV.6: *High-frequency measurements extraction*

## IV.2.6 Standard deviation computation

The computation of the turbulence was done at 80 meters by taking the average of 15 cases of each of the 9 situations, where the standard deviation was assumed constant with height, as done by Nybø.[26] Equation IV.5 was simply used for the computation of the turbulence intensity:

$$TI = \frac{\sigma_u}{\overline{u}_{hub}} \tag{IV.5}$$

Table IV.4 and Figure IV.7 present the standard deviations at 80 meters and the turbulence intensity at hub height as a function of wind speed and stability conditions, respectively. Consistently with theory, turbulence intensity increased with decreasing stability. Nonetheless, turbulence intensity decreased with wind speed which is not what was found by Tuerk et al.[9] at FINO-1 for the period September 2003 - August 2007. Statistical variation via standard deviation of the measured standard deviations can be found in Table IV.5 as well. It was found that the statistical variation of the standard deviations in the three directions was relatively small.

| **Stability conditions** | Stable | | | Neutral | | | Unstable | | |
|---|---|---|---|---|---|---|---|---|---|
| **Wind Speed [m/s]** | 7.5 | 12 | 16 | 7.5 | 12 | 16 | 7.5 | 12 | 16 |
| $\sigma_u$ **[m/s]** | 0.529 | 0.755 | 0.774 | 0.583 | 0.922 | 1.056 | 0.713 | 1.036 | 1.358 |
| $\sigma_v$ **[m/s]** | 0.491 | 0.539 | 0.787 | 0.563 | 0.777 | 1.056 | 0.677 | 0.789 | 1.220 |
| $\sigma_w$ **[m/s]** | 0.235 | 0.262 | 0.383 | 0.343 | 0.539 | 0.566 | 0.321 | 0.516 | 0.617 |

Table IV.4: Standard deviations as a function of wind speed and stability conditions

| **Stability conditions** | Stable | | | Neutral | | | Unstable | | |
|---|---|---|---|---|---|---|---|---|---|
| **Wind Speed [m/s]** | 7.5 | 12 | 16 | 7.5 | 12 | 16 | 7.5 | 12 | 16 |
| $\sigma_{\sigma_u}$ **[m/s]** | 0.0654 | 0.0345 | 0.0549 | 0.0138 | 0.0934 | 0.0422 | 0.0750 | 0.1112 | 0.0581 |
| $\sigma_{\sigma_v}$ **[m/s]** | 0.0013 | 0.0239 | 0.0453 | 0.0201 | 0.0911 | 0.0629 | 0.0235 | 0.0592 | 0.0182 |
| $\sigma_{\sigma_w}$ **[m/s]** | 0.0690 | 0.0565 | 0.0360 | 0.0192 | 0.0221 | 0.0356 | 0.0651 | 0.0728 | 0.0239 |

Table IV.5: Standard deviation statistical variation

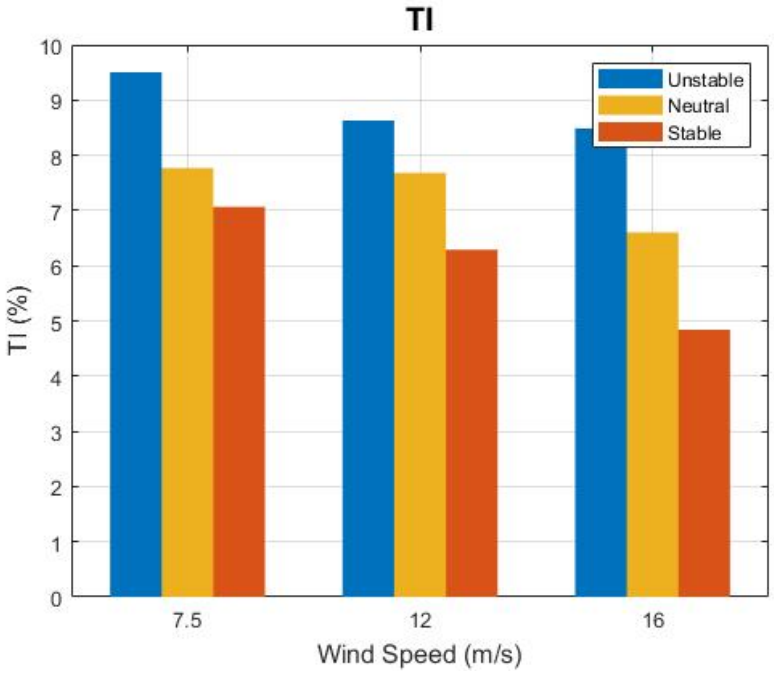


Figure IV.7: *Turbulence intensity as a function of wind speed and stability conditions*

Turbulence intensity from the IEC guidelines[2] was also computed. From Figure IV.7, we see that the highest turbulence followed the specification for a Class C site in the IEC standard.[2] The standard deviation in the longitudinal direction is defined following Equation II.7 as it was used in literature.[14] Table IV.6 summarizes the turbulence intensity at 119 meter height for the three wind speeds.

| **Stability condition** | IEC | | |
|---|---|---|---|
| **Wind Speed [m/s]** | 7.5 | 12 | 16 |
| **Turbulence intensity [%]** | 17.96 | 14.6 | 13.2 |

Table IV.6: IEC standards[2] turbulence intensity

## IV.2.7 Mann parameters

Cheynet et al.'s[52] algorithm was used to estimate the Mann parameters corresponding to the required stability. For the fitting, the average parameters of 15 cases of each of the 9 situations was taken. Cheynet's algorithm uses the 3-component spectra, the co-spectrum in the longitudinal and vertical direction and the wave number vector in the longitudinal direction. High-frequency time series at 80 meters height were considered since they are the closest to the hub height.

Spectra of the time series at 80 m were estimated using Welch's algorithm[66] with a Hamming window, six segments, and 50% overlapping, following Nybø's work.[41] Then, the spectra were bin averaged before the fitting was performed.

Scaling of the resulting parameters with height was considered, but the literature[67] shows use of this height for Mann parameters fitting while using the DTU 10-MW reference turbine. It is interesting to note the change in the parameters with height, offshore, in de Maré et al.'s[16] (see Figure IV.10) and Chougule's[47] work. We see that measurement height is an important factor for the length scale parameter in unstable conditions.

The resulting parameters are presented in Table IV.7 and visualized in Figure IV.8. The statistical variation of the three parameters is shown in Figure IV.9. The parameters recommended by the IEC[2] are also computed based on Table II.6 and are presented in Table IV.8.

| **Stability condition** | Stable | | | Neutral | | | Unstable | | |
|---|---|---|---|---|---|---|---|---|---|
| **Wind Speed [m/s]** | 7.5 | 12 | 16 | 7.5 | 12 | 16 | 7.5 | 12 | 16 |
| $\alpha\epsilon^{2/3}$ | 0.0165 | 0.0221 | 0.0384 | 0.0154 | 0.0327 | 0.0288 | 0.0192 | 0.0213 | 0.0236 |
| $L$ | 28.966 | 25.346 | 16.274 | 38.890 | 42.280 | 55.934 | 50.868 | 81.972 | 77.000 |
| $\Gamma$ | 3.644 | 2.847 | 2.356 | 3.144 | 2.623 | 3.332 | 3.185 | 3.768 | 4.331 |

Table IV.7: *Mann parameters*

| **Stability condition** | IEC | | |
|---|---|---|---|
| **Wind Speed [m/s]** | 7.5 | 12 | 16 |
| $\alpha\epsilon^{2/3}$ | 0.0766 | 0.1295 | 0.1882 |
| **L** | 33.6 | | |
| **Gamma** | 3.9 | | |

Table IV.8: *Mann parameters following IEC guidelines[2]*

We found that $L$ followed the expected increase with decreasing stability. Concerning the $\alpha\epsilon^{2/3}$ parameter, trends differed with wind speed: at 7.5 m/s, the value for unstable conditions was the highest and the smallest value occurred with neutral conditions while the opposite was true for 12 m/s. At 16 m/s the diffusion parameter increased with stability, in contradiction with the theory. $\Gamma$ followed de Maré & Mann[16] and Chougule[47] trends for 16 m/s: the parameter value increased with unstability.

These parameters were obtained with the average of 15 cases for each of the situations. While not following theoretical trends from the literature, they were kept for the rest of the thesis. The statistical variation can be quite large depending on the stability, the wind speed and the parameter considered. Stable conditions at 16 m/s gives the greatest standard deviation for the $\alpha\epsilon^{2/3}$ (0.013). The $L$ parameter greatest standard deviation (15.41) happens for neutral conditions at 16 m/s and stable conditions at 12 m/s gives the greatest standard deviation (0.87) for the $\Gamma$ parameters.

A sensitivity analysis of all parameters was also performed to assess how much each parameter influences the wind fields and the dynamics of a floating wind turbine (presented in Chapter VI).

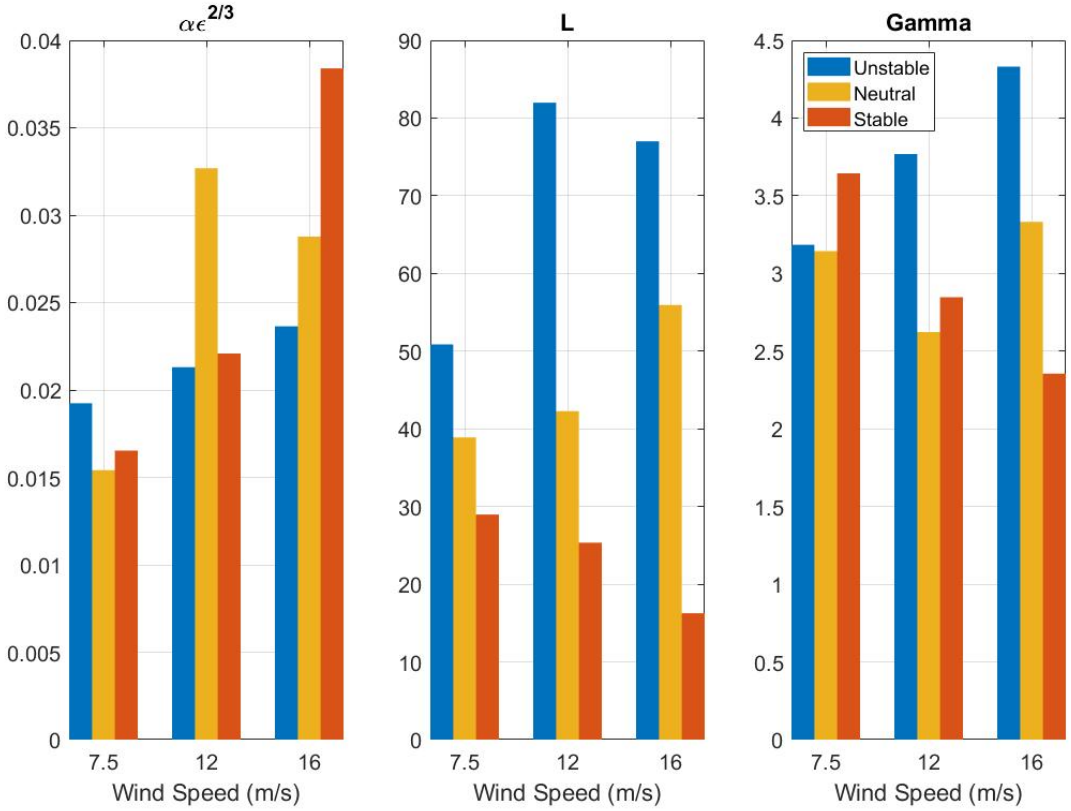


Figure IV.8: *Mann parameters as a function of wind speed and atmospheric stability*

## IV.2.8 Coherence fitting

Having three different heights for measurements allows the computation of coherence for different vertical separation distances (20 meters and 40 meters). According to Cheynet et al.,[64] the scale of turbulent structures may become too small compared to the separation between the sonic anemometers, above a stability limit, to allow an accurate study of the vertical coherence. They suggest then to study the coherence using separation smaller than 20 meters. Since the smallest separation available is 20 meters, only the couple (40-60) meters and (60-80) meters were available. To compute more accurately the turbulence at hub height, at least the sonic anemometer at 80 meters height should be used. High-frequency measurements at 80 and 60 meters were then used for the coherence fitting of all components. In this subsection, the statistical variation of the parameters will be presented as a standard deviation in tables.

### IEC Kaimal coherence

Equation II.15 was fitted to the measurements using Matlab. Similar to the Mann fitting, the resulting coherence parameters are the average of 15 cases. Table IV.9 presents the coherence parameters for the IEC Kaimal coherence model, Table IV.10 shows the statistical variation, and Figure IV.11 shows the corresponding coherence as a function of reduced frequency, $f_r = \frac{f\delta}{\bar{u}_{hub}}$, where $\delta = 20$ meters.

As seen from Figure IV.11, u-, v- and w-coherence increased with decreasing stability. This is in agreement with Chougule et al.'s[47] findings. The neutral and unstable vv-coherence at all wind speeds are very similar. It could be explained by the stability classification that is very broad for unstable and stable conditions while narrower for neutral conditions. Concerning the statistical variation of the parameters, the small variation allowed us to trust the chosen values.

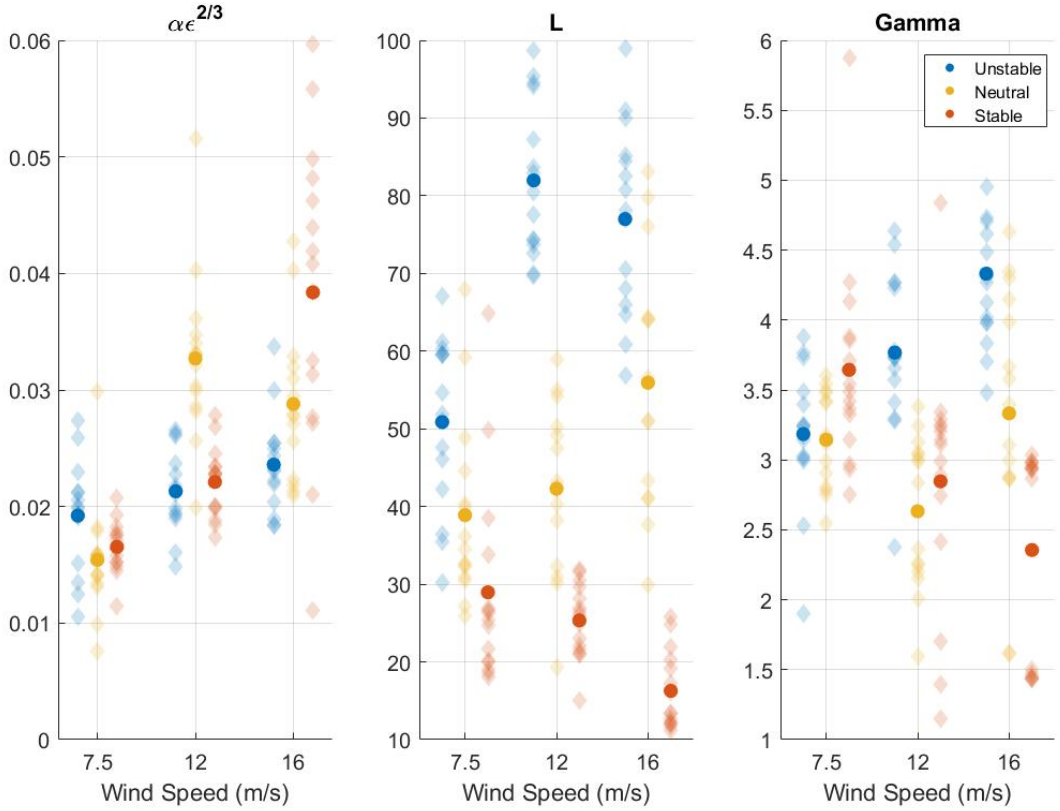


Figure IV.9: *Statistical variation of the Mann parameters. The transparent diamonds denote the different cases*

| **Stability condition** | Stable | | | Neutral | | | Unstable | | |
|---|---|---|---|---|---|---|---|---|---|
| **Wind Speed [m/s]** | 7.5 | 12 | 16 | 7.5 | 12 | 16 | 7.5 | 12 | 16 |
| $a_u$ | 8.081 | 8.632 | 12.670 | 3.175 | 5.387 | 10.089 | 2.558 | 4.511 | 6.963 |
| $b_u$ | 0.001 | 0.0002 | 0.0002 | 0.0005 | 0.0002 | -4.41e-05 | 9.58e-05 | 6.31e-05 | -2.31e-05 |
| $a_v$ | 5.239 | 4.479 | 8.281 | 1.882 | 2.699 | 3.619 | 1.681 | 2.963 | 4.373 |
| $b_v$ | 0.0036 | 0.0027 | 0.0043 | 0.0005 | 0.0032 | 1.49e-03 | 1.05e-03 | 7.12e-05 | -2.61e-04 |
| $a_w$ | 2.052 | 2.829 | 3.541 | 1.683 | 2.270 | 3.307 | 1.182 | 2.056 | 2.850 |
| $b_w$ | 0.0150 | 0.0034 | 0.0089 | 0.0027 | 0.0055 | -6.45e-04 | 1.14e-03 | 9.96e-04 | 1.02e-03 |

Table IV.9: IEC Coherence model parameters

| **Stability condition** | Stable | | | Neutral | | | Unstable | | |
|---|---|---|---|---|---|---|---|---|---|
| **Wind Speed [m/s]** | 7.5 | 12 | 16 | 7.5 | 12 | 16 | 7.5 | 12 | 16 |
| $\sigma_{a_u}$ | 0.016 | 0.531 | 0.189 | 0.056 | 0.039 | 0.092 | 0.109 | 0.078 | 0.101 |
| $\sigma_{b_u}$ | 2e-4 | 3e-5 | 3.2e-5 | 1.1e-5 | 2.1e-5 | 1.9e-6 | 6.4e-6 | 8.2e-6 | 1e-5 |
| $\sigma_{a_v}$ | 0.021 | 0.367 | 0.245 | 0.076 | 0.087 | 0.165 | 0.099 | 0.023 | 0.032 |
| $\sigma_{b_v}$ | 4e-4 | 2e-4 | 6e-5 | 5.4e-6 | 4.5e-5 | 3e-4 | 4e-4 | 1e-6 | 3e-4 |
| $\sigma_{a_w}$ | 0.064 | 0.010 | 0.087 | 0.087 | 0.078 | 0.164 | 0.082 | 0.099 | 0.026 |
| $\sigma_{b_w}$ | 1.5e-3 | 9e-4 | 1e-4 | 5e-4 | 8e-4 | 2e-5 | 1e-4 | 6e-5 | 3.6e-4 |

Table IV.10: Statistical variation of the IEC Coherence model parameters

## Davenport coherence

The Davenport model coherence was used for the TIMESR inflow turbulence generation. Table IV.11 presents the result of the fitting using 15 cases. Table IV.12 the statistical variations, and Figure IV.12

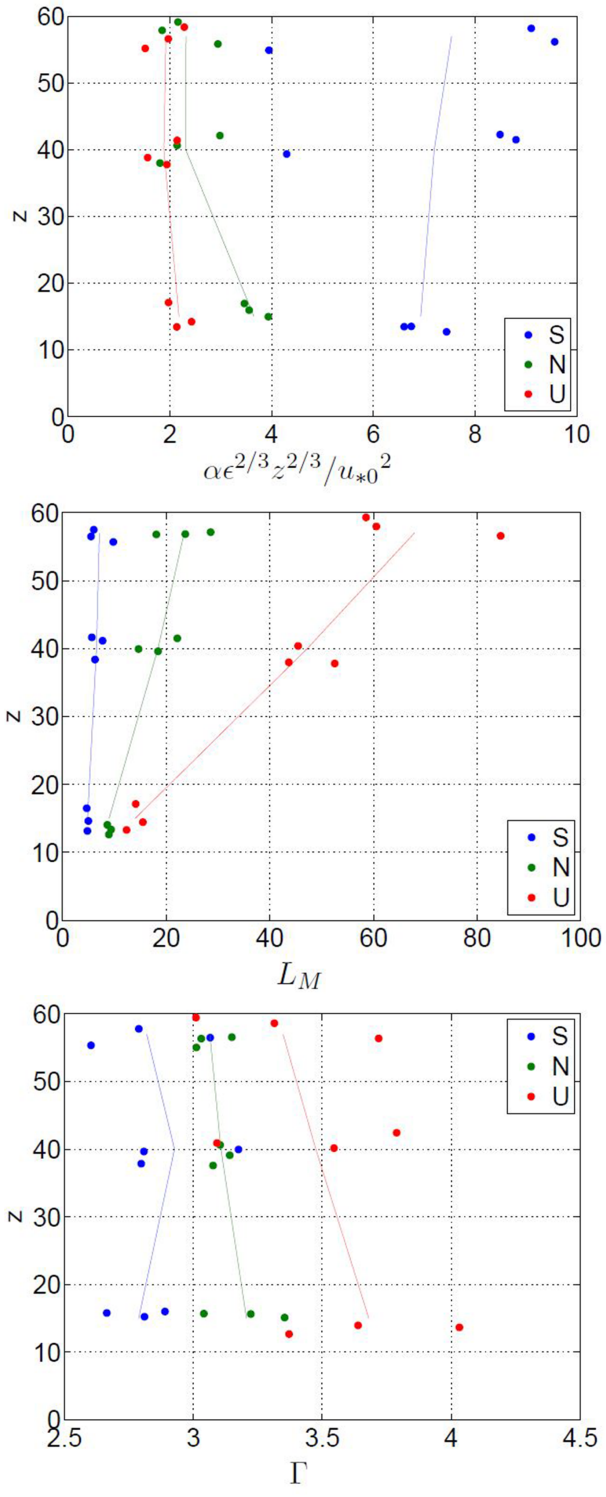


Figure IV.10: *Mann parameters as a function of height from de Maré*[16]

shows the corresponding coherence as a function of reduced frequency.

Similarly, neutral and unstable conditions give a very similar uu-, vv- and ww-coherence that could be explained by the width of the stability classification ranges.

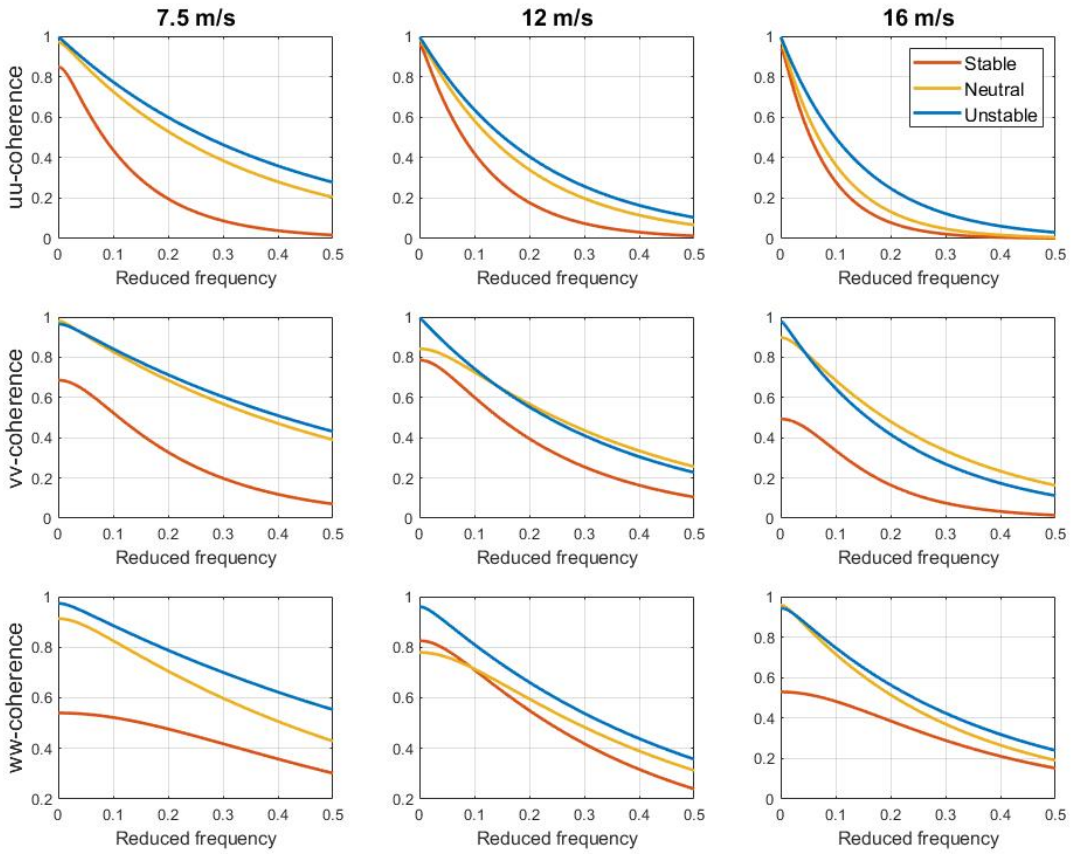


Figure IV.11: *IEC coherence model for all components as a function of wind speed and stability conditions*

| **Stability condition** | Stable | | | Neutral | | | Unstable | | |
|---|---|---|---|---|---|---|---|---|---|
| **Wind Speed [m/s]** | 7.5 | 12 | 16 | 7.5 | 12 | 16 | 7.5 | 12 | 16 |
| $C_u$ | 14.994 | 27.329 | 43.055 | 4.934 | 12.397 | 18.011 | 5.046 | 9.329 | 13.501 |
| $C_v$ | 18.330 | 18.187 | 56.698 | 4.868 | 8.570 | 14.991 | 3.639 | 6.187 | 9.921 |
| $C_w$ | 33.453 | 37.322 | 22.121 | 2.900 | 8.169 | 6.758 | 2.389 | 5.359 | 6.401 |

Table IV.11: Davenport coherence model parameters

| **Stability condition** | Stable | | | Neutral | | | Unstable | | |
|---|---|---|---|---|---|---|---|---|---|
| **Wind Speed [m/s]** | 7.5 | 12 | 16 | 7.5 | 12 | 16 | 7.5 | 12 | 16 |
| $\sigma_{C_u}$ | 1.267 | 3.789 | 8.120 | 0.928 | 1.267 | 3.621 | 1.001 | 1.548 | 3.190 |
| $\sigma_{C_v}$ | 3.107 | 2.341 | 6.980 | 0.629 | 2.512 | 2.389 | 1.325 | 0.523 | 1.478 |
| $\sigma_{C_w}$ | 2.078 | 1.453 | 0.688 | 0.733 | 1.112 | 0.892 | 0.511 | 1.209 | 0.729 |

Table IV.12: Statistical variation of the Davenport coherence model parameters

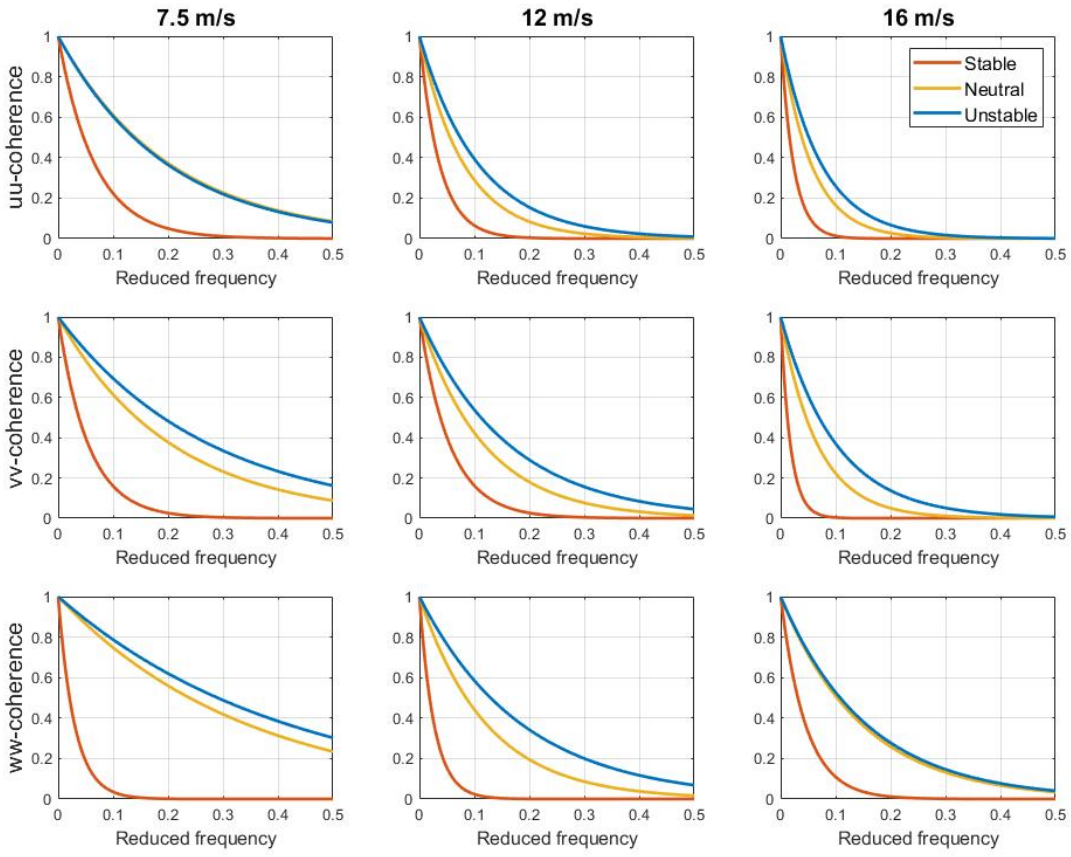


Figure IV.12: *Davenport coherence model for all components as a function of wind speed and stability conditions*

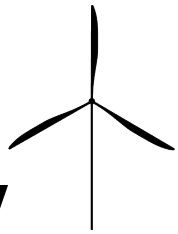

CHAPTER V

# Modeling

To generate inflow turbulence or to simulate the coupled dynamic response of wind turbines, different softwares have been developed. Using open source softwares allow us to perform different analysis without any cost but the computational ones.

## V.1 OpenFAST

One of the softwares used to simulated wind turbines dynamics is OpenFAST[4] developed by the National Renewables Energy Lab (NREL). *"OpenFAST is the framework (or "glue code") that couples computational modules for aerodynamics, hydrodynamics for offshore structures, control and electrical system (servo) dynamics, and structural dynamics to enable coupled nonlinear aero-hydro-servo-elastic simulation in the time domain"*.[4] Figure V.1 presents the OpenFAST submodel hierarchy and more details about the software can be found in the manual.[4]

## V.2 Inflow turbulence generation

OpenFAST allows the inflow to be generated using turbulent wind models (Kaimal, Mann and turbulence from measurements, in this study). TurbSim[48] will be used to generate turbulence for the Kaimal model and from measurements (TIMESR). The DTU Mann 64bit turbulence generator[46] will generate the turbulence for the Mann model. The dimensions of the wind boxes should at least cover the rotor swept area and should be sufficiently long for the time length of the simulation. A simulation time length of 1 hour (plus a 400-second transient) is used for this thesis. During the simulation, the wind box will move in the x-direction at the hub height mean wind speed, accurate box dimensions and box discretization is hence necessary to get different turbulence during the entire simulation.

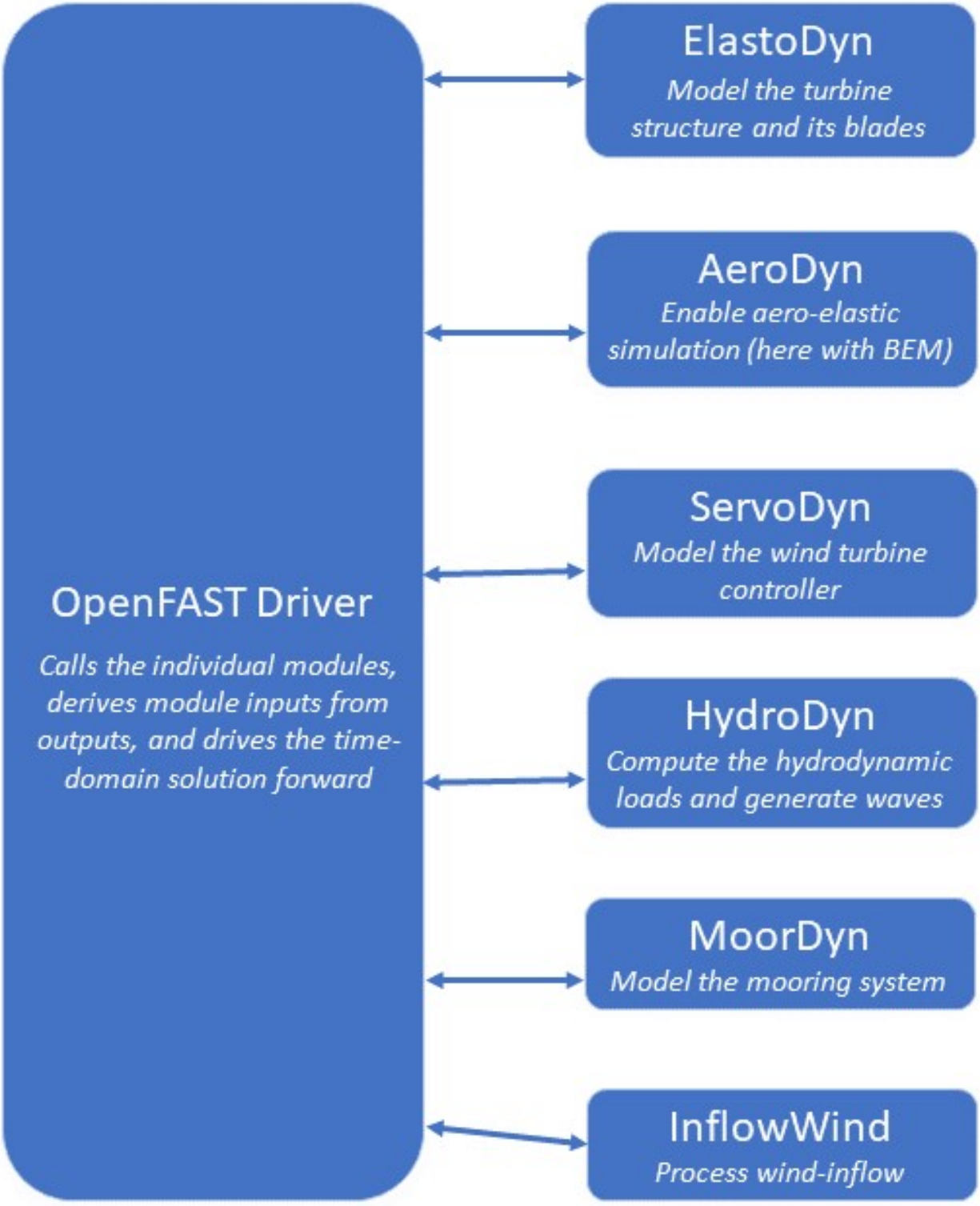


Figure V.1: *OpenFAST organization*

### V.2.1 TurbSim

TurbSim is a stochastic inflow turbulence simulator used to generate turbulent wind field or full-field flow developed by National Renewable Energy Laboratory (NREL). The Veers model is used to generate velocity time series in the u-, v-, w-components at different spatial points on a yz-plane following frozen turbulence Taylor's hypothesis.[68] TurbSim computes the requested spectra for the three wind components at a specific plane point, then Fast Fourier Transform (FFT) are applied to the calculated

spectrum to obtain the turbulence time series.[69] The Shinozuka method allows then the computation of the turbulence time series for the remaining grid points using the coherence function[69] assuming the three turbulence components are independent from each other.

### V.2.2 DTU 64bit turbulence generator

Mann turbulent wind field generated by the Mann turbulence generator is computed from the isotropic von Kárman turbulence spectrum where wind shear effect is later added by introducing anisotropic parameter gamma as the eddies stretch with time. The only constraint on the turbulence generation is on the number of grid points that must be a power of 2 to respect spatial and temporal scales.

### V.2.3 Size of the box

The general idea is to have the same box dimensions for Kaimal, Mann and TIMESR simulations. First, the vertical and lateral dimensions are determined based on the rotor dimensions and the maximum FWT motions. TurbSim[48] suggests the grid height and width to be at least 10% greater than the rotor diameter, in our case at least greater than 196.13 meters. The maximum FWT motions are computed with a steady wind at rated wind speed (11.4 m/s) because of the maximum thrust force that happens at this wind speed. The maximum heave motion is close to 2 meters and the maximum side motion (sway and roll coupled) of the FWT is around 2 meters. It should be noted that maximum heave or sway motions might not happen during this wind conditions but the 10% margin should be enough for the lateral and vertical motion variation.

It is recommended by OpenFAST[4] to choose a vertical and lateral grid spacing to be equal or lower than the maximum blade chord of the wind turbine. While Wise & Bachynski[14] chose a grid spacing of 7.5 meters greater than the maximum blade chord (around 6.2 meters), our choice will be $d_y = d_z = 6.5$ meters, closer to this value. The discretization value was also chosen based on the number of grid points chosen in the lateral and vertical directions. It was shown by Bonnie Jonkman[17] that the computation time in TurbSim is dominated by the Cholesky decomposition of an $n^2$ by $n^2$ matrix at each time step, $n$ being the number of grid points. She showed that the evolution of CPU time was exponential with the increase of grid points as shown in Figure V.2.

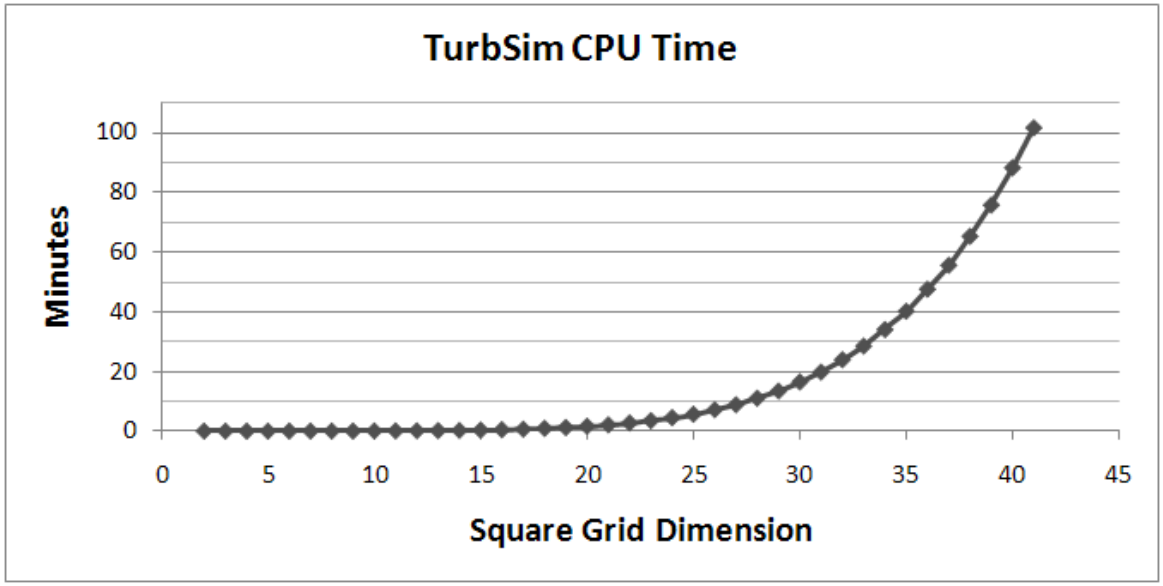


Figure V.2: *TurbSim computational time as a function of grid dimension, by Bonnie Jonkman*[17]

Because of the constraint on number of grid points from the DTU Mann generator[46] and the CPU time evolution, $N_y = N_z = 32$ has been chosen. The grid height and the grid width are then equal to *201.5 meters*.

The length of the box should change with wind speed. Only the DTU Mann generator requires a box length, TurbSim will generate a box length based on a time step and a simulation length. The recommended time step for most simulation is $dt = 0.05$ seconds and our chosen simulation length is $T_{max} = 4000$ seconds. In the DTU Mann generator, the number of grid point in the downstream direction is set to be $N_x = 2^{16}$ and this value was chosen to match the time resolution used in the TurbSim simulations. The spatial resolution in the downstream direction is calculated as:

$$d_x = \frac{T_{max}}{N_x}\overline{u_{hub}} \tag{V.1}$$

This results in $d_x \approx$ 0.46 m, 0.73 m, 0.98 m for the 7.5, 12, 16 m/s scenarios, respectively. The three values correspond to a time resolution of $dt \approx 0.06$ s which closely matches the TurbSim time resolution.

Table V.1 summarizes the turbulence box dimension for both 64bit Mann turbulence generator and TurbSim.

| Generator | Wind Speed [m/s] | Nx | dx [m] | Ny | dy [m] | Nz | dz [m] |
|---|---|---|---|---|---|---|---|
| Mann | 7.5 | 65536 | 0.4578 | 32 | 6.5 | 32 | 6.5 |
| | 12 | | 0.7324 | | | | |
| | 16 | | 0.9766 | | | | |
| | **Wind Speed [m/s]** | **Analysis time [s]** | **dt [s]** | **Grid Height [m]** | **Ny** | **Grid Width [m]** | **Nz** |
| TurbSim | 7.5 | 4000 | 0.05 | 201.5 | 32 | 201.5 | 32 |
| | 12 | | | | | | |
| | 16 | | | | | | |

Table V.1: *Turbulence box input for DTU Mann generator[46] and TurbSim[48]*

## V.2.4 Mann model

Two groups of wind boxes will be generated. One group called Mann-1 will be the group with the fitted parameters, another group called Mann-2 will be made for the sensitivity analysis.

### Mann-1

72 wind boxes were generated for 4 stability conditions (Stable, Neutral, Unstable, IEC), 3 wind speeds (7.5, 12, 16 m/s) and 6 seeds for the fatigue analysis.[70] The simulated cases used the parameters in Table IV.7 and IV.8 and were generated for 6 seeds in order to reduce statistical uncertainties. The results presented in this thesis correspond to the mean of the six 1-hour realizations.

### Mann-2

To perform a sensitivity analysis, the Mann parameters will take three values: their maximum and minimum values obtained from the fitting and the average of the two. The mean wind speed of all simulations was arbitrarily chose at 16 m/s. Table V.2 summarizes the 7 different cases. These values allowed us to study how each parameter influences the FWT dynamics. Similarly, 6 seeds were generated for each situation.

| Cases | $\alpha\epsilon^{2/3}$ | $L$ | $\Gamma$ |
|---|---|---|---|
| Base case | 0.0269 | 49.1232 | 3.3434 |
| $L_+$ | 0.0269 | 81.9723 | 3.3434 |
| $L_-$ | 0.0269 | 16.2742 | 3.3434 |
| $\alpha\epsilon_+^{2/3}$ | 0.0384 | 49.1232 | 3.3434 |
| $\alpha\epsilon_-^{2/3}$ | 0.0154 | 49.1232 | 3.3434 |
| $\Gamma_+$ | 0.0269 | 49.1232 | 4.3312 |
| $\Gamma_-$ | 0.0269 | 49.1232 | 2.3555 |

Table V.2: Sensitivity analysis Mann parameters

### V.2.5 Kaimal model

The Kaimal and coherence model used the turbulence intensity values in Table IV.4 and IV.6, and used the fitted coherence values in Table IV.9. These values were used in TurbSim in addition to the parameters in Table V.1. 6 seeds were generated for each situation.

### V.2.6 TIMESR

TurbSim is commonly used to simulate wind fields according to the IEC wind turbine design standard. Providing time series of measurements to generate turbulence is also possible (TIMESR). With this option, TurbSim calculates the spectral amplitudes of the input time series. The spectral amplitudes of all simulated grid points in a yz-plane are given by linear interpolation of the spectra of the input time series or "nearest neighbor" extrapolation. Spectra of 15 time series from the sonic anemometers at 40, 60 and 80 meters were averaged and the corresponding time series was used as an input. Initially, TurbSim uses Veer's method[69] to generate random phases (dependent on seed) at each simulated point. Thereafter, the phases are modified using a coherence function ensuring proper coherence between all points. In TIMESR, the phases are subsequently shifted so that the input time series of a reference point is reproduced in the output wind field. The measured wind speed at 80 m above the surface is used as reference. This height is chosen due to its proximity to the hub height, assuming that the phase information at this height is more important for the rotor wind field. The Davenport coherence model is used to ensure coherence between the 80-m data and simulated points. Values presented in Table IV.11 are used for the coherence computation.

## V.3 Response

### V.3.1 Spectra computation

The power spectral density (PSDs) values presented in this report are estimated using the WAFO toolbox[71] using the Welch's averaged periodogram method with overlapping batches. For the analysis of flow components, frequencies below 0.003 Hz and above 3 Hz are computed but not plotted for readability.

### V.3.2 Fatigue analysis

OpenFAST computes the interactions between the environment and the FWT using different theories in modules. The outputs can be the wind speed in all direction at any point in space, motions of the platform, displacements of elements but also moments and loads. The tower top yaw moment, $M_{topZ}$,

the tower base fore-aft bending moment, $M_{baseY}$, the fairlead tension of the mooring line 2 (see Figure III.2), $F_{fairten2}$, and the blade root out-of-plane bending moment, $M_{oop}$, are considered in this thesis. Fatigue loading is assessed using short-term damage-equivalent loads (DELs) calculated using NREL's MLife.[72,5] First, the short-term accumulated fatigue damages $D_j^{ST}$ are computed:

$$D_j^{ST} = \sum_i \frac{n_{ji}}{N_{ji}} = \frac{n_j^{STeq}}{N_j^{eq}}, \qquad n_j^{STeq} = f^{eq} T_j \tag{V.2}$$

where $D_j^{ST}$ is the short-term accumulated fatigue damage from time-series $j$, $n_{ji}$ is the $i$th cycle count, $N_{ji}$ is the number of cycles to failure, $n_j^{STeq}$ is the total equivalent fatigue counts, $f^{eq}$ is the DEL frequency here taken as 1 Hz, $T_j$ is the elapsed time of time series $j$ and $N_j^{eq}$ is the equivalent number of cycles until failure. Then, the short-term damage equivalent loads, $DEL_j^{ST}$, are computed:

$$DEL_j^{ST} = \left( \frac{\sum_i (n_{ji} (L_{ji}^R)^m)}{n_j^{STeq}} \right)^{\frac{1}{m}} \tag{V.3}$$

where m is the Wöhler exponent taken as 3 for the steel tower and mooring lines and 10 for the composite blades based on Wise's work,[14] and $L_{ji}^R$ is the cycle's load range without using the Goodman correction.

## V.4 Summary

This section will simply present how the work was organized. The questions of this thesis presented in the introduction can be divided in two groups called work objectives (WO), $WO-1$ and $WO-2$, based on what simulation will be used to answer each question from the introduction.

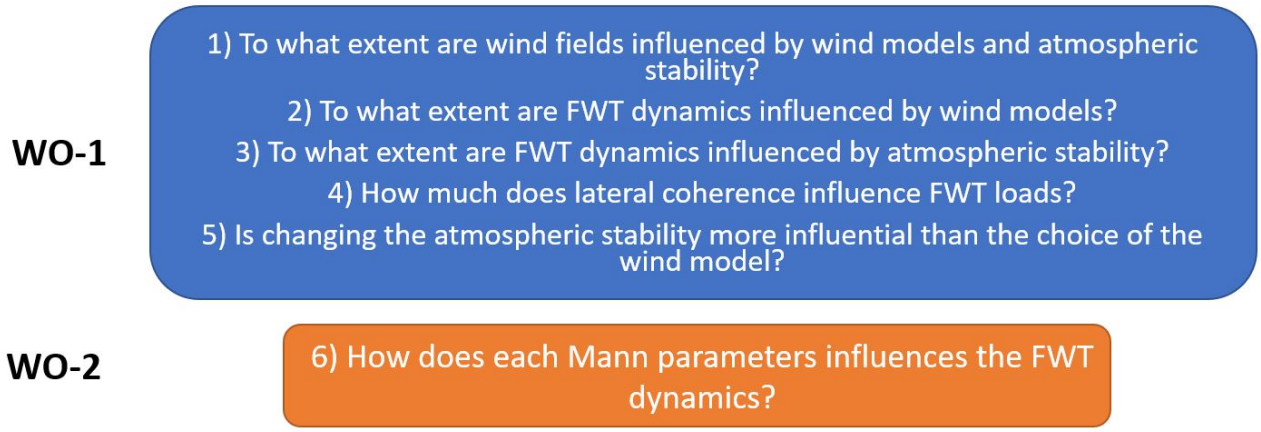


Figure V.3: *Work objectives*

These work objectives will use the simulations presented in Figure V.4.

198 simulations will be used for $WO-1$ and 42 for $WO-2$. It should be noted that the IEC guideline stability condition were not considered for TIMESR simulations because no guidelines are given for this generation method. With 45 minutes CPU time per simulation, all the runs are very inexpensive.

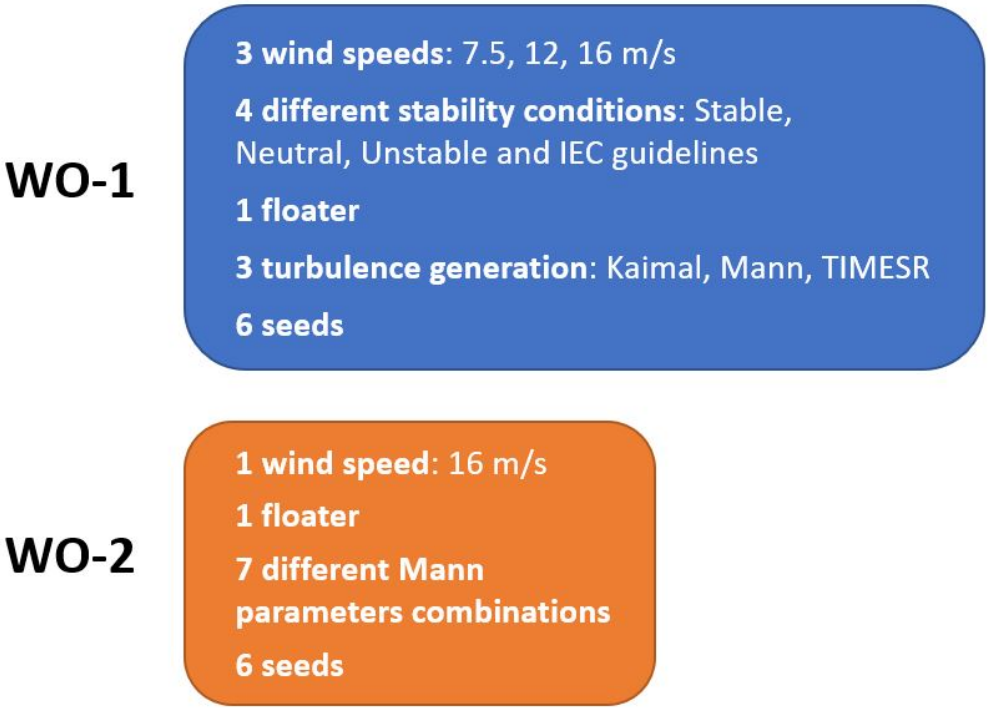


Figure V.4: *Simulations for each work objective*

# CHAPTER VI

# Results

This chapter contains the results from the OpenFAST simulations. The first section presents answers to the work questions with regard to the wind fields, the second section describes the global motions of the FWT. Loads on the turbine are studied in the third section. Finally, the results from the sensitivity analysis are presented in the last section. All the plots presented hereinafter are the average of the six seeds.

## VI.1 Wind fields

Wind fields generated by the three different methods (TIMESR, Mann and Kaimal) are compared to each other. A scaling has been performed on the Mann generated wind fields to match measurement standard deviations (see Table IV.4). On InflowWind, a scaling method allowed the Mann box to reach requested standard deviations. Figure VI.1 shows the longitudinal wind speed standard deviation as a function of mean wind speed for the three different methods and all stability conditions. Mann and TIMESR are slightly shifted to the left and right, respectively, for readability but correspond to the mean wind speed displayed on the x-axis. Figures VI.2 and VI.3 show the lateral and vertical wind component standard deviation. Results were extracted at the hub centre $(0, 0, 119)$ but due to the even number of grid points, there is no grid point exactly at the hub. The standard deviation is the result of an average among the neighbouring grid points hence is slightly lower than the true standard deviation.

Generally, in the longitudinal direction, standard deviation differences between simulations using Kaimal and Mann were negligible for all stability conditions at all wind speed but were all lower than the target standard deviation. TIMESR simulations resulted in standard deviation that were similar to Kaimal and Mann except for the stable condition at 12 and 16 m/s wind speed where the difference was almost 0.1 m/s. This standard deviation scaling allowed us to compare wind fields content without considering the influence of turbulence intensity.

For the v-component wind speed, differences appeared. Since the scaling was based on the measurements and not the Kaimal outputs, Mann standard deviation were different from Kaimal by up to 0.2 m/s in the worst case (unstable, 16 m/s). The results from the IEC simulations were closest to those

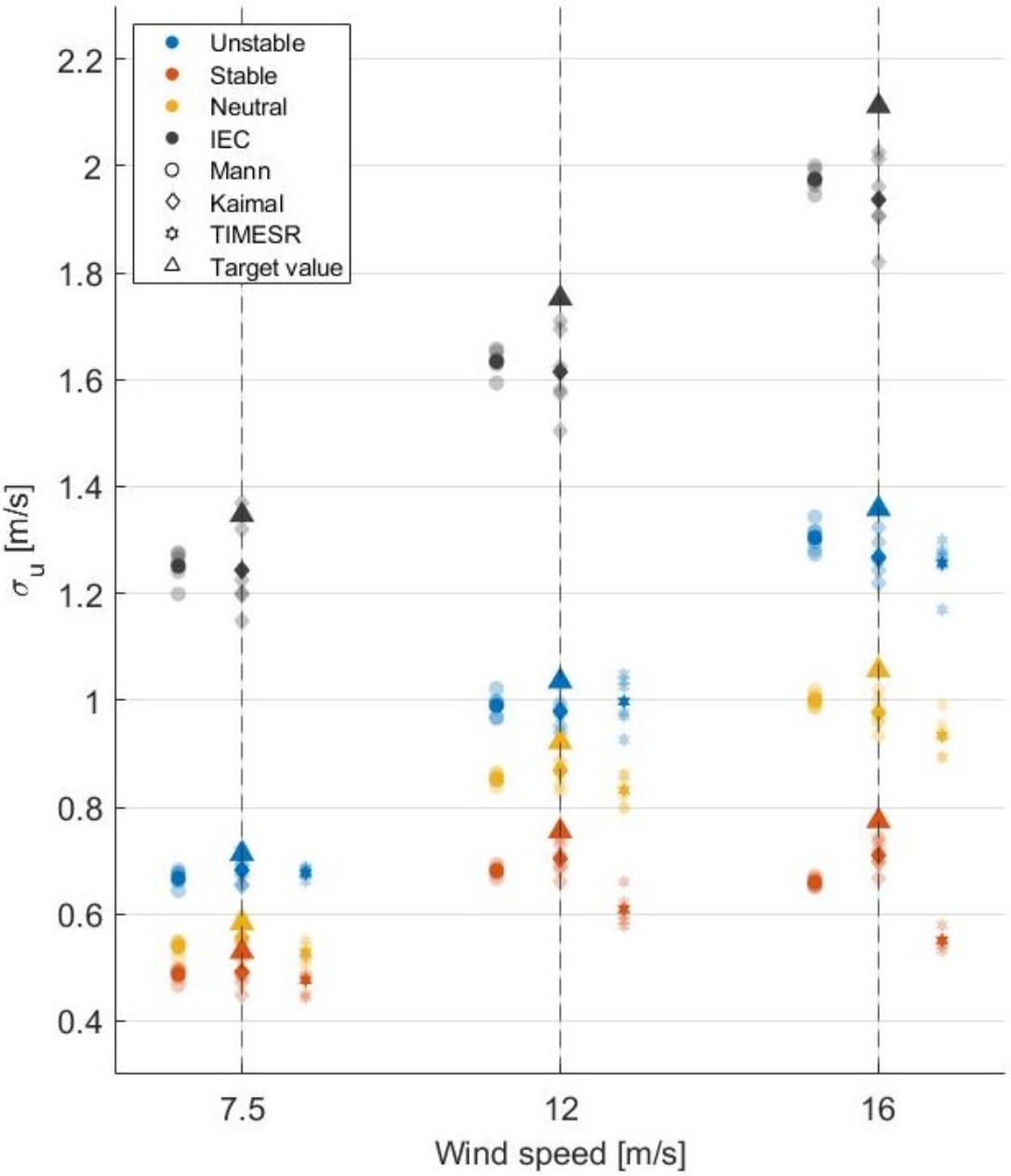


Figure VI.1: *Longitudinal standard deviation as a function of wind speed and atmospheric conditions. The triangle shape represent the target standard deviation and the transparent shapes denote the different seeds*

of the neutral simulations. Generally, stable standard deviations were the lowest and unstable standard deviations the highest as expected. TIMESR simulations showed standard deviations closer to the Mann results for all stability conditions than the Kaimal results.

For the w-component wind speed, differences between models were up to 0.1 m/s (stable 12 m/s). The standard deviations from the IEC simulations were closest to those of the neutral simulations, as for the v-component. Similarly, standard deviations under stable conditions were the lowest and standard deviations under unstable conditions the highest for all wind speeds. The proximity of Mann and Kaimal results to the TIMESR results depends on the wind speed and the stability conditions. Kaimal was closest to TIMESR for neutral conditions at 16 m/s and unstable conditions at 12 m/s. Mann results were the closest in the remaining situations.

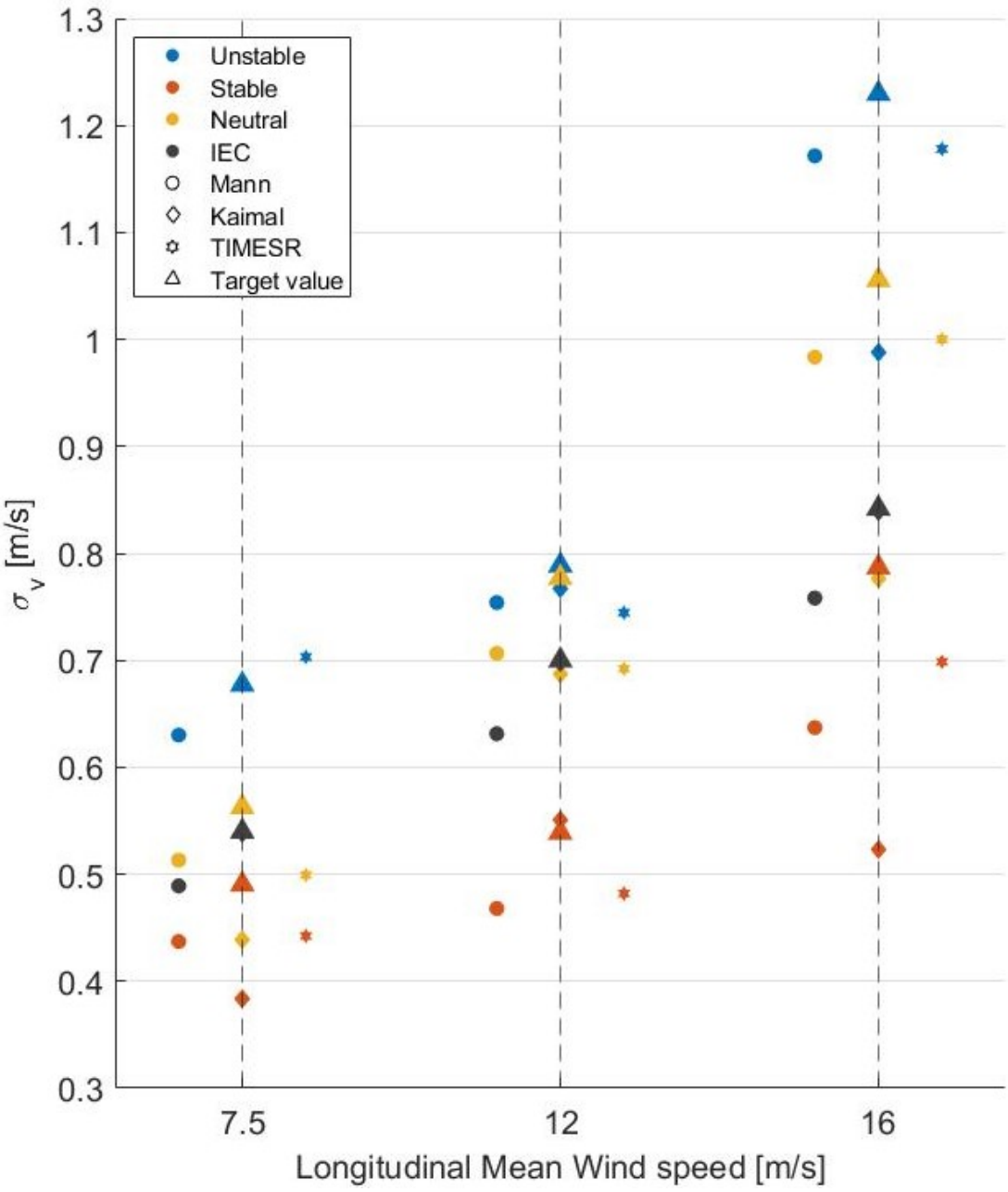


Figure VI.2: *Lateral standard deviation as a function of wind speed and atmospheric conditions. The triangle shape represent the target standard deviation*

### VI.1.1 Wind spectra

It is also interesting to check how similar the power spectral density of the velocity fluctuations are. Figure VI.4 shows the computed spectra at hub centre $(0, 0, 119)$ for all components at 12 m/s as a function of stability. Only the 12 m/s is shown here as trends were identical for the other wind speeds (can be found in Appendix B) and results are shown from $6.3 \cdot 10^3$ to 3 Hz.

In the longitudinal direction, Mann and Kaimal PSDs matched very well for all stability conditions and TIMESR PSDs had, generally, less energy content at lower frequencies (lower than 1 Hz) but more at higher frequencies (greater than 1 Hz). The spectra obtained by the three generation methods should show similarities in energy content in the low-frequency range as they have the same turbulence intensity.[26] Nonetheless, at 12 m/s under stable conditions, TIMESR showed a lot of difference in the energy content in this frequency range. The area under the spectra was lower than that of Mann and

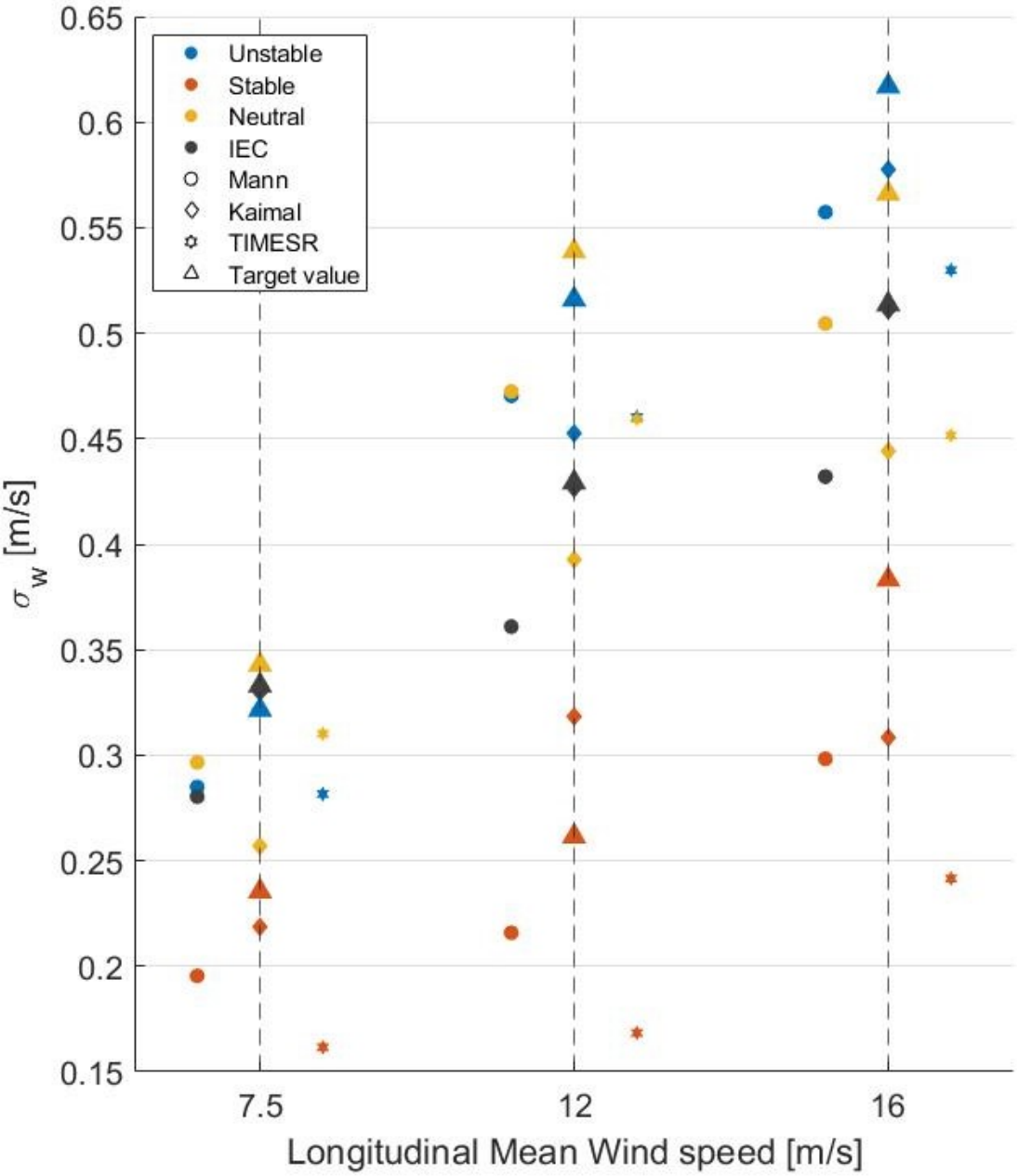


Figure VI.3: *Vertical standard deviation as a function of wind speed and atmospheric conditions. The triangle shape represent the target standard deviation*

Kaimal, although the standard deviation was similar. It might be due to the fact that the Matlab function providing the power spectral density did not compute values for frequencies lower than $6.3 \cdot 10^3$ Hz. The time series (see Figure VI.5) shows that the high amplitude of the low frequency sample could lead to a high energy content in the very low frequency range not shown in the graph. Including this energy content in the computation of the area under the spectra should give the same value for TIMESR, Kaimal and Mann. Since the low frequency range is more important for floater behaviour, this difference was borne in mind for the next results.

In the lateral direction, Mann and Kaimal matched well in the low frequency range but Mann resulted in less energy content at higher frequencies. Similarly to the u-component, TIMESR simulations energy content was lower at all frequencies higher than 0.1 Hz for all stability conditions. In the low-frequency range, the three generation methods gave similar energy content. In the w-component, Mann resulted in less energy in the high-frequency range for all stability conditions and depending on the stability condition, differences were seen in the low frequency range. TIMESR PSDs had less

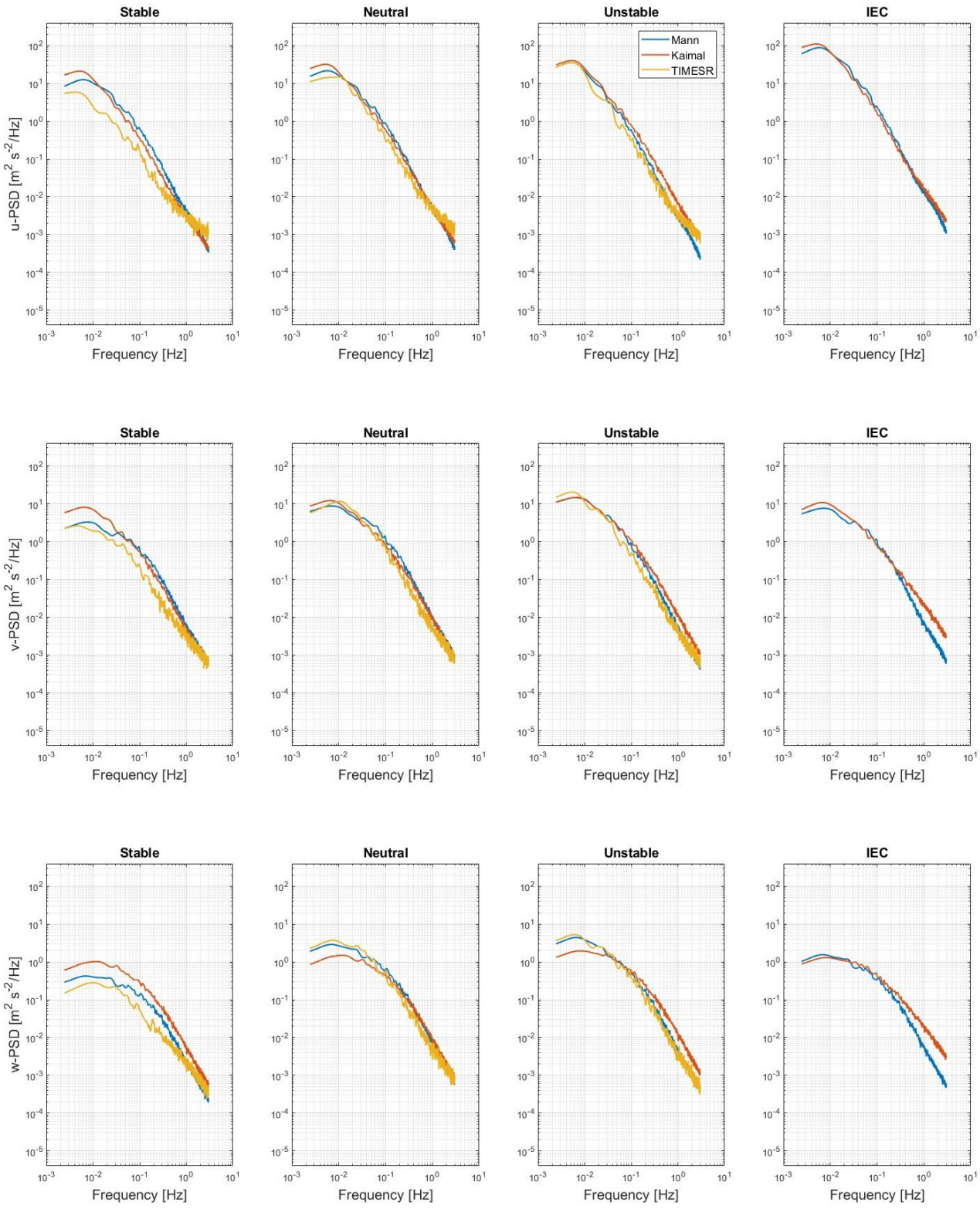


Figure VI.4: *Power spectral density at hub centre at 12 m/s mean wind speed*

energy content at high frequencies and what was observed for stable condition in the u-component was also true, although closer to the Mann energy content.

As expected, for the u-component, stable conditions resulted in the lowest energy content in the low frequency range than neutral and unstable. IEC conditions resulted in the highest showing the influence of turbulence intensity. The energy levels in the lateral and vertical directions of the IEC condition were similar to the neutral condition. This result was expected as the IEC models should represent

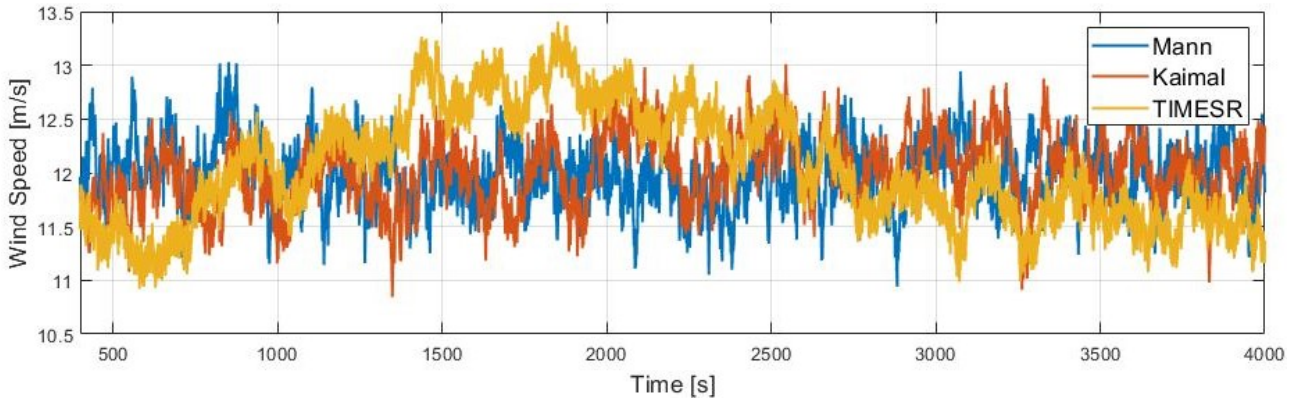


Figure VI.5: *Wind speed at hub height in stable conditions for a 12 m/s mean wind speed*

neutral conditions.

## VI.1.2 Wind coherence

Because we are interested in investigating the effect of lateral coherence on the FWT dynamics, coherence should be compare across the three different turbulence methods. Although, according to the literature,[73,74] longitudinal coherence is most relevant for wind turbine control, most load studies considered lateral and vertical coherence. Vertical and lateral coherence of the longitudinal wind component were used to explain the global motions and loads results presented hereafter.
Because only vertical measurements were available, the vertical coherence between hub height and a point at 99 meters high in the same x-plane was studied to compare the models, the coherence from the OpenFAST simulations and measurements (see Figure VI.6). The wind speed considered was 12 m/s. Other wind speed can be found in Appendix C. Mann coherence from the model was computed using Cheynet's algorithm.[27] Lateral coherence is presented in next figures.

First, for each velocity component, the coherence decreased with reduced frequency in all turbulence models reaching around zero above reduced frequency equal to 0.5 as shown by Panofsky and Singer.[75] This low reduced frequency range below 0.5 correspond to the range where FWT natural period are. Indeed, for the spar, the longest natural period is that of the surge motion (102.4 seconds) corresponding to reduced frequencies in the range 0.0123 for 16 m/s to 0.0261 for 7.5 m/s.

The models' coherence in the longitudinal velocity component were generally higher following the Kaimal model until intersections between Kaimal and Mann, and Kaimal and TIMESR. The intersection appeared at a reduced frequency of 0.1 in the u-component for Kaimal and Mann (0.2 for Kaimal and TIMESR). Kaimal always resulted in higher coherence in the v-component, and Mann always resulted in higher coherence in the w-component. Mann, Kaimal and TIMESR models showed, as expected,[47] a higher coherence in unstable conditions while the coherence in stable conditions fell sharply with the reduced frequency. Since the IEC Kaimal coherence model only compute coherence in the longitudinal direction, the coherence in the v- and w-component was zero, as shown in Figure VI.6.

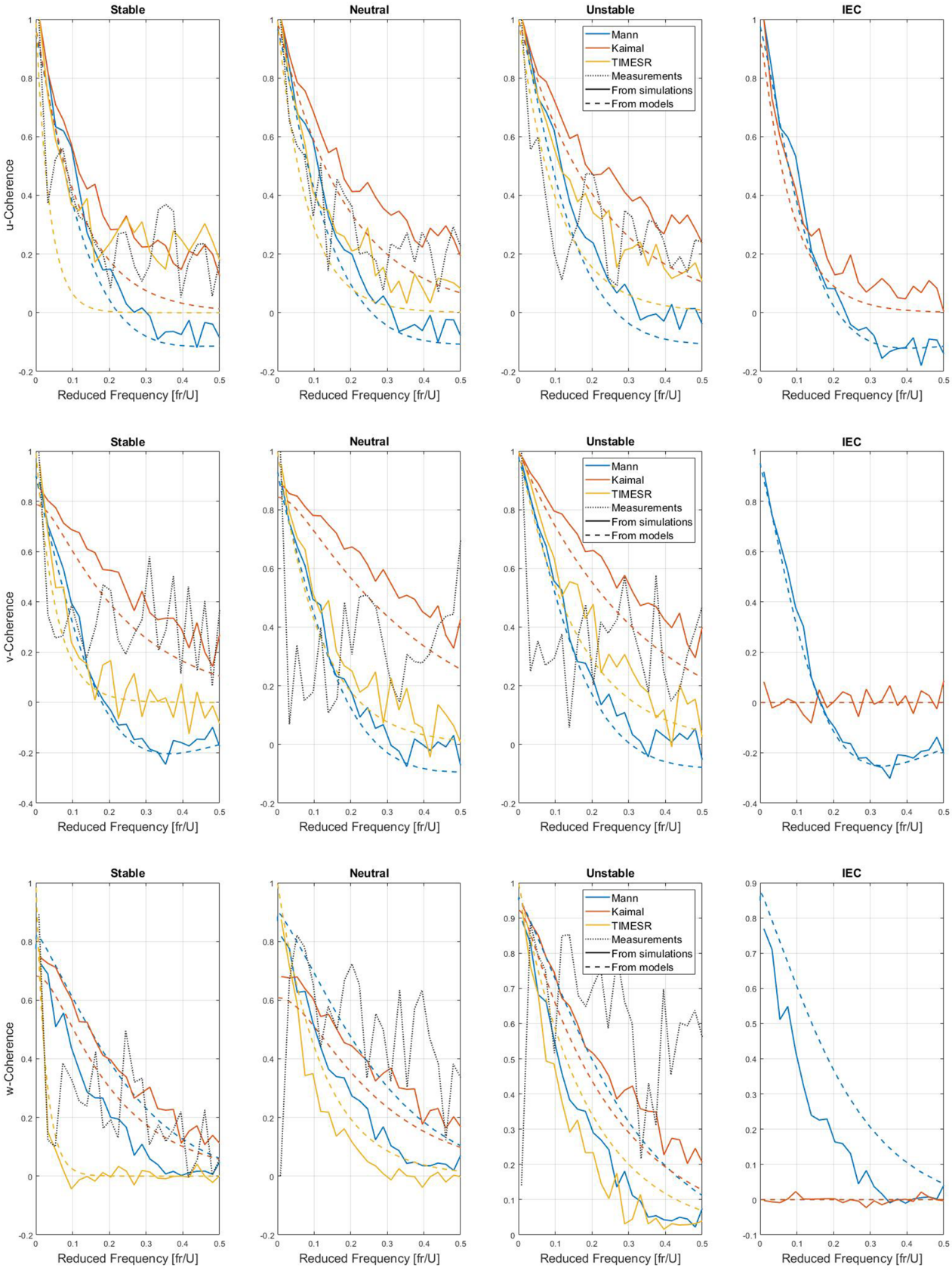


Figure VI.6: *Coherence of three velocity components between hub height and 20 meters below the hub at 12 m/s as a function of reduced frequency*

**Coherence from models:**
In the u-component, Mann coherence from the model matched TIMESR Davenport coherence model

better than Kaimal at the lowest reduced frequencies under neutral and unstable conditions. Under stable condition, at 12 m/s, coherence from the Davenport model fell sharply reaching 0 at a reduced frequency of 0.15. For the coherence of lateral velocity component ($v$), Mann coherence model fitted better to the Davenport model. In the w-component, for all stability conditions, Davenport gave the lowest coherence.

Generally, IEC Mann coherence matched the fitted Mann coherence in stable conditions better. It was also true for 16 and 7.5 m/s. As for IEC Kaimal in the u-component, the coherence matched better at stable conditions although it was lower than the fitted coherence. It was expected to see the IEC models coherence match the neutral conditions better since these models represent neutral conditions.

**Coherence from simulations:**
When comparing coherence extracted from OpenFAST simulations (solid lines), same conclusions can be drawn on the differences between the models. Furthermore, Mann simulations consistently matched better their model coherence in all directions and for all stability conditions. TIMESR and Kaimal simulations matched well their models but were slightly different depending on stability and velocity component. In the u- and v-component, coherence from the simulations were always higher than their corresponding model. The opposite was true for the w-component. When looking at the coherence of the longitudinal wind component ($u$) computed from the simulations, TIMESR resulted in higher coherence than Mann simulations and was closer to Kaimal results.

**Coherence from measurements:**
The measurement coherence values represent the computation of the coherence using the same time series used in the TIMESR generation method, the Davenport coherence fitting, the Mann parameters fitting and the Kaimal coherence fitting. As for the computation of the simulations coherence, measurement coherence computation is the average of 15 cases. TIMESR coherence from OpenFAST simulation fitted better the measurements in the u-component. Concerning the v- and w-coherence, no conclusion can be drawn specifically on the best model. The coherence from the measurements is the highest in the neutral and unstable situations in the w-component. In the stable condition, Kaimal simulation seemed to fit the measurements the best for a reduced frequency above 0.2 Hz.

To study which parameter from the Mann model influence coherence the most, a study is proposed in the last section of this chapter. This allow us understand what atmospheric characteristics influence coherence.

## Quad-coherence

The quad-coherence is only present in the Mann wind fields and in the vertical direction according to the Mann model formulation. Figure VI.7 shows the quad-coherence of longitudinal velocity component at 12 m/s for all stability conditions. Results for 7.5 and 16 m/s are equivalent and presented in Appendix D.

As expected, the coherence was higher than the quad-coherence and Mann quad-coherence computed from the simulations fitted the model quite well. Saranyasoontorn & Veers[49] showed that the quad-coherence was negligible for bottom founded turbines but Nybø[26] showed that the non-negligible quad-coherence lead to a phase shift that will have an impact on the dynamic response of offshore wind turbines. Here, quad-coherence cannot be considered as negligible for the frequency range of interest for FWT and should have an impact on the loads.

The impact of atmospheric stability on the quad-coherence appeared to be negligible but neutral conditions quad-coherence was the lowest at all frequencies.

Kaimal and TIMESR do not represent the phase shift of the coherence as their coherence model is always positive. We might then expect bigger loads on the wind turbine rotor with a Mann generated

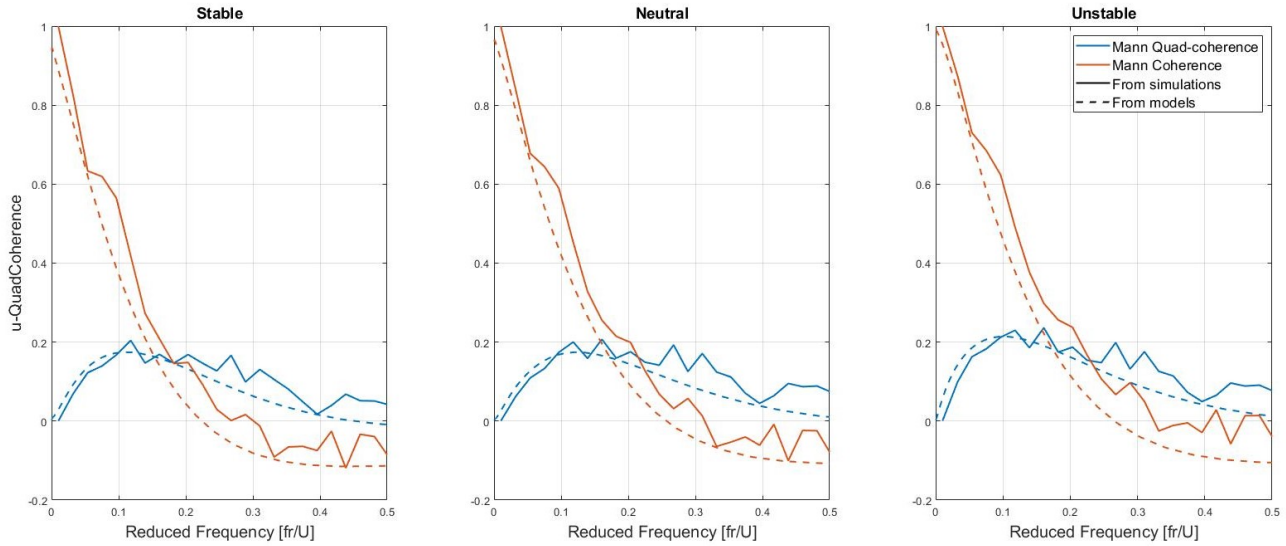


Figure VI.7: *Quad-coherence in the longitudinal direction between hub height and 20 meters below the hub at 12 m/s as a function of reduced frequency*

wind field than with a Kaimal or TIMESR generated wind field.

## VI.1.3 Lateral coherence

Figure VI.8 shows the lateral coherence of the longitudinal velocity component at 12 m/s mean wind speed with a separation distance of $1/2$D between the hub (0, 0, 119) and the rotor border (0, 89.15, 119). Other wind speeds can be found in Appendix E. Here, differences between the models are clearer than for the vertical coherence.

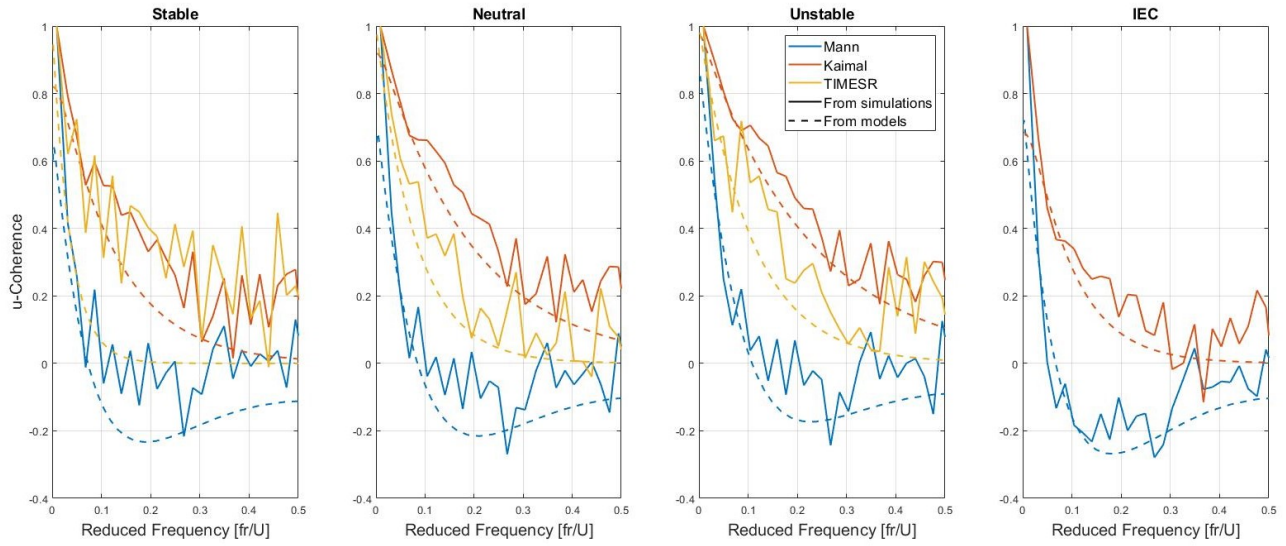


Figure VI.8: *Lateral coherence in the longitudinal direction at 1/2 diameter separation distance at 12 m/s as a function of reduced frequency*

For greater separation distances, coherence decreases as expected.[21] Mann model seems to be the most affected by the separation distance as it gave the lowest coherence for all stability conditions at all reduced frequencies. The impact of atmospheric stability on lateral coherence was similar to vertical coherence: coherence decreased with increasing stability. This great separation distance allows

the study of large coherent structures that influence the global motions of the platform and loads on the structure. Similar to the vertical coherence computation in Figure VI.6, coherence from TIMESR simulations was the closest to coherence from Kaimal simulations under stable conditions. The observations on the coherence from IEC models in the previous section were also true for the lateral coherence: IEC Mann coherence matched the fitted Mann coherence under stable condition better while IEC Kaimal coherence resulted in the lowest lateral coherence in the longitudinal direction.

Since the Mann model does not formulate the quad-coherence in the lateral direction, the quad-coherence of the longitudinal velocity component at 12 m/s mean wind speed with a separation distance of $1/2D$ between the hub (0, 0, 119) and the rotor border (0, 89.15, 119) is zero, as shown in Figure VI.9.

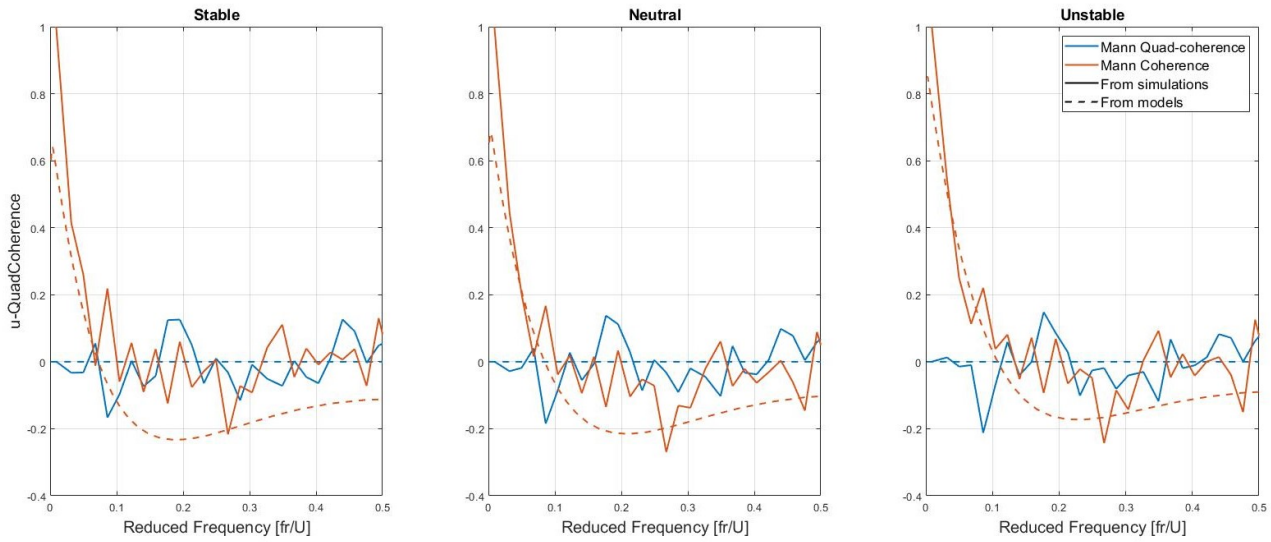


Figure VI.9: *Lateral quad-coherence in the longitudinal direction at 1/2 diameter separation distance at 12 m/s as a function of reduced frequency*

## VI.2 Global motions

In this section, different impacts are discussed. The first subsection presents the influence of the turbulence generation model on the platform motions. The second subsection shows the influence of atmospheric stability on these motions. Standard deviations and power spectral density are used for the analysis.

### VI.2.1 Influence of the turbulence model

The focus of this subsection is on the differences between the three different generation models (Kaimal, Mann, TIMESR). Figure VI.10 shows the standard deviation of surge, pitch and yaw motions for the spar floater as a function of mean wind speed at the hub. Each point represents the average standard deviation from six 1-hour simulations and Mann and TIMESR are both shifted to the left and right, respectively, for readability purposes.

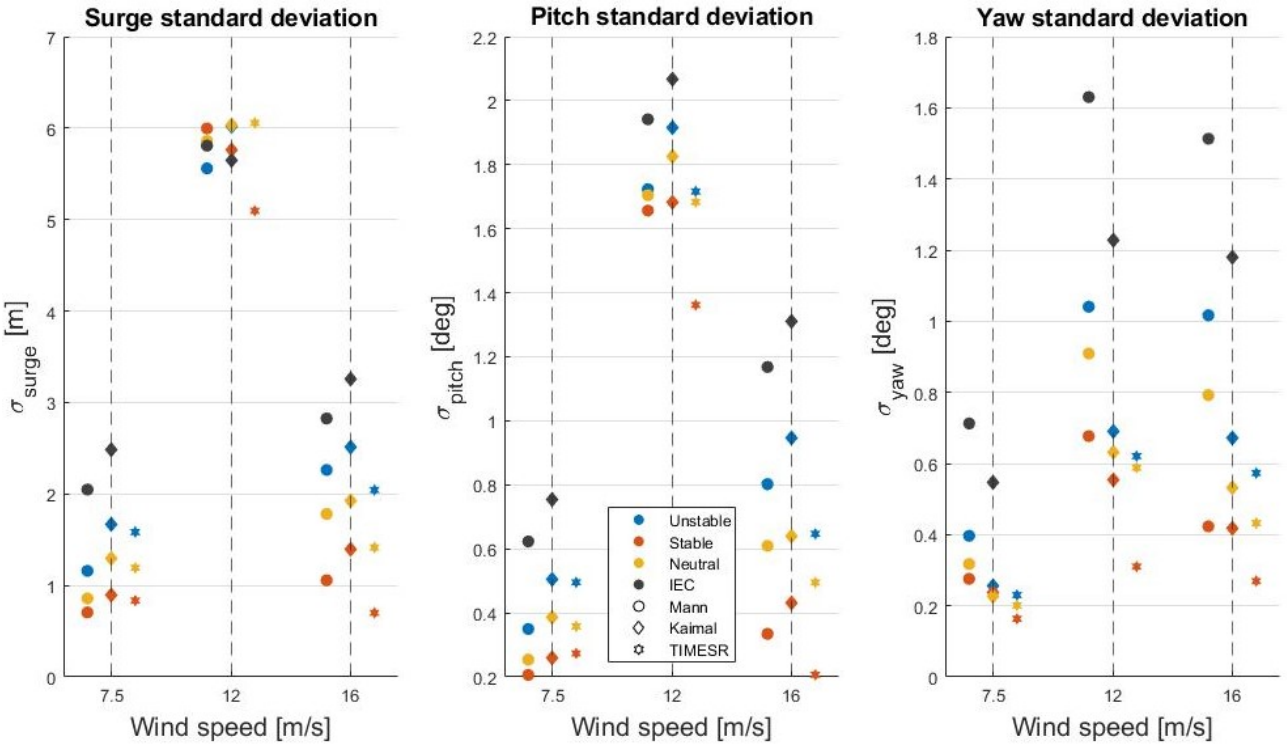


Figure VI.10: *Platform pitch, surge, and yaw motion standard deviations as a function of* $\overline{u}_{hub}$

The pitch and surge standard deviations followed the shape of the mean thrust curve for all stability conditions. Consistently with previous observations,[23] Kaimal simulations resulted in larger standard deviations in surge and pitch for all stability conditions except at 12 m/s for the surge motion. At this wind speed, differences between models depended on the stability conditions: Under IEC conditions, using Mann model resulted in larger motions, while for unstable and neutral conditions, TIMESR simulations dominated and resulted in the same value for both stability conditions and were closer to the Kaimal values. Under stable conditions, Mann gave the largest standard deviation. Although there are differences, these are small compared to the differences at the two other wind speeds and could be explained by the fact that the surge natural frequency (0.01 Hz) is smaller than that of the blade pitch controller (0.02 Hz): the controller is thus quicker than the surge motion and resulted in a greater surge response at 12 m/s mean wind speed. Even though the mean wind speed (12 m/s) is above the rated wind speed (11.4 m/s), turbulence in the wind could allow the controller to measure wind speeds below the rated wind speed and switch between the two different regimes.

For a 16 m/s mean wind speed, Mann resulted in closer results to TIMESR than Kaimal for surge and pitch motions. The opposite was true for 7.5 m/s mean wind speed. Although the standard deviation for stable condition resulting from TIMESR simulations was 20% lower than the value resulting from Mann simulations, TIMESR pitch standard deviations at 12 m/s were closer to the Mann standard deviations than the Kaimal values. These low standard deviation values for surge and pitch motions at 12 m/s under stable conditions using TIMESR wind generation could be explained by the lower energy content in the wind spectra in the longitudinal wind direction.
At 7.5 m/s mean wind speed, Kaimal resulted in 19% (IEC conditions) to 40% (neutral conditions) higher surge standard deviation results than the Mann model. Differences between the two models under stable conditions were the smallest. At 16 m/s, the largest surge motion percent difference was achieved in stable conditions (27%) while neutral conditions gave the smallest (7.5%). Equivalent values were found for pitch motion (from 5% to 41%) at 16 m/s.

The surge standard deviations differences can be related to the coherence in Figure VI.8. The large coherent structures were spread more uniformly over the rotor for the Kaimal wind model. According to Bachynski and Eliassen,[23] this uniformity resulted in large thrust variations and small out-of-plane forcing. Assuming that vertical coherence differences between models at this separation distance ($1/2$D) are similar for the lateral coherence (see Figure VI.8), the large thrust force variation provided a larger global pitch moment with the Kaimal wind model than with the Mann model explaining the pitch standard deviation differences between the two wind models.

Mann resulted in the largest yaw motions in all stability conditions at all mean wind speeds, and TIMESR the lowest. The evolution of the yaw standard deviation with wind speed was not consistent with Bachynski and Eliassen[23] findings who found an increasing yaw standard deviation with wind speed while using a 5 MW floating wind turbine.
In general, TIMESR results were closer to the Kaimal ones. Unstable conditions resulted in the largest percent differences between Kaimal and Mann with an average 35% higher yaw standard deviation with the Mann wind model across the three wind speeds. Generally, stable conditions resulted the smallest percent difference (from 1% at 16 m/s to 15% at 7.5 m/s to 20% at 12 m/s). The IEC conditions using the Mann wind model resulted a 25% higher standard deviation with the three wind speeds.

Since the large coherent structures were spread less uniformly over the rotor for the Mann wind model, greater out-of-plane forcing was present, and it resulted in larger yaw motions with Mann.

The standard deviation of the roll, sway and heave motions are shown in Figure VI.11. Roll and sway motions were small compared to pitch and surge motions and, not consistently with Bachynski and Eliassen,[23] did not increase with wind speed, but rather, followed the same trend as the yaw motion. Nonetheless, their findings on the comparison between Mann and Kaimal were similar: Mann gave larger sway and roll motions than Kaimal and, in our case, than TIMESR. Concerning the heave motion, as the spar-type floater is a cylinder, it is not highly influenced by waves. According to Bachynski and Eliassen,[23] this motion is due "to the pitch and roll motions about a point far below the waterline". Whether Kaimal or Mann dominates the heave motion depended on stability condition, wind speed and can be related to the roll and pitch motions. TIMESR always resulted in the lowest motion, except at 12 m/s for unstable conditions where it was Mann. At 16 m/s, Mann resulted in larger heave motions for stable and neutral conditions. The opposite was true for unstable and IEC conditions. It is difficult to link this result to roll motions and pitch motions as Kaimal gave larger motions for both roll and pitch degrees of freedom at 16 m/s under stable conditions.

Although Kaimal resulted in slightly larger roll motions at 7.5 m/s (from 2% for unstable conditions to 13% for stable conditions (while IEC Mann gave larger standard motions than IEC Kaimal), use of the Mann model resulted in larger roll motions at 12 m/s and 16 m/s. The largest difference at 12 m/s happened under neutral conditions (28%) and under IEC conditions at 16 m/s (15%).

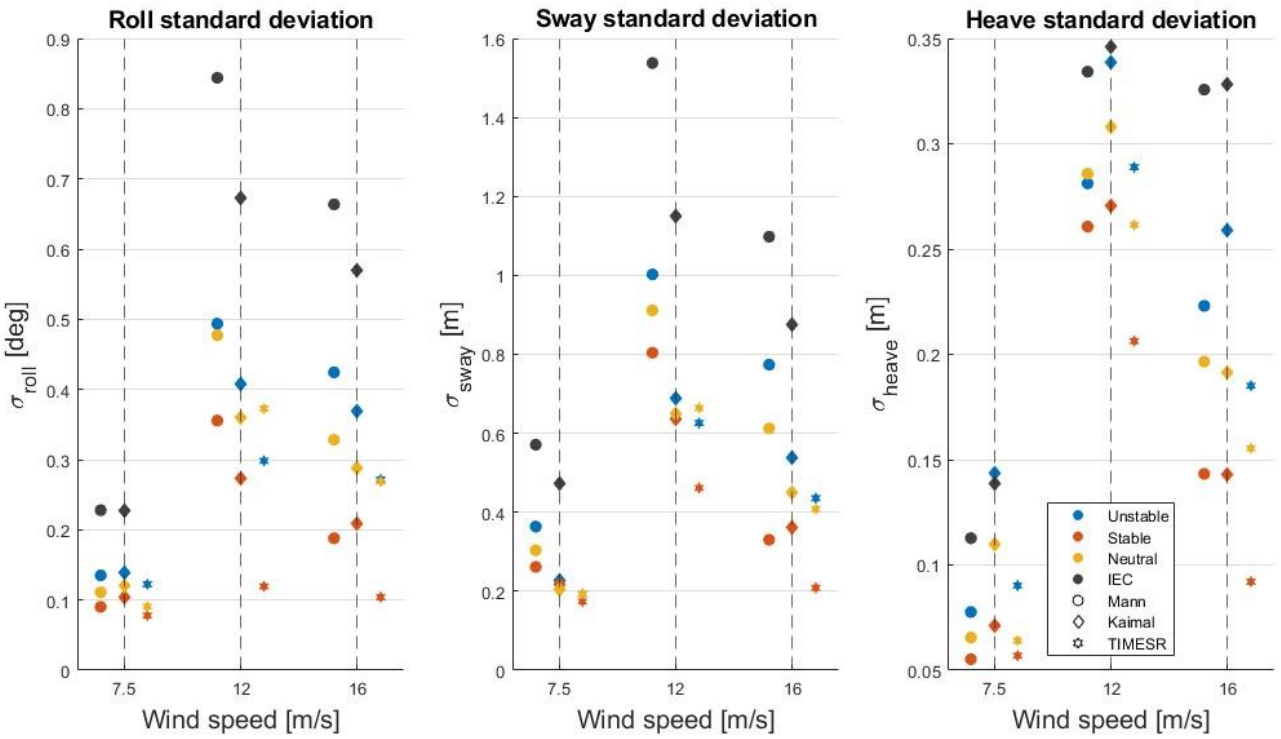


Figure VI.11: *Platform roll, sway and heave motion standard deviations as a function of* $\overline{u}_{hub}$

Unstable conditions resulted in the largest sway motion percent difference between the wind models at all wind speed with 40% higher motions using Mann wind model. The smallest sway motion percent difference were found under stable conditions. While using Mann model generally gave larger sway motion than Kaimal model, stable conditions at 16 m/s showed an opposite behaviour with a 9% higher motion with the Kaimal wind model.

According to Bachynski and Eliassen,[23] the sway and roll motions differences can be understood like the yaw motions: the yaw moment resulting from the non-uniformity of the wind field across the rotor and a larger sideways force component. A simulation with an isolated rotor should suffice to verify that using Mann wind model results in a larger sideways force component.

Power spectral density should give an insight on the mechanics that lead to these differences. Figure VI.12 shows the motions responses at 16 m/s wind speed. A zoom in a higher frequency range (0.06 to 0.7 Hz) is proposed as well. Other wind speeds can be found in Appendix F. The responses in surge and pitch at low frequencies were larger for Kaimal and lower for TIMESR. This was true for all stability conditions and it translated to the differences in standard deviation. The differences between Kaimal and Mann were also consistent with Bachynski and Eliassen[23] findings. In the higher frequency range, the wave frequency response was independent of the turbulence model, and the response was negligible for frequencies higher than the wave frequency. The amount of energy in the low frequency range was strongly linked to the standard deviation differences: response for neutral conditions with the Kaimal model being larger and response for stable conditions with the TIMESR model being the smallest. It should also be noted that the surge response at the pitch natural frequency increased with wind speed, being nearly negligible for 7.5 m/s mean wind speed.

Consistent with Bachynski and Eliassen,[23] the yaw response was higher when Mann was applied and was mainly quasi-static at low frequencies. The response at the rotor frequency (1P) was explained by Bachynski and Eliassen[23] and is "understood to be related to turbulence sampling". Hence, due to the proximity of the 1P frequency and the yaw natural frequency, the response was non-negligible.

Similarly to surge and pitch, the corresponding sway and roll motions responses were higher when

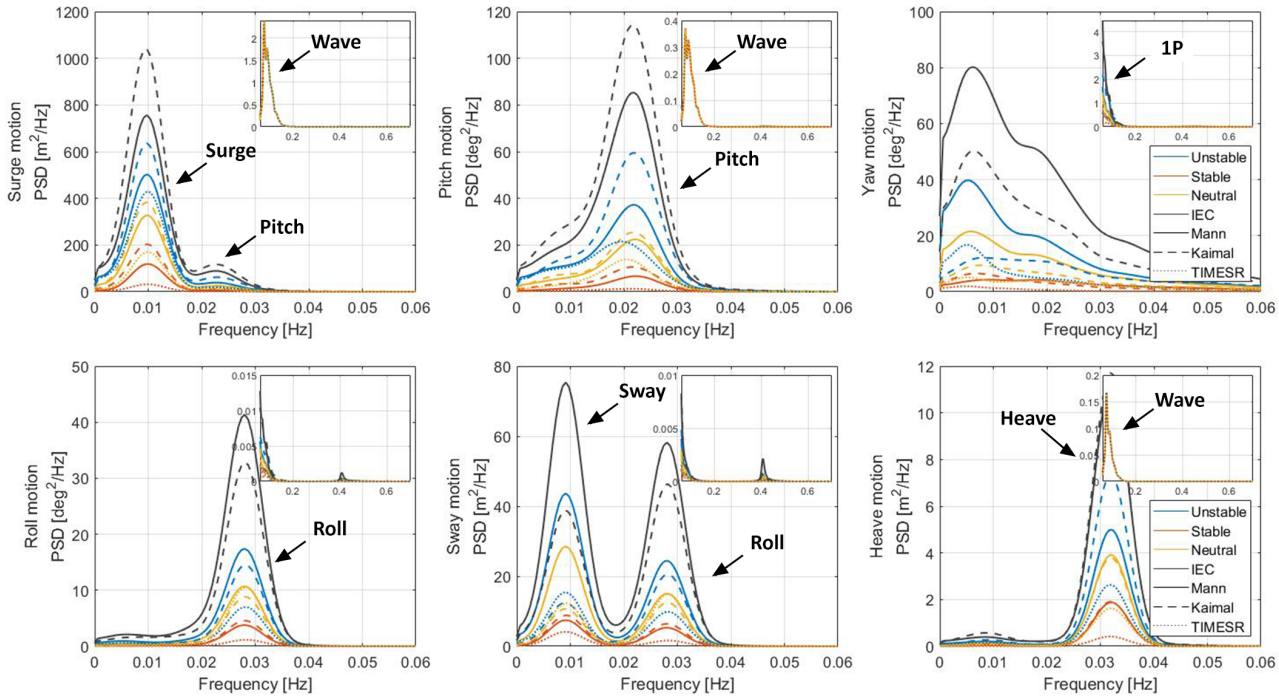


Figure VI.12: *Platform motions PSDs at 16 m/s*

Mann was applied and both sway and roll natural frequencies were present in the sway response. There was negligible response in the higher frequency range, as expected and found by Bachynski and Eliassen.[23]

Concerning the heave motion, resonant responses at the heave natural frequency dominated for the highest wind speed. Responses at the surge natural period was also non negligible and higher at 12 m/s wind speed where the surge motion was the greatest.

**Note on TIMESR results:**
Except for the surge motion at 12 m/s, TIMESR always gave the lowest energy in the PSD hence the lowest standard deviation, for all stability conditions. It could be explained by the fact that the wind spectra energy content in the low frequency was always the lowest, resulting in less energy in the motions spectra. Scaling of the TIMESR turbulence could be an interesting next step to see the influence of the generation method.

## VI.2.2 Influence of atmospheric stability

Figure VI.13 shows the percent difference between all stability conditions and the fitted neutral conditions for the three generation methods for surge, pitch and yaw motions (see Equation VI.1). The same figure for roll, sway and heave motions can be found in Appendix G.

$$PercentDifference = \frac{\sigma_k(stability) - \sigma_k(neutral)}{\sigma_k(stability)} \cdot 100 \tag{VI.1}$$

where $k$ denotes the motion considered (surge, pitch, yaw, roll, sway, heave) and $stability$ denotes the stability condition (unstable, stable, IEC). Even though the IEC standard models aim at representing neutral conditions they represent different stability conditions in this thesis because of their different model parameters.

Generally, IEC conditions dealt more motions at all wind speeds for the three generation models than unstable, neutral and stable conditions. The exception was for the surge motion at 12 m/s where stable conditions with Mann model and unstable conditions with Kaimal model lead to more motion.

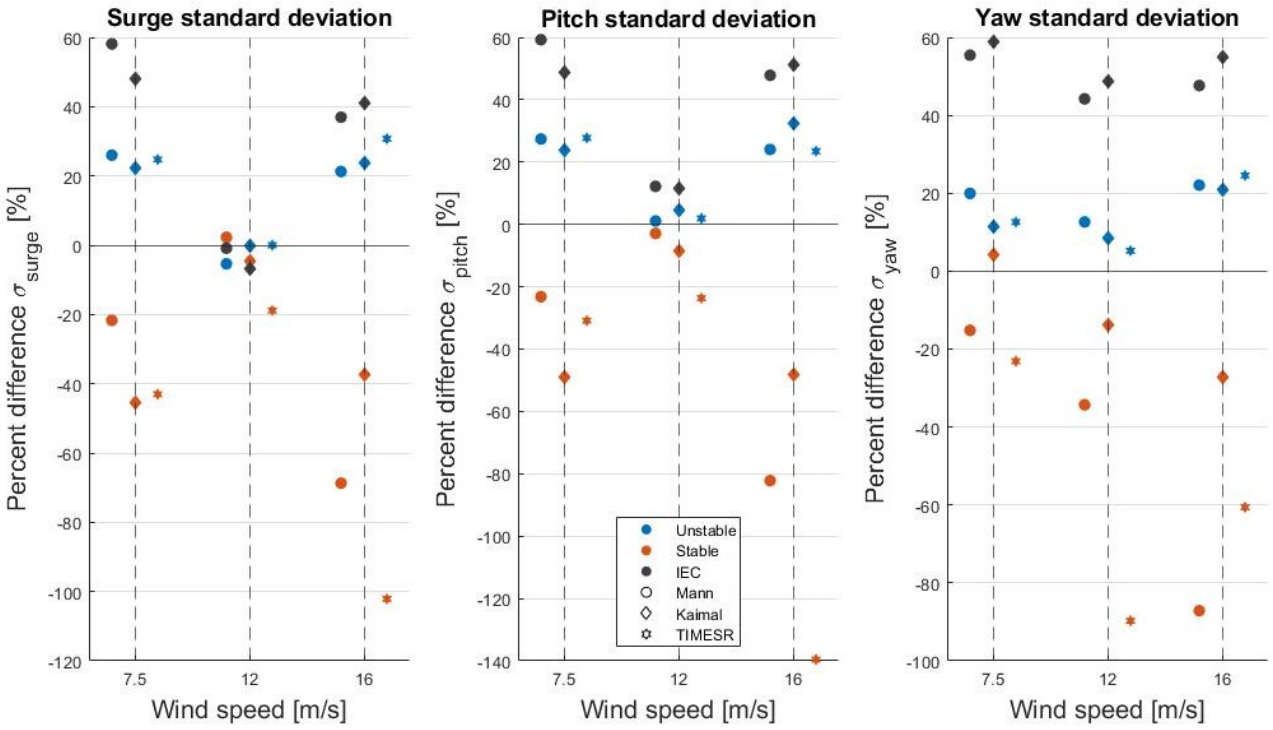


Figure VI.13: *Platform pitch, surge, and yaw motion percent difference standard deviations between stability conditions and neutral conditions as a function of* $\overline{u}_{hub}$

The lowest atmospheric stability impact happened for the surge motion at 12 m/s but it was explained by the controller higher natural frequency. For the other wind speeds, coherence plots (see Figure VI.8) can explain the differences between stability conditions i.e. stable coherence was the lowest while unstable coherence was the highest. This led to less motion in stable conditions and more in unstable conditions. The same observation can be made for the pitch motion.

While differences in yaw motion between the three generation methods were explained by their differences in coherence, the same conclusion is not true when it comes to stability condition differences. Indeed, yaw motion was higher with Mann wind model because of the less uniform wind flow across the rotor, i.e. less lateral coherence. Nonetheless, coherence increased with decreasing stability but unstable conditions still led to more yaw motion.

Motions are not only influenced by the coherent structures but also the turbulence intensities. Surge and pitch motions differences at 7.5 m/s and 16 m/s followed the same trend as the turbulence intensities. With increasing turbulence intensity, motions increase. This is also true for the yaw motion at all wind speeds. Studying how much coherence or turbulence intensity impacts the yaw motion is not studied here but recommended for future work.

## VI.2.3 Design standard models or stability conditions

This subsection discusses whether the difference between atmospheric stability leads to greater motion differences than the difference between Mann and Kaimal wind models. Figure VI.14 shows the percent difference between Kaimal and Mann models at all stability conditions and wind speeds for surge, pitch and yaw following Equation VI.2:

$$PercentDifference = \frac{\sigma_{Mann}(stability) - \sigma_{Kaimal}(stability)}{\sigma_{Mann}(stability)} \cdot 100 \tag{VI.2}$$

where $stability$ denote the stability condition (unstable, neutral, stable).

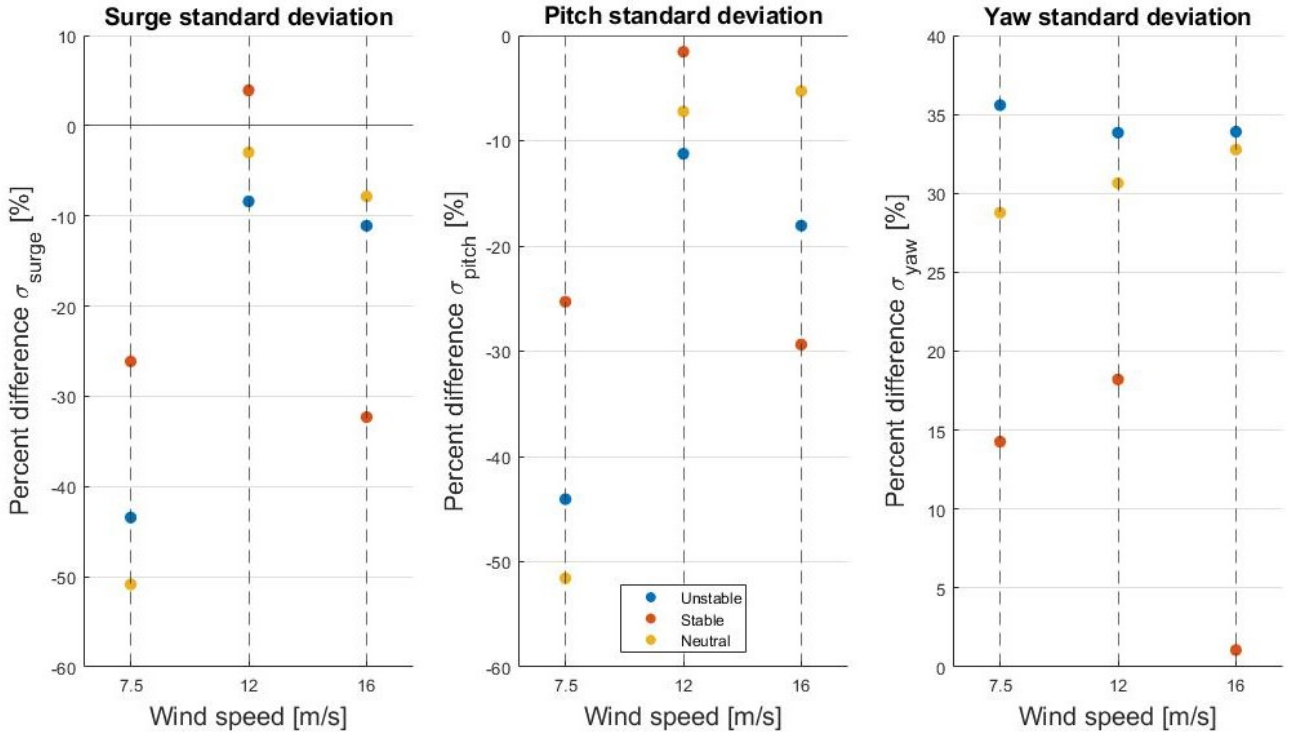


Figure VI.14: *Platform pitch, surge, and yaw motion percent difference standard deviations between wind models as a function of* $\overline{u}_{hub}$

Figures VI.14 and VI.13 are used to answer the question. IEC conditions are disregarded in this subsection as they represent neutral conditions with a conservative ($90^{th}$ percentile) turbulence intensity. If the percent difference between the models is higher than the percent difference between the stability conditions it would mean that changing the wind model has more impact on the motions than changing the stability condition. Whether the change in model had a bigger impact on the motions than the change in stability conditions depends on the motion considered and the wind speed. The yaw response showed a higher impact of the wind model choice at 7.5 m/s for unstable and neutral conditions. Indeed, unstable conditions dealt 12% to 20% higher motions than neutral conditions for Kaimal and Mann, respectively, while the percent difference between the models was 36% for unstable conditions and 28% for neutral conditions. In stable conditions, changing the model had a bigger impact. Same conclusions can be drawn for 12 m/s and 16 m/s: changing the atmospheric conditions using Mann model has more impact on the yaw motion than with Kaimal model.

Pitch motion showed the opposite at 7.5 m/s and 16 m/s: changing the stability had a bigger impact on the motions than changing the model. Kaimal model changes in atmospheric stability had generally more impact on the motions than with Mann model. At 12 m/s, although the differences between models and stability conditions were small: the choice of the wind model was more influential. Surge motion showed the same conclusions.

It is difficult to conclude on whether the difference between atmospheric stability leads to greater motion differences than the difference between Mann and Kaimal wind models. What can be drawn from the Figures VI.14 and VI.13 is that atmospheric conditions needs to be taken into account for

both wind models. It was observed that using IEC standard values led to far greater motions than the fitted atmospheric conditions.

# VI.3 Load response

In this section, different impacts are discussed. The first subsection presents the influence of the turbulence generation model on the damage equivalent loads (DELs). The second subsection shows the influence of atmospheric stability on the damages. In this section, standard deviations and power spectral density are used for the analysis. To isolate the effects of motions, wave and rotor frequencies, filtering have been performed using a bandpass Matlab function from Halvor Lie, Marintek. The ranges were 0 to 0.06 Hz to isolate the effect of the platform motions and 0 to 0.1Hz to add the effect of wave and 1P frequency loading to motions. The DELs computed from the filtering can be found in Appendix H.

## VI.3.1 Influence of the turbulence model

Similarly to the global motion subsection, the focus of this subsection is on the differences between the three different generation models (Kaimal, Mann, TIMESR). Figure VI.15 shows the damage equivalent loads in the tower top yaw moment, $M_{topZ}$, the tower base fore-aft bending moment, $M_{baseY}$, the fairlead tension of the mooring line 2, $F_{fairten2}$, and the blade root out-of-plane bending moment, $M_{oop}$, for the spar floater as a function of mean wind speed at the hub. Each point represents the DEL from six 1-hour simulations and Mann and TIMESR are both shifted to the left and right, respectively, for readability purposes.

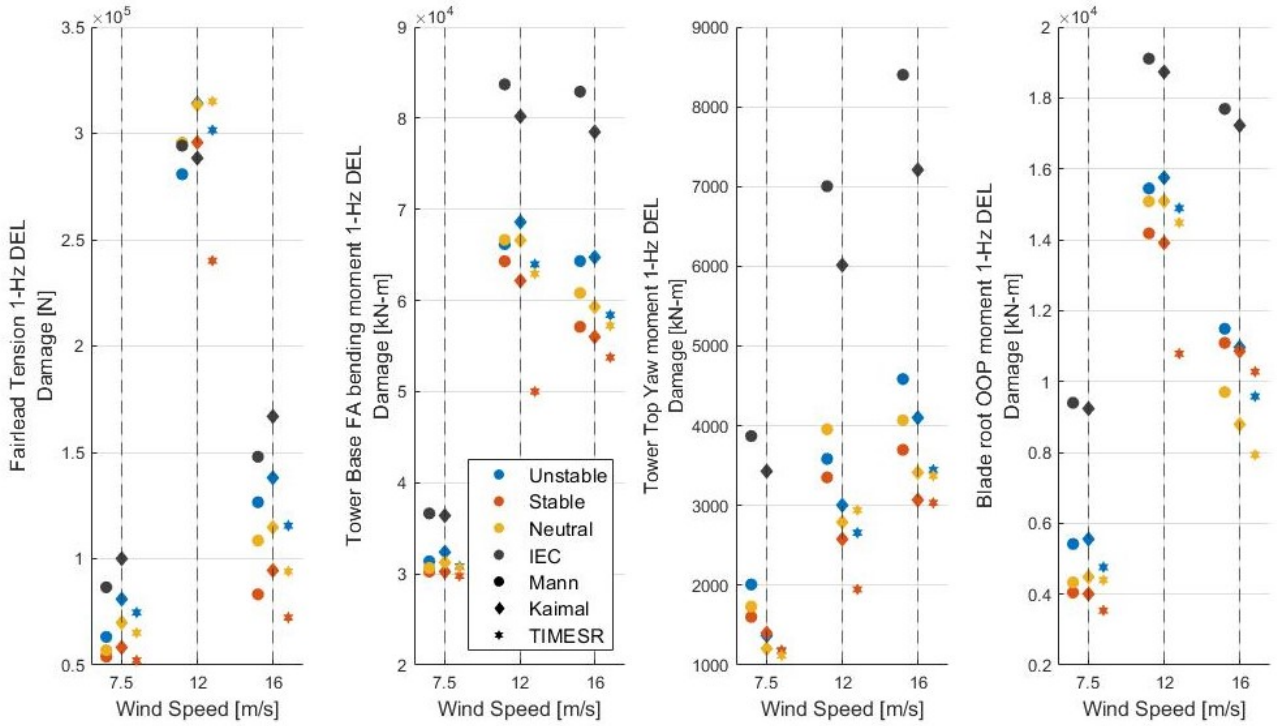


Figure VI.15: *Damage-equivalent loads as a function of* $\overline{u}_{hub}$

The fairlead tension damage was most sensitive to the surge motion as it follows the surge motion standard deviation trend. As shown in Figure VI.16, this damage depended on the surge frequency loading. At the 7.5 and 16 m/s wind speeds, Kaimal predicted more fatigue damage than Mann and

TIMESR. Kaimal predicted the closest results to TIMESR at 7.5 m/s but the opposite was true at 16 m/s. Similarly to the global motion, the fairlead tension damage at 12 m/s was not very sensitive to the choice of turbulent wind model, although TIMESR predicted significantly lower damage in stable conditions.

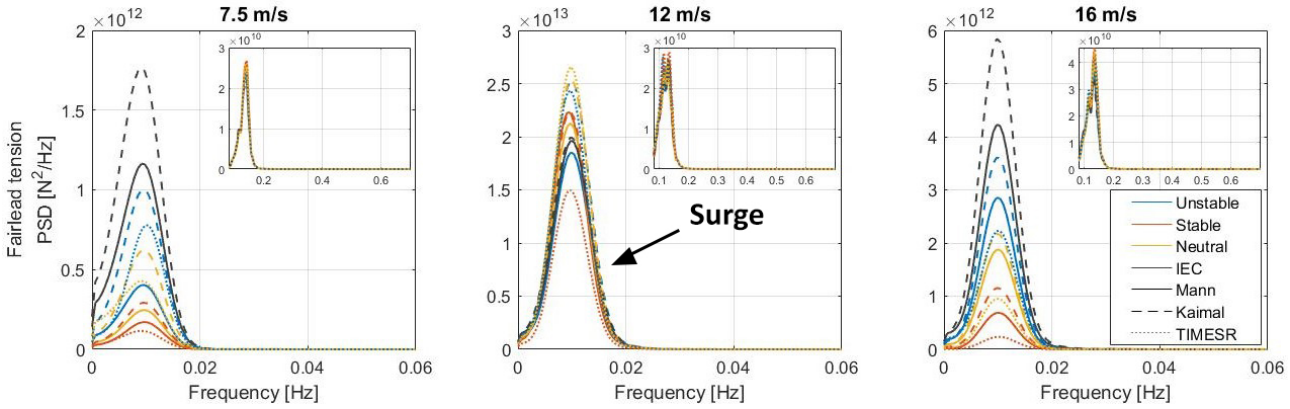


Figure VI.16: *Mooring line 2 tension spectra at each wind speed*

Consistent with Bachynski and Eliassen[23] findings, the tower base fore-aft bending moment damage was not very sensitive to the choice of turbulent wind model. It was true for all stability conditions, although the biggest differences appeared under IEC conditions. TIMESR predicted generally lower damages, the lowest being at 12 m/s under stable conditions. As expected, the largest damages were at 12 m/s because of the high thrust at this wind speed. According to Figure VI.17 that shows the tower base fore-aft bending moment spectra, a strong influence of the 1P frequency loading on the tower base moment damage was found but the biggest energy content came from the motion of the platform. Nonetheless, according to Figure H.1 and H.2, 1P frequency loading doubled the damage at 16 m/s but had less impact at 12 m/s where the surge and pitch motions were greatest. High number of cycles and higher stress range variation could explain the impact of the 1P frequency loading on the tower base bending moment. At 12 m/s, there was a non negligible influence of the tower frequency loading on the damages, specially under the IEC conditions. This might be due to turbulence intensity differences and that the tower frequency is in the 3P frequency range. Figure VI.17 also shows that Kaimal model provided more energy in the low frequency range while giving the lowest energy at the 3P/tower frequency.
These results show that tower base fore-aft bending moment was influenced by the platform pitch motions and corresponding acceleration, gravity loads and the rotor frequencies.

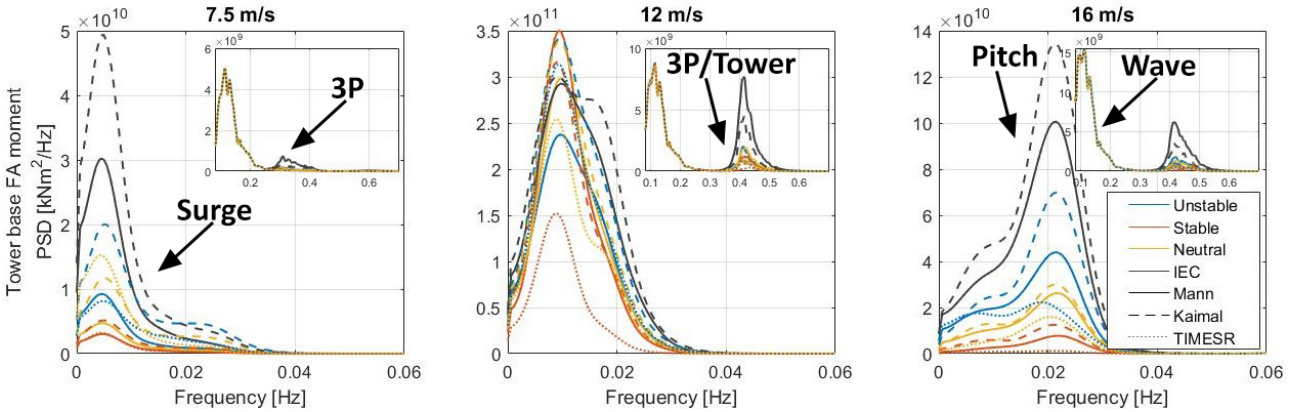


Figure VI.17: *Tower base fore-aft bending moment spectra at each wind speed*

The damage at the tower top yaw moment was consistently higher with Mann wind model, explained by the lower coherence of the Mann wind field that provided a greater yaw moment. According to

Myrtvedt et al.,[29] the quad-coherence should also contribute to the yaw moment. TIMESR predicted lower damages and closer results to Kaimal, explained by the similar lateral coherence of these two wind fields. An interesting result was that using Mann at 12 m/s for neutral conditions gave greater damages than unstable conditions. This was also true for TIMESR and consistent with the spectra in Figure VI.18.

Although there were higher peaks at low frequency, these contributed less than the 3P excitation because of their lower number of cycle and stress range variation. It can be seen in Figure H.1 that low frequency loadings accounted for only a third of the total damage. At 16 m/s, stable conditions using TIMESR model led to a very high peak at the 3P frequency. This translated to a higher damage from loadings at this frequency compared to the other wind model. Nonetheless, TIMESR still predicted less damage when considering all frequencies.

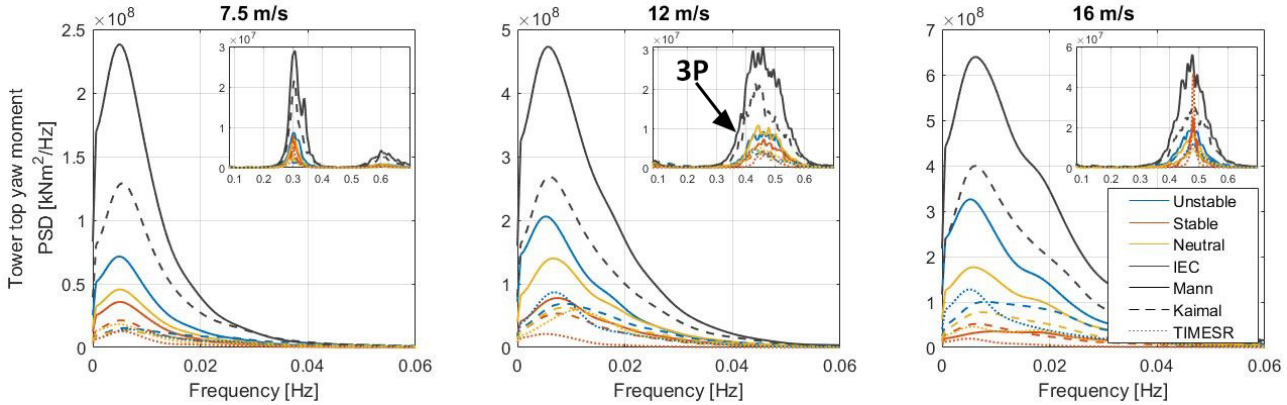


Figure VI.18: *Tower top yaw moment spectra at each wind speed*

The blade root out-of-plane moment damage was not very sensitive to the choice of turbulent wind model. As seen in Figure VI.19, while Kaimal provided more energy content in the low frequency, hence more damage from these frequency variations, Mann had more influence in the higher frequency range. Although 1P frequency excitation had a higher number of cycles, the biggest influence on the blade root out-of-plane moment came from low frequency loadings (75% of the total DELs under all stability conditions), as seen in Figure H.1. Differences between wind models, although very small, could be related to differences in coherence, as proposed by Dimitrov et al.[76] DELs were greatest at 12 m/s as it reached the maximum thrust force hence the largest platform surge and pitch motions. The blade root out-of-plane moment damages can then be related to the platform pitch motions and corresponding acceleration and gravity loads and also the large gravity and inertial loads on the blade.

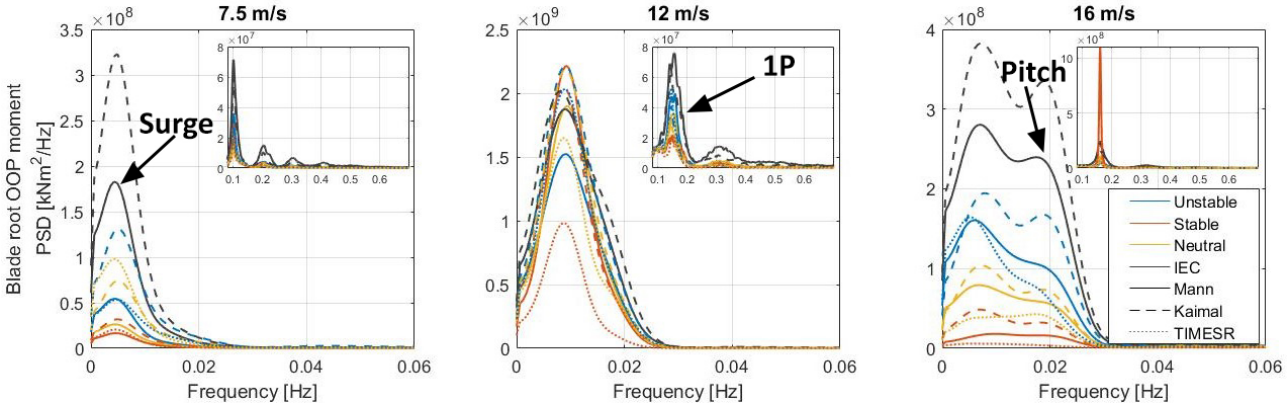


Figure VI.19: *Blade root out-of-plane moment spectra at each wind speed*

## VI.3.2 Influence of atmospheric stability

This subsection discuss the influence of atmospheric stability on the tower top yaw moment, $M_{topZ}$, the tower base fore-aft bending moment, $M_{baseY}$, the fairlead tension of the mooring line 2, $F_{fairten2}$, and the blade root out-of-plane bending moment, $M_{oop}$. Figure VI.20 shows the percent difference between stability conditions normalized with neutral conditions using Equation VI.1 for the spar floater as a function of mean wind speed at the hub. Each point represents the DEL from six 1-hour simulations and Mann and TIMESR are both shifted to the left and right, respectively, for readability purposes.

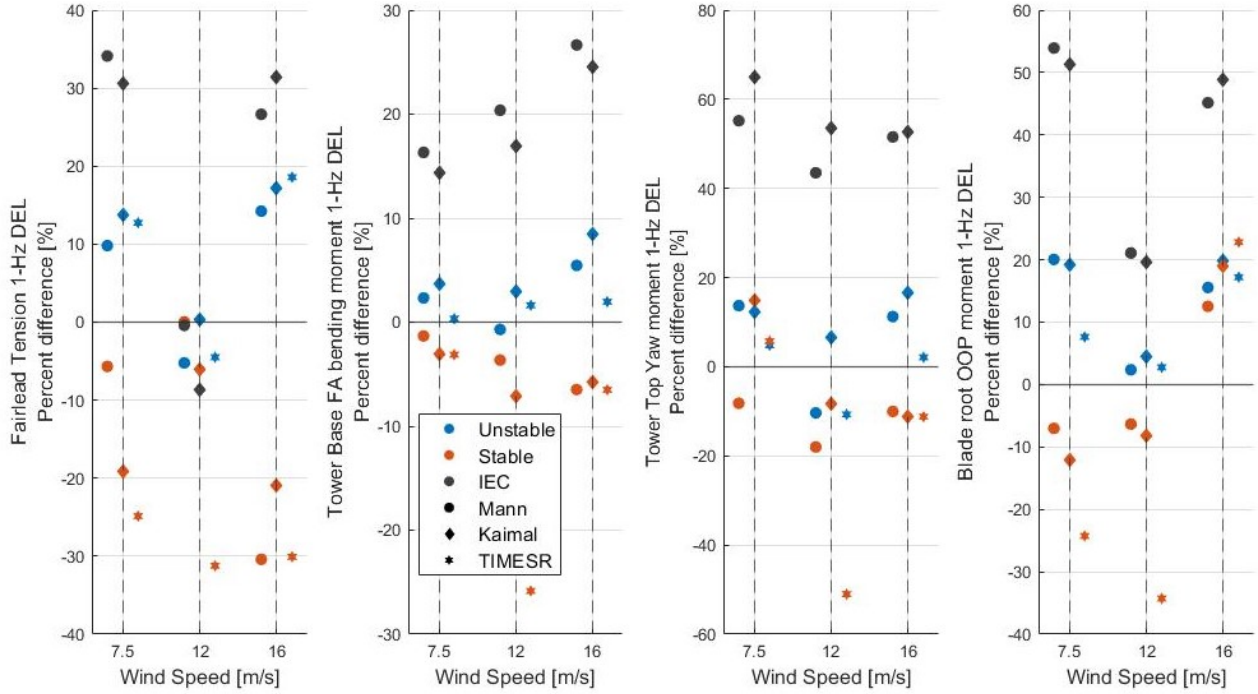


Figure VI.20: *Damage-equivalent loads percent difference between stability conditions and neutral conditions for all generation methods at each wind speed*

The impact of atmospheric stability on the fairlead tension damage was biggest for the highest wind speed scenario with differences up to 30% (using Mann model). The sensitivity to atmospheric stability was also high for the lowest wind speed scenario (around 15% of variation between stability conditions). Doubrawa et al.[21] found that loads on the mooring system were most sensitive to atmospheric stability in low winds. At 12 m/s, little sensitivity of the damage to atmospheric stability was found. Similar to the surge motion, high controller natural frequency can explain this behaviour.

According to Sathe et al.,[12] for a bottom-fixed turbine, the tower loads are mainly caused by variation in the thrust on the rotor which change with atmospheric stability. For a FWT, pitch motion is not negligible. Wind profile and turbulence vary with atmospheric stability and exert different force on different element of the wind turbine: the wind profile cause a moment at the blade root and at the hub while turbulence does so at the tower base. Sathé et al.[12] then showed that the larger the eddy size, the larger the moment at the tower base. In other words: the larger the vertical coherence, the larger the exerted force on the rotor. Unstable conditions should then lead to more damage than the other stability conditions. Figure VI.20 shows that under unstable conditions, damage were 1% to 9% higher than under neutral conditions. At 12 m/s under neutral conditions and using Mann model, damages were more important. Under stable conditions, damage were 8% to 1% lower. Only while using TIMESR, damages were 25% lower under stable conditions.
In the hypothesize that vertical coherence differences between stability conditions are similar for lateral coherence, Figure VI.8 shows small differences in coherence between stability conditions which can

explain the small differences in tower base fore-aft bending moment damage equivalent loads. The higher damage at 12 m/s under neutral conditions can be explained by the fact that surge motion was more important in this case. It should be noted that, because of the non-isotropic nature of the Mann turbulence model, the coherence between two points on a radial line (typically the rotor border) is different depending on the azimuthal position.[76] Nonetheless, atmospheric stability influences vertical and lateral coherence similarly.

Atmospheric stability influence on tower top yaw moment DELs depended on the wind speed and the wind model. Kaimal predicted higher damages under unstable conditions at 12 m/s and 16 m/s while Mann predicted so at 7.5 m/s and 16 m/s. At 12 m/s, TIMESR and Mann predicted higher damage under neutral stability conditions and Kaimal predicted higher damage at 7.5 m/s under stable conditions. These differences were found to be due to differences in 3P/tower frequency loadings, as seen in Figure VI.18.

Sathe et al.[12] hypothesized that the dynamic moments at the blade root section were mainly influenced by the wind profile and turbulence. Under stable condition, a greater shear would lead to a larger force on the blades. Sathe et al.[12] then observed that atmospheric stability had small influence on the blade root out-of-plane moment DELs. It was also our case at 12 m/s, as shown in Figure VI.20. The larger differences at 7.5 m/s and 16 m/s wind speeds can be explained by differences in wind profiles and turbulence intensities at these wind speeds. A large shear at 16 m/s wind speed under stable condition (see Figure IV.4) can explain the high damage, although the blade root out-of-plane moment DEL were still higher under unstable conditions. This shows a high influence of turbulence (turbulence intensity and coherent structures) on the blade root DELs. Doubrawa et al.[21] found that loads on blade root were most sensitive to atmospheric stability in high winds. Although they also found that neutral conditions resulted in the lowest damage at this wind speed, loads on blade root were found to be most sensitive to atmospheric stability in low wind speeds in our case.

Figure VI.20 shows that, under IEC conditions, DEL were always larger (up to 54%) than those obtained by using fitted models, which shows that the IEC wind models are quite conservative but also that turbulence intensity has a high influence on the DEL. Whether turbulence intensity or coherence has a greater influence on the loads can be studied in further work.

### VI.3.3 Design standard models or stability conditions

Similarly to Section VI.2.3, Figure VI.21 shows the percent difference between Kaimal and Mann models for all stability conditions and wind speeds.

Fairlead tension damage was more influenced by the choice of wind model at 7.5 m/s. Indeed, using Kaimal under stable conditions led to the same damage as using Mann in neutral conditions and the percent difference between the two models under unstable conditions was 27%. At 12 m/s, changing from neutral to unstable conditions led to a bigger difference in damage than changing the wind model. Opposite to 7.5 m/s, change in atmospheric stability at 16 m/s had more influence on the fairlead tension damage than changing the wind model.

Since the tower base fore-aft bending moment was not highly influenced by the wind model or the atmospheric stability at 7.5 and 12 m/s wind speeds, it is difficult to conclude. The influence of atmospheric stability was greater, although small, at 16 m/s.

Choice of the wind model had the greatest influence on the tower top yaw moment damage. Higher difference in coherence between the models than between stability conditions could explain this behaviour.

The blade root out-of-plane moment was not sensitive to the choice of turbulent wind model but was

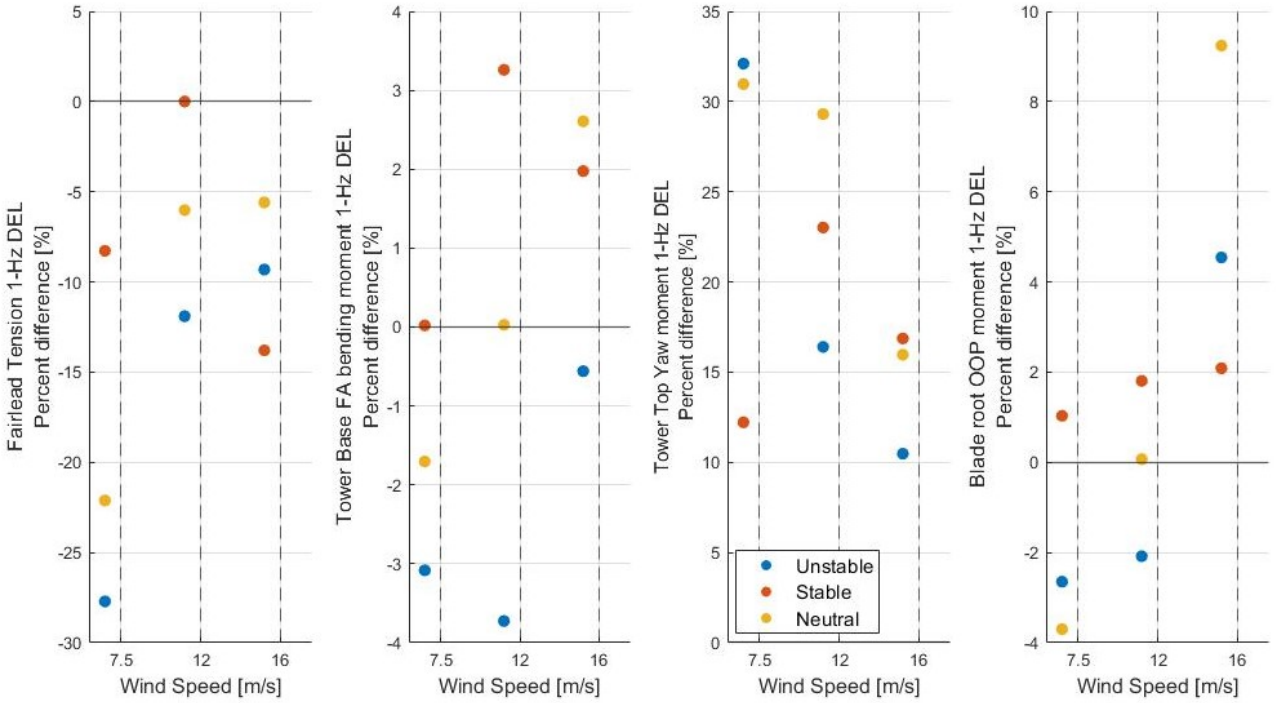


Figure VI.21: *Damage-equivalent loads percent difference between Kaimal and Mann for all stability conditions at each wind speed*

slightly more influenced by the atmospheric stability. Similarly, since Kaimal and Mann had the same turbulence intensity, differences in the blade root out-of-plane moment damage could be explained by the differences in coherence or wind profile which are non-negligible between atmospheric conditions.

# VI.4 Mann parameters sensitivity analysis

This section contains a study of the influence of each Mann model parameters: $\alpha\epsilon^{2/3}$, $L$ and $\Gamma$ (see Section V.2.4). Dimitrov et al.[76] assessed the individual effects of each Mann turbulence parameters on fatigue and ultimate loads using the NREL 5 MW turbine and the DTU 10 MW reference turbines on fixed platforms. It was found that $L$ and $\Gamma$ had a significant influence on loads, explained by the change in coherence: Increasing $L$ or $\Gamma$ led to less fatigue damage. All the following percentages value given are understand to be the percent difference between the varying cases and the base case.
The analysis in this study was done at 16 m/s mean wind speed and a target standard deviation was then achieved in each situation and was equal to the one of the base case.

## VI.4.1 Influence of $\alpha\epsilon^{2/3}$

As highlighted by Dimitrov et al.,[76] changing $\alpha\epsilon^{2/3}$ is equivalent to scaling the variance of the wind spectrum. Figure VI.22 shows that changing $\alpha\epsilon^{2/3}$ had no influence on the standard deviation that has been scaled. This negligible impact in turbulence intensity translated in the wind spectra in the longitudinal wind component as shown in Figure VI.23.

According to Equation II.17, the Mann model coherence is independent of $\alpha\epsilon^{2/3}$. Figure VI.24 showing the influence of $\alpha\epsilon^{2/3}$ on the lateral coherence of the longitudinal wind component between $(0, 0, 119)$ and $(0, 89.15, 119)$ confirms it. Results from simulations showed that coherence stayed similar at all frequency.

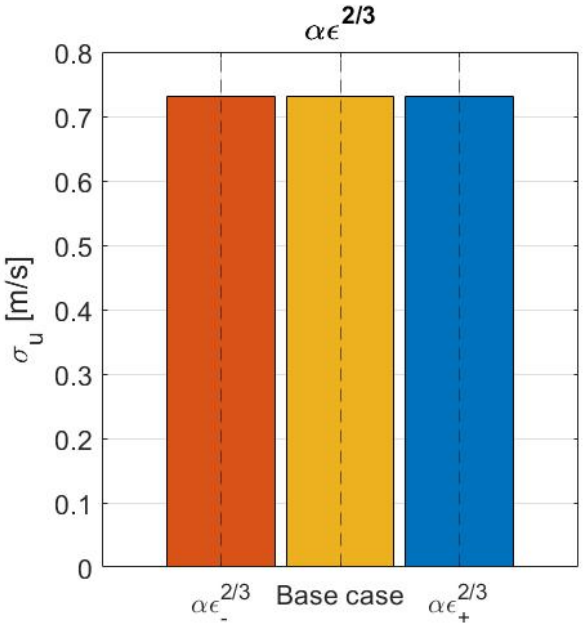


Figure VI.22: *Influence of $\alpha\epsilon^{2/3}$ on the longitudinal standard deviation*

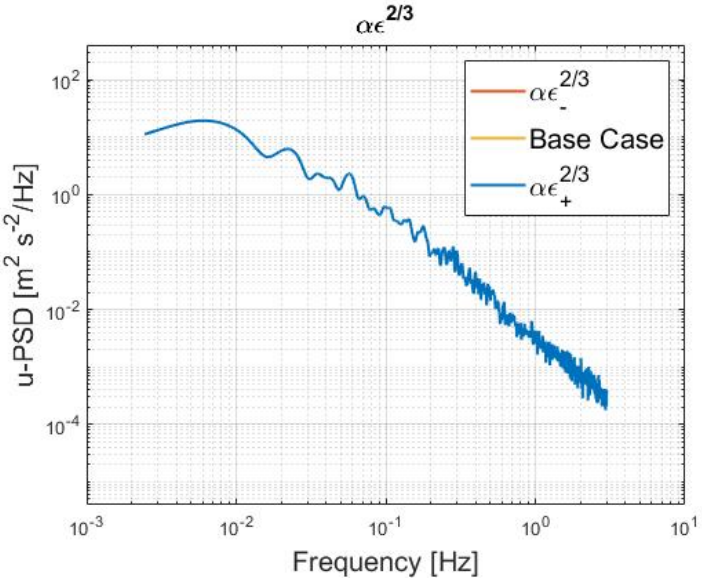


Figure VI.23: *Influence of $\alpha\epsilon^{2/3}$ on the power spectral density at hub centre*

Because the time series were scaled and resulted in the same turbulence intensity and lateral coherence, $\alpha\epsilon^{2/3}$ had no influence on pitch, surge and yaw motions standard deviations as shown in Figure VI.25. This was confirmed by Figure VI.26 that shows the influence of $\alpha\epsilon^{2/3}$ on the motions responses. Similarly, the sensitivity of the damage-equivalent loads to $\alpha\epsilon^{2/3}$ was negligible, as shown in Figure VI.27.

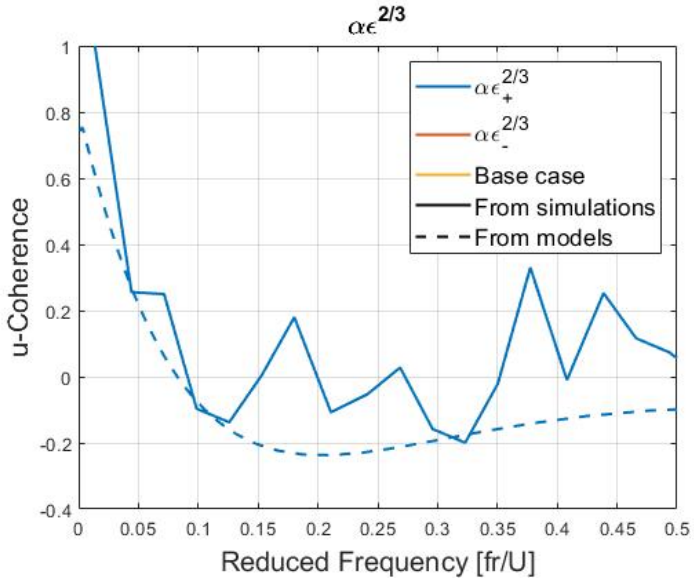


Figure VI.24: *Influence of $\alpha\epsilon^{2/3}$ on the lateral coherence of the longitudinal wind component between (0,0,119) and (0,89.15,119)*

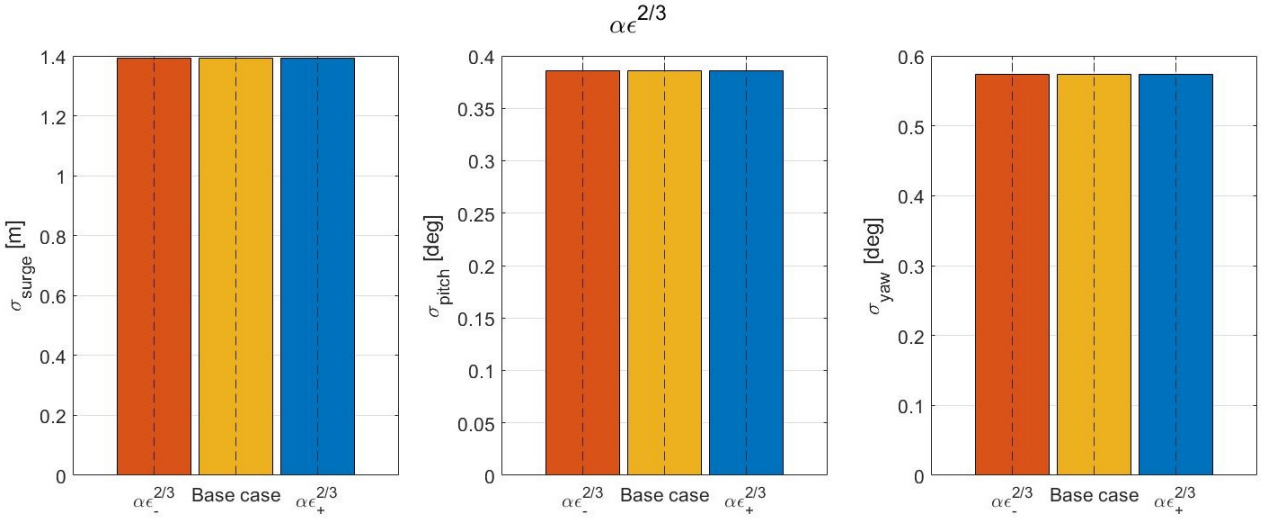


Figure VI.25: *Influence of $\alpha\epsilon^{2/3}$ on the platform pitch, surge and yaw motions*

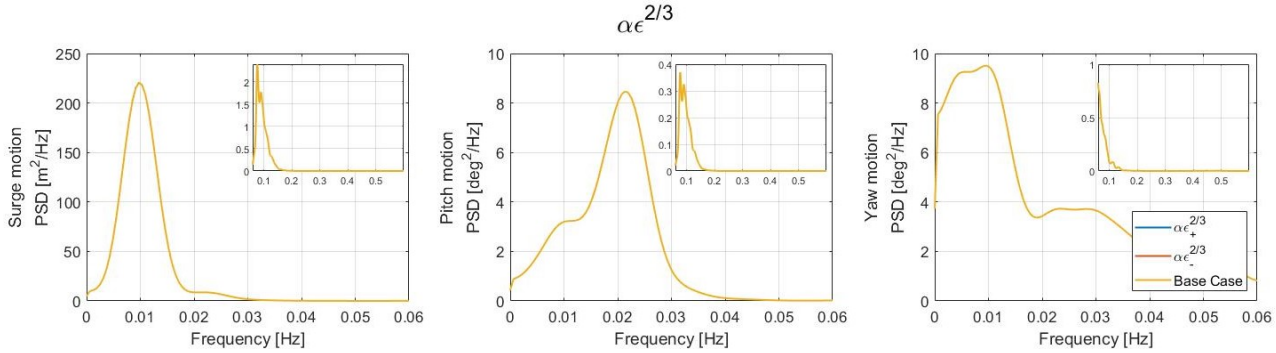


Figure VI.26: *Influence of $\alpha\epsilon^{2/3}$ on the platform motion responses*

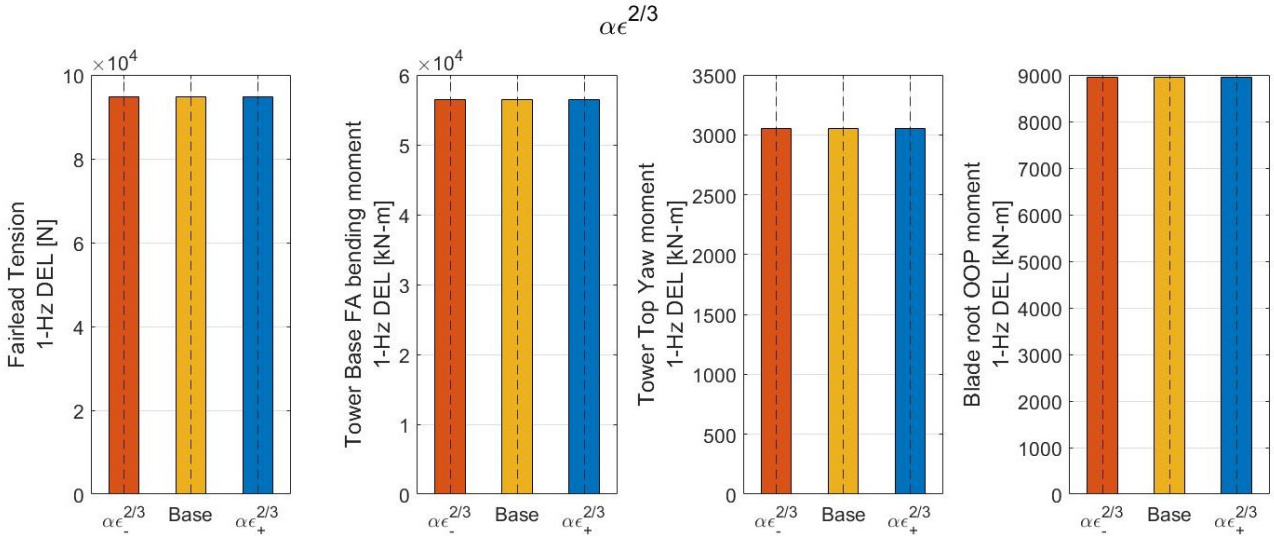


Figure VI.27: *Influence of $\alpha\epsilon^{2/3}$ on the damage-equivalent loads*

## VI.4.2 Influence of $L$

Figure VI.28 shows that variation of $L$ has an influence on the longitudinal wind component standard deviation. The variation in the parameter value (66.8%) resulted in a 5.7% lower standard deviation in the lower $L$ case, and a 1% higher value in the higher $L$ case. I am not sure why an equal variation of the parameter gave different standard deviation variation. Furthermore, I am not sure why the standard deviations are different even though a scaling has been performed. Investigating how the DTU Mann generator generates the time series could maybe give an answer to these questions.

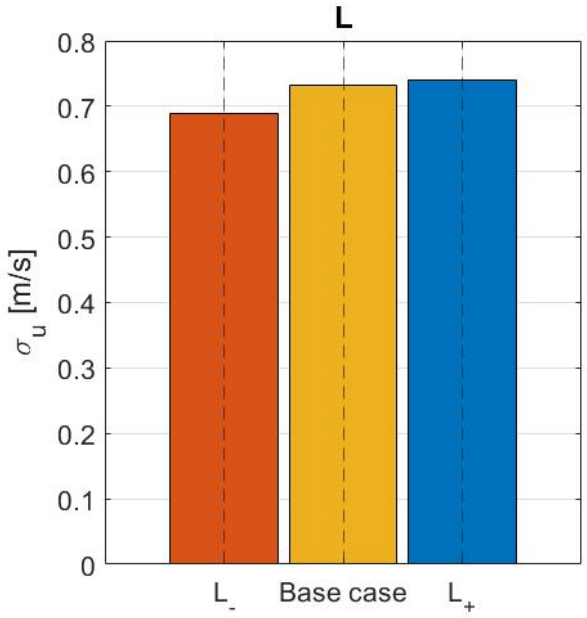


Figure VI.28: *Influence of $L$ on the longitudinal standard deviation*

As expected, this variation in turbulence intensity translated in the low frequency range of the wind spectra in the longitudinal wind component as shown in Figure VI.29. This result was consistent with the theory:[47] higher values of $L$ imply higher energy in the low frequency range of the wind spectra.

Figure VI.30 shows the influence of the length scale parameter on the lateral coherence between the hub

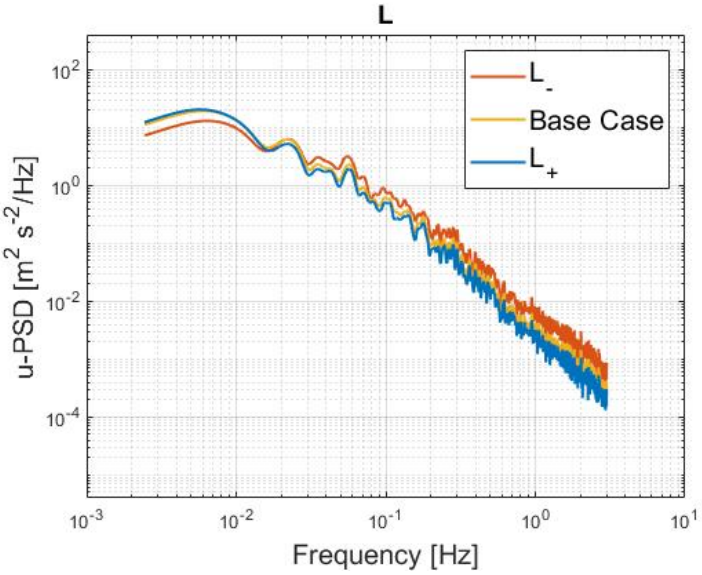


Figure VI.29: *Influence of $L$ on the power spectral density at hub centre*

centre and the tip of the rotor horizontally. As expected, coherence of the longitudinal wind component from the models showed an increase in coherence with increasing values of $L$. With larger eddy sizes, coherent structures covering the rotor are bigger hence increasing the coherence between the rotor centre and a point along one of the wind turbine blades.

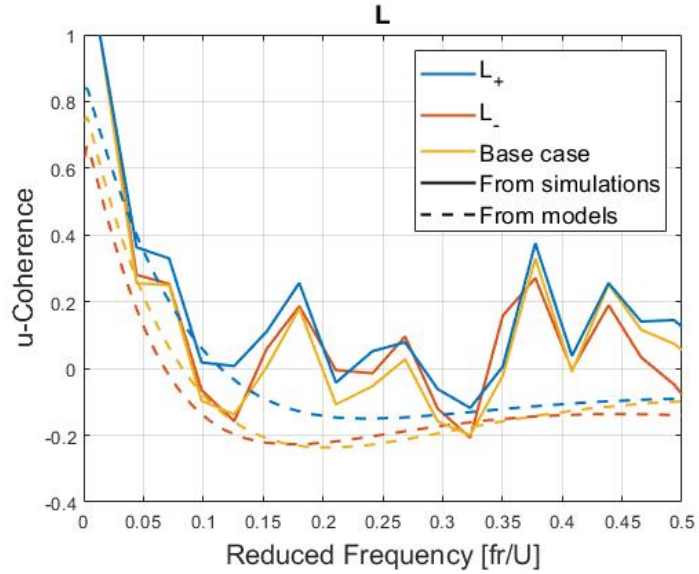


Figure VI.30: *Influence of $L$ on the lateral coherence of the longitudinal wind component between (0,0,119) and (0,89.15,119)*

Pitch, surge and yaw motions standard deviations are shown in Figure VI.31. Varying $L$ by 66% led to a 7.2% increase in surge motion and 17% decrease depending on the $L$ value. This result is similar to the one found with the fitted Mann model (see Figure VI.10): decreasing atmospheric stability led to an increase in surge motion. Whether turbulence intensity or coherence influenced surge motion is difficult to quantify in this situation because changing $L$ also changed the turbulence intensity. A 20% lower pitch motion was found with the lowest $L$ value while a 5.9% higher motion was found with the highest $L$ value. Yaw motion sensitivity to $L$ was non negligible in the lower $L$ case with a difference in motion of 19%. In the higher $L$ case, the difference was negligible.
These results were not what I was expecting. I thought increasing L would decrease the yaw motion but

the opposite happened. It also seems like decreasing L had more impact. An hypothesize could be that once the length scale reaches a certain value compared to the rotor size, its impact is less important.

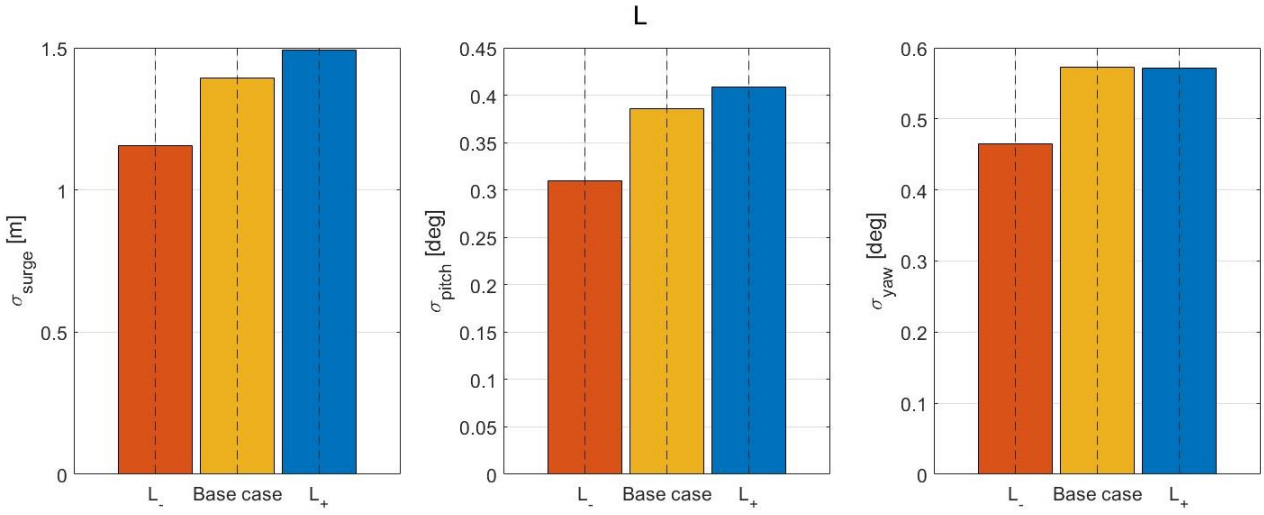


Figure VI.31: *Influence of $L$ on the platform pitch, surge and yaw motions*

Figure VI.32 shows the influence of $L$ on the motions responses. As expected, variations of $L$ did not influenced the wave-frequency responses and differences in motions standard deviation translated in differences in the spectrum: the greater the energy at the natural frequency, the greater the motion. The yaw response at higher frequency is explained by the yaw motion natural frequency value equal to 0.12 Hz. Similarly to the results presented in Figure VI.31, the difference in energy content at the motion natural frequency between the cases is the smallest when comparing the base case and the higher $L$ case.

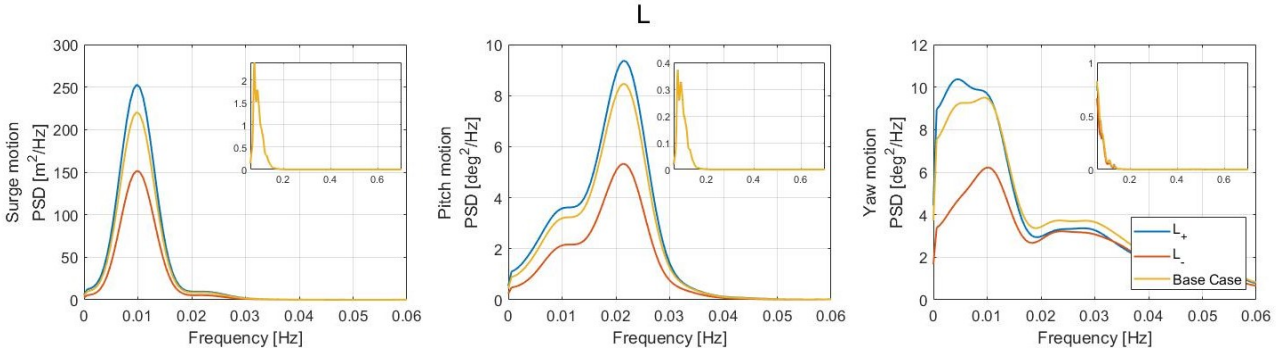


Figure VI.32: *Influence of $L$ on the platform motion responses*

Influence of the length scale parameter on different moments DELs is shown in Figure VI.33. Similarly to the surge motion, the fairlead tension damage varied with $L$ by up to 8%. This can be understood to be because of both the turbulence intensity and the coherence: a great $L$ value leads to a greater coherence over the rotor that results in large thrust. The tower base fore-aft bending moment DEL was not very sensitive to a $L$ parameter variation. Increasing and decreasing $L$ by 66% led to a 10% decrease and 12% increase in the tower top yaw moment DEL, respectively. Finally, the blade root out-of-plane moment DEL variation was negligible.

According to Dimitrov et al.[76] findings who studied the effect of $L$ and $\Gamma$ on 10 MW and 5 MW fixed-turbines, increasing $L$ results in reduced lifetime damage equivalent fatigue loads on the rotor. Our findings only agree with their results for the tower top yaw moment.

According to Dimitrov et al.,[76] an increase in $L$ implying a shift of the spectrum to the left could ex-

plain the reduction of loads. Indeed, this shift implies the frequencies of the order of rotor sampling frequency to have lower energy content.

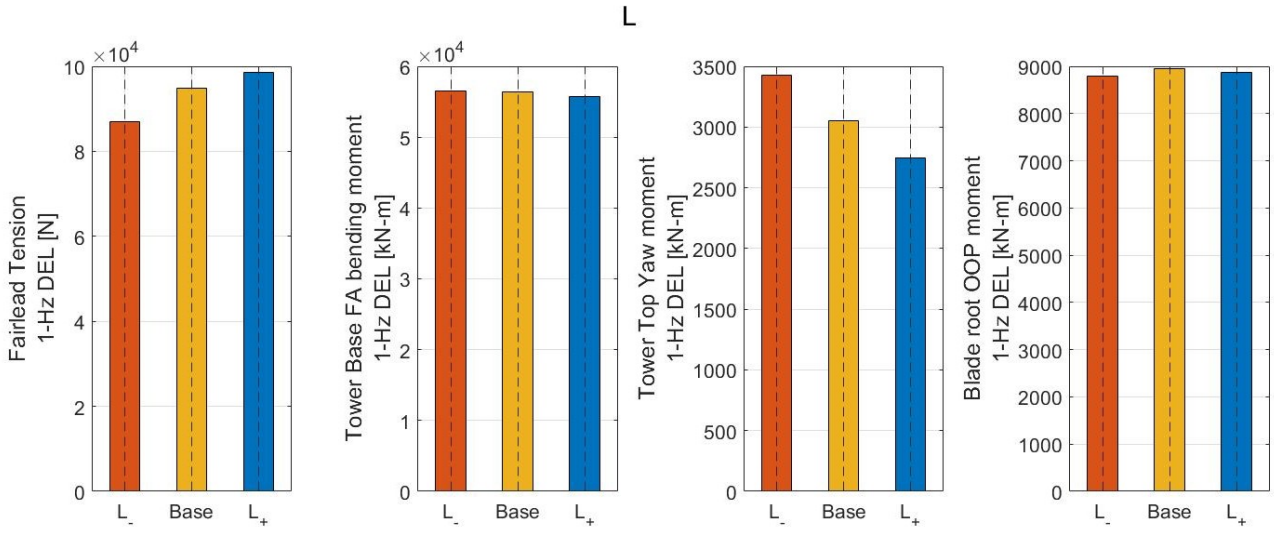


Figure VI.33: *Influence of L on the damage-equivalent loads*

## VI.4.3 Influence of $\Gamma$

Figure VI.34 shows the influence of $\Gamma$ on the longitudinal wind component standard deviation. $\Gamma$ parameter value varied by 29.5%. This resulted in a longitudinal wind speed standard deviation variation of 1% even though a scaling has been performed. Similarly to the influence of the length scale, I am not sure why there is a difference in standard deviation.

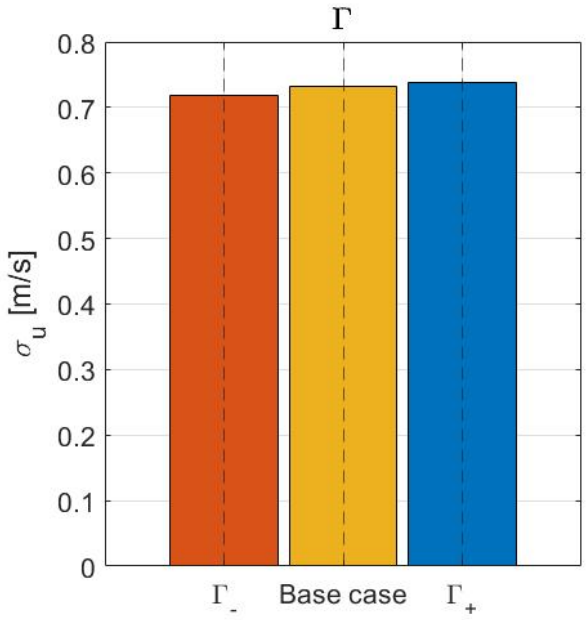


Figure VI.34: *Influence of* $\Gamma$ *on the longitudinal standard deviation*

The variation in turbulence intensity translated in the low frequency range of the wind spectra in the longitudinal wind component as shown in Figure VI.35 but a decrease of the energy content in the high frequency range was observed. It is more difficult to explain the impact of $\Gamma$ on turbulence intensity

but, according to Dimitrov et al.,[76] a shift in $\Gamma$ value changes the shear deformation of turbulent eddies and the ratio between the standard deviations of the wind speed in $u-$,$v-$ and $w-$directions.

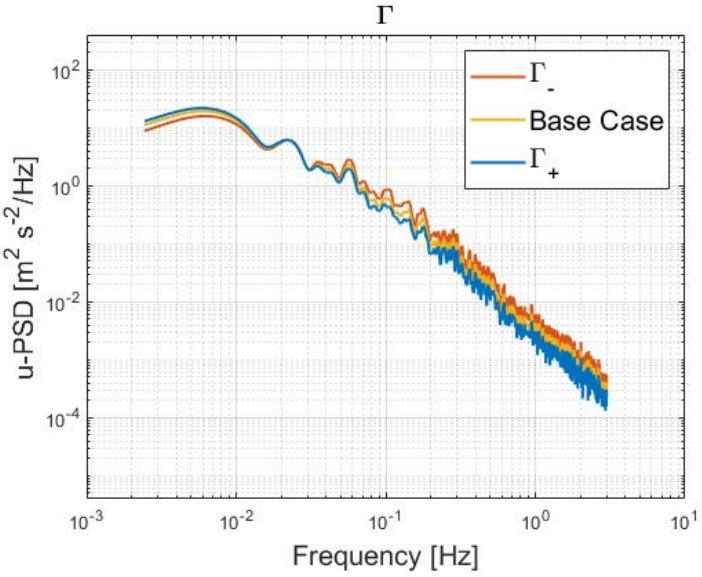


Figure VI.35: *Influence of* $\Gamma$ *on the power spectral density at hub centre*

Figure VI.36 shows the influence of the eddy lifetime parameter on the lateral coherence between the hub centre and the tip of the rotor horizontally. Coherence decreased with increasing $\Gamma$ as seen by Dimitrov et al.[76]

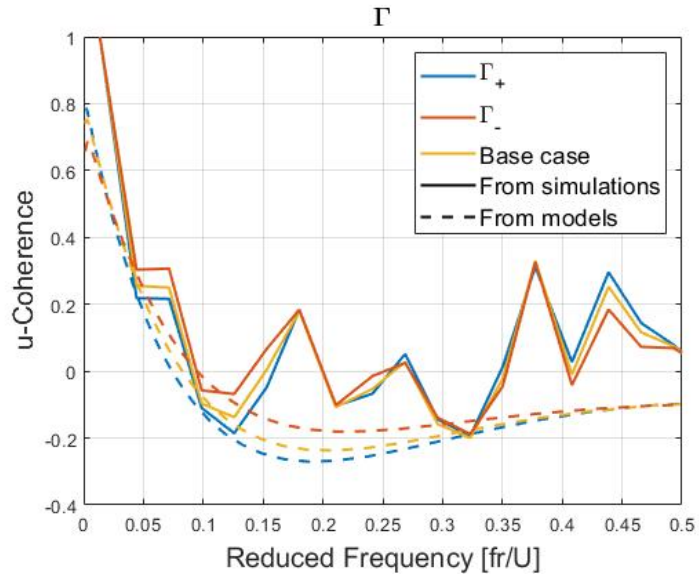


Figure VI.36: *Influence of* $\Gamma$ *on the lateral coherence of the longitudinal wind component between (0,0,119) and (0,89.15,119)*

Influence of $\Gamma$ on pitch, surge and yaw motions standard deviations is shown in Figure VI.37. A 15% $\Gamma$ variation resulted in a 2.4% increase in surge motion and 6.8% decrease. Pitch motion was not very sensitive to $\Gamma$ but still showed a higher pitch motion for the base case that could be considered as negligible ($\pm$1%). Yaw motion sensitivity to $\Gamma$ was similar to the surge motion ($\pm$4%). The yaw motion was in accordance with the change in lateral coherence: less coherence led to greater yaw motion. The change in surge motion could be hypothesized to be greater influenced by turbulence intensity than by lateral coherence. Concerning the pitch motion, I am not sure why the base case led to the greatest

motion; maybe increasing the number of simulations (i.e. number of seeds) would show that Γ has a negligible impact on the pitch motion.

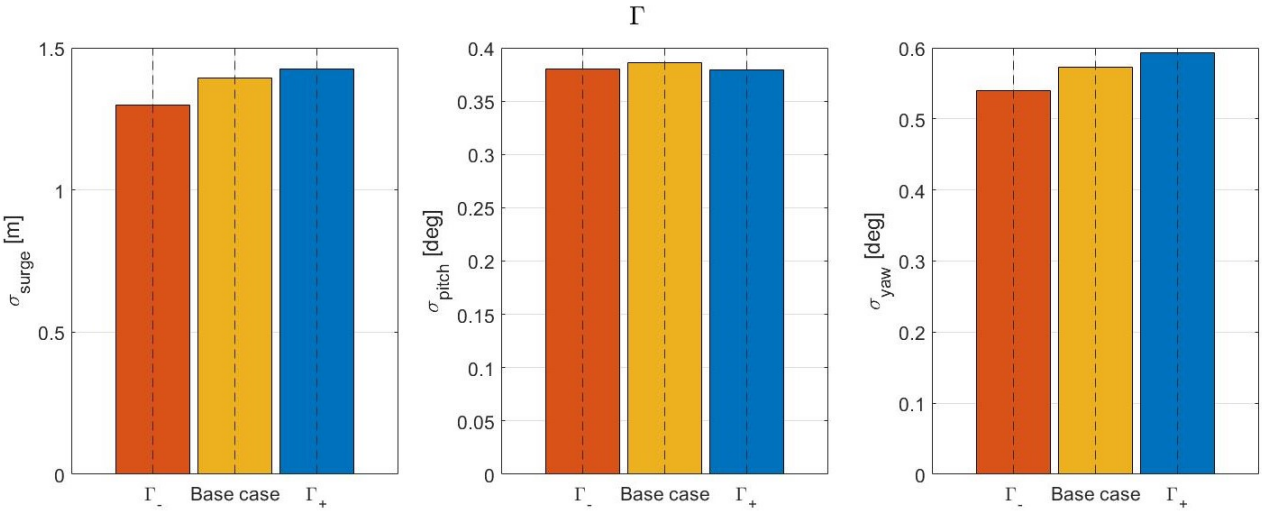


Figure VI.37: *Influence of* Γ *on the platform pitch, surge and yaw motions*

Similarly to the two other parameters, Γ influenced the low frequency range of the motion spectra and did not influenced the wave-frequency responses (see Figure VI.38) and the variation in standard deviation translated at the motions natural frequencies.

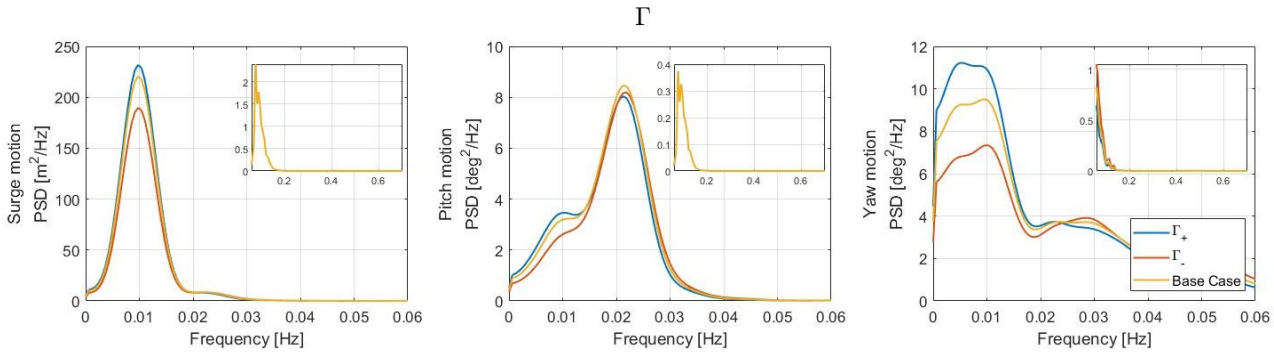


Figure VI.38: *Influence of* Γ *on the platform motion responses*

Figure VI.39 shows the influence of Γ on the DELs. The fairlead tension damage varied with Γ by 3%. Γ smallest influence was on the tower base fore-aft bending moment DEL and the blade root out-of-plane moment DEL with a 0.5% variation. The tower top yaw moment is impacted similarly to the yaw motion: varying Γ by 29% led to a 2% change in tower top yaw moment DEL.
Consistently with Dimitrov et al.,[76] the influence of Γ is lower than that of $L$. The impact of Γ was suggested to be due to "the changes in the $v-$,$w-$components of turbulence caused by the [variation of] Γ" which implies a change in shear deformation of the eddies: greater shear may induce greater rotor loads.

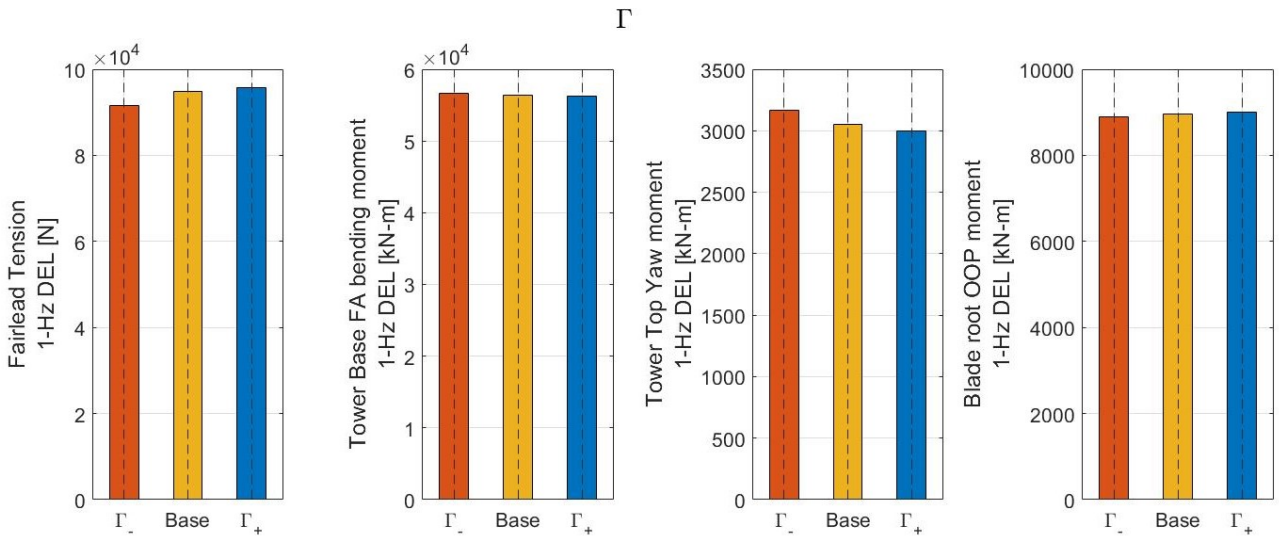


Figure VI.39: *Influence of* Γ *on the damage-equivalent loads*

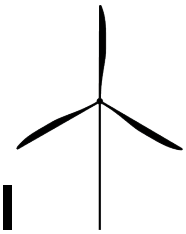

# CHAPTER VII

# Conclusions and recommendations

This work aimed at contributing to better understand how atmospheric stability and the choice of the wind model influenced the dynamics of a spar-type floating wind turbine. Three turbulent generation models were used for the simulation: the IEC Kaimal and coherence model and the Mann model, both recommended by the standards,[2] and TIMESR which generate turbulence using wind time series at different heights. Measurements from the FINO-1 research platform were processed and allowed for a fitting of Mann model parameters, IEC Kaimal coherence model and the Davenport coherence model to generate turbulent wind fields that matched specific atmospheric conditions (as close as possible to what can be found offshore). These atmospheric conditions were sorted following Golder classification:[36] unstable, neutral and stable based on the gradient Richardson number. A forth atmospheric condition was considered: the one recommended by the IEC guidelines[2] which aim at modelling neutral conditions. Since the Mann parameters or IEC Kaimal coherence model parameters recommended by the design standard[2] were different from the fitted parameters, the atmospheric condition IEC was considered as an additional condition. Finally, the aero-hydro-servo-elastic tool OpenFAST[4] was used to compute 1-hour simulations with different atmospheric conditions.
Based on this work results, conclusions are drawn in Section VII.1 and recommendations for future research are provided in Section VII.2.

## VII.1 Conclusions

Conclusions answer the questions described in Chapter I.

**Q1: "To what extent are wind fields influenced by wind models and atmospheric stability?"**
Since a scaling of the turbulence intensity to the measurements was performed for only simulations using the Mann model, small differences in the three wind components standard deviations appeared between the models. Generally, TIMESR resulted in the lowest standard deviations while Kaimal and Mann models gave similar longitudinal standard deviations for all three atmospheric conditions. The three models always resulted in lower standard deviation than the target value from measurements; it was understand to be due to the averaging of the standard deviation among the hub centre neighbouring grid points. The impact of atmospheric stability on

turbulence intensity was significant and was greater for higher wind speeds. Generally, standard deviation in the three wind components was the lowest under stable conditions and the highest under IEC conditions.

Differences in spectra when using Mann and Kaimal were negligible in the low-frequency range, which is more relevant for floating wind turbines, but Kaimal model resulted in higher energy content at higher frequency (above 1 Hz). TIMESR generally provided the lowest energy content at low-frequency which translated in lowest wind speed standard deviations. Concerning the influence of atmospheric stability: the energy content at all frequencies increased with decreasing atmospheric stability.

Coherence was also investigated. First the vertical coherence between a point at hub centre and a point 20 meters below was studied in order to compare the coherence given by the models, the simulations and the measurements. It was found that Kaimal model generally resulted in higher coherence for all atmospheric conditions. Whether TIMESR or Mann models provided less coherence depended on the atmospheric stability and the wind speed. It was also found that TIMESR coherence for the longitudinal component was the closest to measurements. Concerning the lateral coherence between the hub centre and a point on a radial line at 89.15 meters (blade length), Kaimal consistently provided the most coherence while Mann the lowest. The impact of atmospheric condition was not negligible: coherence increased with decreasing stability, as found by Chougule.[47]

**Q2: "To what extent are FWT dynamics influenced by wind models?"**
Consistently with Bachynski and Eliassen,[23] it was found that the pitch and surge motions were greater while using Kaimal model. Mann and Kaimal similarity with TIMESR results depended on the wind speed: Kaimal gave closer results for the lowest wind speed and the opposite was true for the highest wind speed. Concerning the yaw motion, Mann resulted in the greatest motions and Kaimal gave closer results to TIMESR simulations. These differences in motions were explained by the differences in coherence.

The impact of the wind model on damage equivalent loads was significant with ranges of variation of more than 30% depending on the moment considered: the tower top yaw moment being the most sensitive to the change in wind model. Differences were related to the differences in coherence.

**Q3: "To what extent are FWT dynamics influenced by atmospheric stability?"**
Generally, global motions of the platform were more important under IEC conditions, then unstable conditions, and were the lowest under stable conditions. Ranges of variation were from 1% to nearly 90%. Even though differences in motions between the wind model were explained by the differences in coherence, it was observed that turbulence intensity had a great impact on the motion. While coherence increased with decreasing stability, unstable conditions still led to the greatest yaw motions.

The impact of atmospheric stability on the loads was the greatest for the fairlead tension with 30% less damage under stable condition than under neutral condition at the highest mean wind speed. The lowest impact was on the tower base fore-aft bending moment. Similarly to the yaw motion, damage from the tower top yaw moment were understood to be greatly influenced by turbulence intensity.

**Q4: "How does lateral coherence influence FWT loads?"**
Lateral coherence had a non negligible influence on the floating wind turbine dynamics and it was mostly seen when turbulence intensity was identical between models. Differences in coherence resulted in different motion and load results. More uniform structures over the rotor for the Kaimal model resulted in large thrust variation leading to greatest surge and pitch motions and

small out-of-plane forcing resulted in small yaw moment. Concerning the loads, high coherence resulted in large moment at the tower base and low yaw moment.
While these are important findings, a lifetime fatigue study should be carried out to check if these conclusions are still valid beyond the short-term fatigue damage estimates.

**Q5: "Is changing the atmospheric stability more influential than the choice the wind model?"**
Is is difficult to answer this question as it depended on the wind speed, the global motions or the load considered. What can be concluded is that both IEC recommended wind models (Mann and Kaimal) need to take into account the different atmospheric stability conditions and that more qualitative measurements are needed to fit the models to offshore conditions.
The IEC guidelines[2] also provide a very conservative $90^{th}$ percentile turbulence intensity that resulted in an over-prediction of fatigue loading and global motions.

**Q6: "How does each Mann parameter influence the FWT dynamics?"**
Because of the turbulence intensity scaling, changing $\alpha\epsilon^{2/3}$ had no influence on the longitudinal wind speed standard deviation, the lateral coherence and any of the motions and loads. Increasing $L$ and $\Gamma$ resulted in an increase in longitudinal wind speed standard deviation even though a scaling was performed. On the wind spectrum, an increase in the two parameters resulted in greater energy content in the low-frequency range but less energy in the higher frequency range. Coherence was influenced by $L$ and $\Gamma$ variation: a greater $L$, which means larger eddies, gave higher coherence and the opposite was true for $\Gamma$. An increase in both parameters generally led to an increase in surge, pitch and yaw motions. The $L$ parameter had little influence on the tower base fore-aft bending moment and the blade root out-of-plane moment damage equivalent loads but led to an increase in fairlead tension DEL. The opposite was true for the tower top yaw moment DEL. Concerning $\Gamma$, same variation as with $L$ were observed but to a lesser extent.

This thesis showed that considering atmospheric stability was important when studying a floating wind turbine dynamics and that it should be considered when modeling it. No conclusions were drawn concerning the best wind model but high quality offshore measurements are needed to generate turbulent boxes that are closer to reality than what the IEC standard[2] recommend.

## VII.2 Recommendations

Based on this work, recommendations can be made for future research. Because of the limited amount of time, some aspect of the work were not further studied.

First, the wind profile used in this thesis is only valid in the surface layer and has one parameter that accounts for both atmospheric stability and roughness length. Gryning et al.[33] developed a wind profile that is valid for the entire boundary layer and that has a different formulation for the different stability conditions. Sathe et al.[12] showed that wind profile models can influence bottom-fixed wind turbine loads by up to 7%.

It was found that the fitted Mann parameters were not following trends from literature. It was explained by the fact that the Mann model is originally valid under neutral atmospheric conditions. Chougule[47] showed that additional parameters are required to quantify the buoyant-generated turbulence in the Mann model by taking into account the gradient Richardson number and the dissipation rate of temperature variance. Using his model could allow for turbulence generation closest to reality.

Because TIMESR simulations always resulted in the lowest standard deviation, a scaling of the turbulent boxes could be done to reach the target value and model more accurately the measurements. Instead of using expensive large eddy simulation, TIMESR generation method could be seen as an alternative if more measurements are available.

Furthermore, this study only considered a spar-type floater which correspond to a ballast stabilized platform. Studying the impact of atmospheric stability on other type of structures could be achieved in future work.

Simulations with fixed pitch or fixed generator torque at 12 m/s could be carried out to investigate the effect of the controller on the results at that wind speed.

High quality field wind measurements are needed to fit the IEC standard[2] models to offshore conditions. Measurements from floating wind turbine farms are also required for this fitting.

Finally, a sensitivity analysis on the impact of the rotor size to analyze the effect of larger wind turbines on the fatigue loads and platform motions could be done.

# APPENDIX A

## Spar decay tests

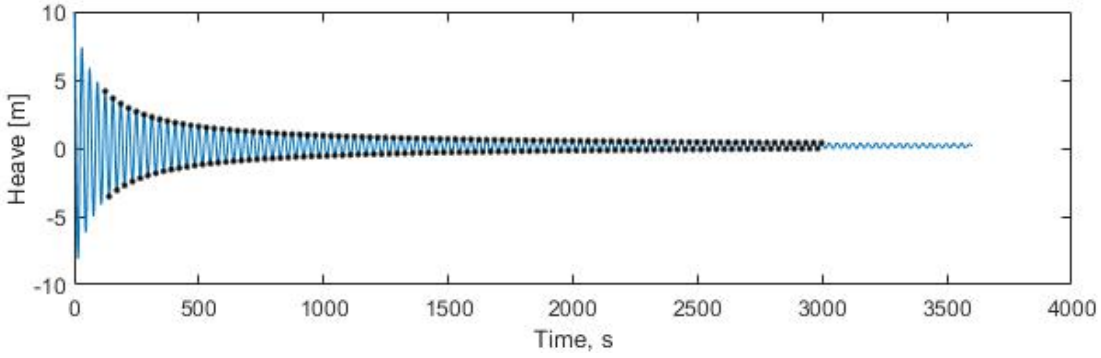


Figure A.1: *Heave spar decay test*

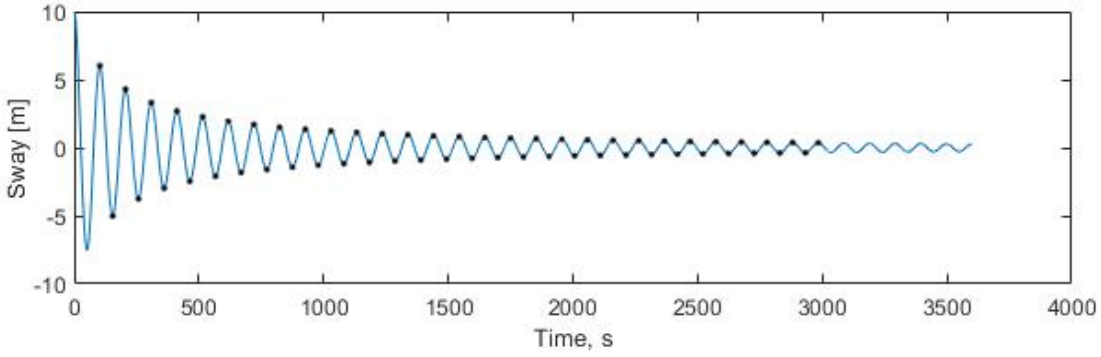


Figure A.2: *Sway spar decay test*

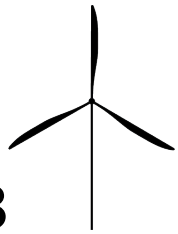

# APPENDIX B

## Wind spectra

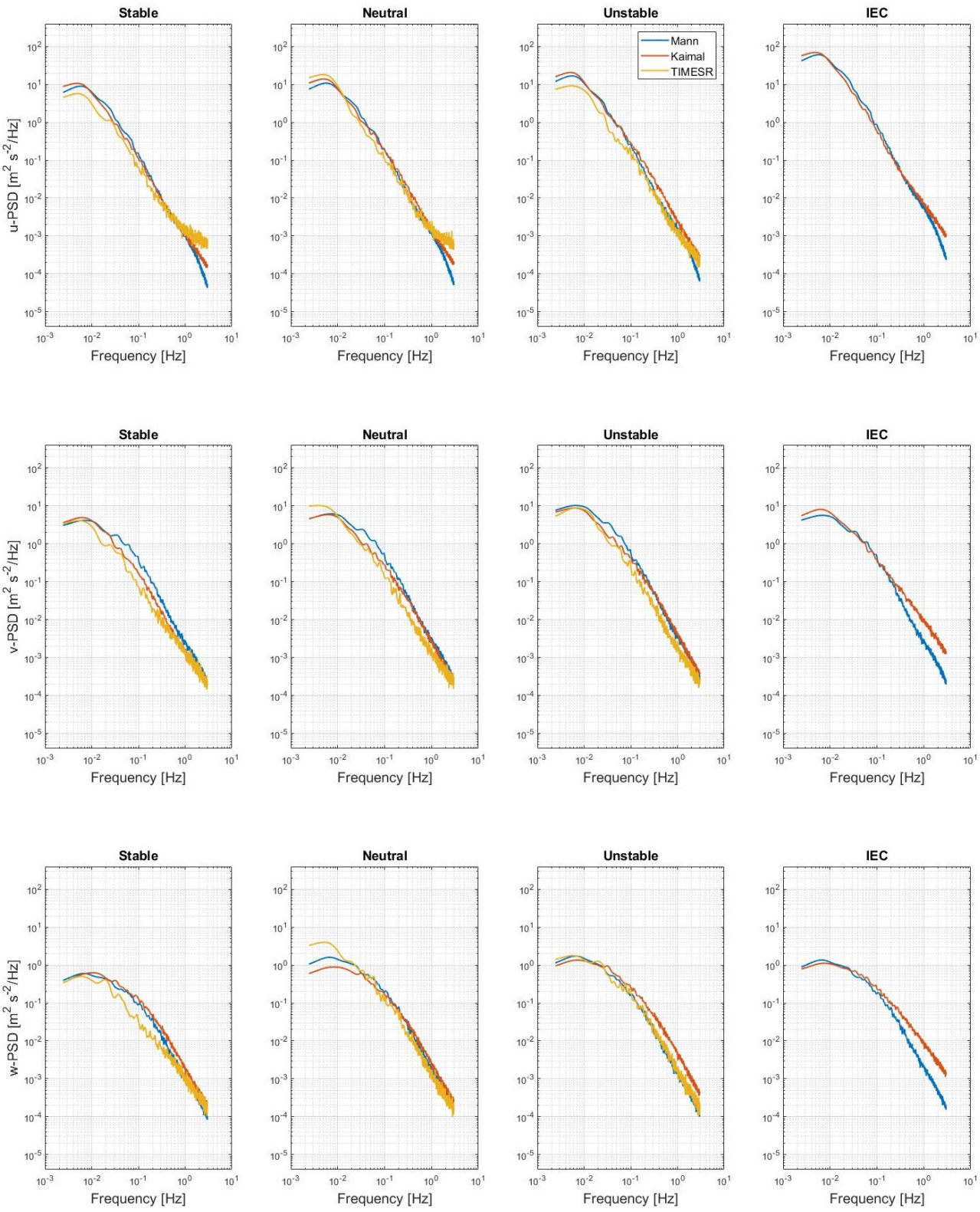


Figure B.1: *Power spectral density at hub centre at 7.5 m/s mean wind speed*

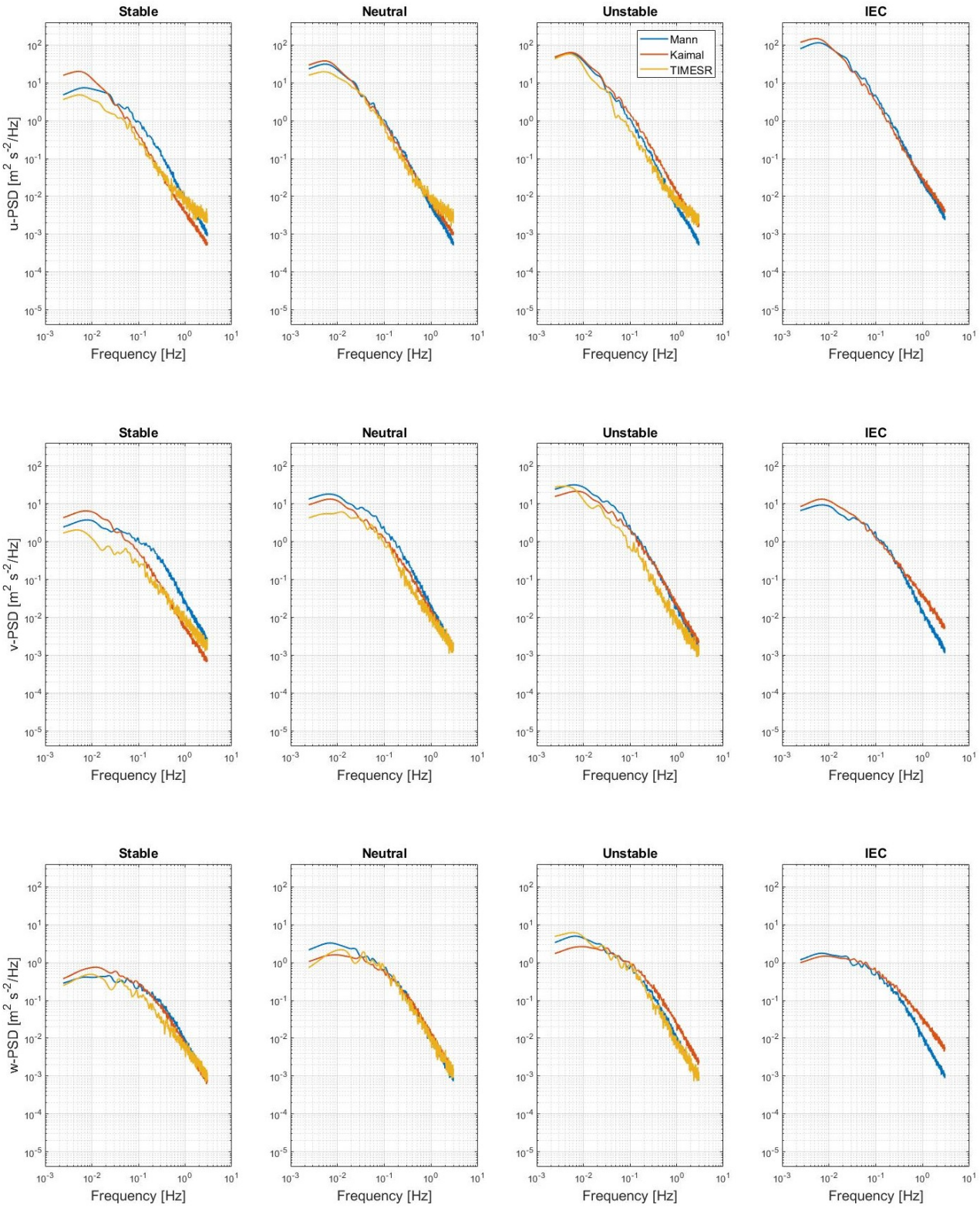


Figure B.2: *Power spectral density at hub centre at 7.5 m/s mean wind speed*

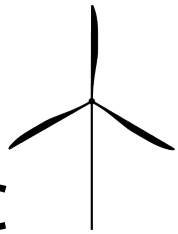

# APPENDIX C

## Coherence

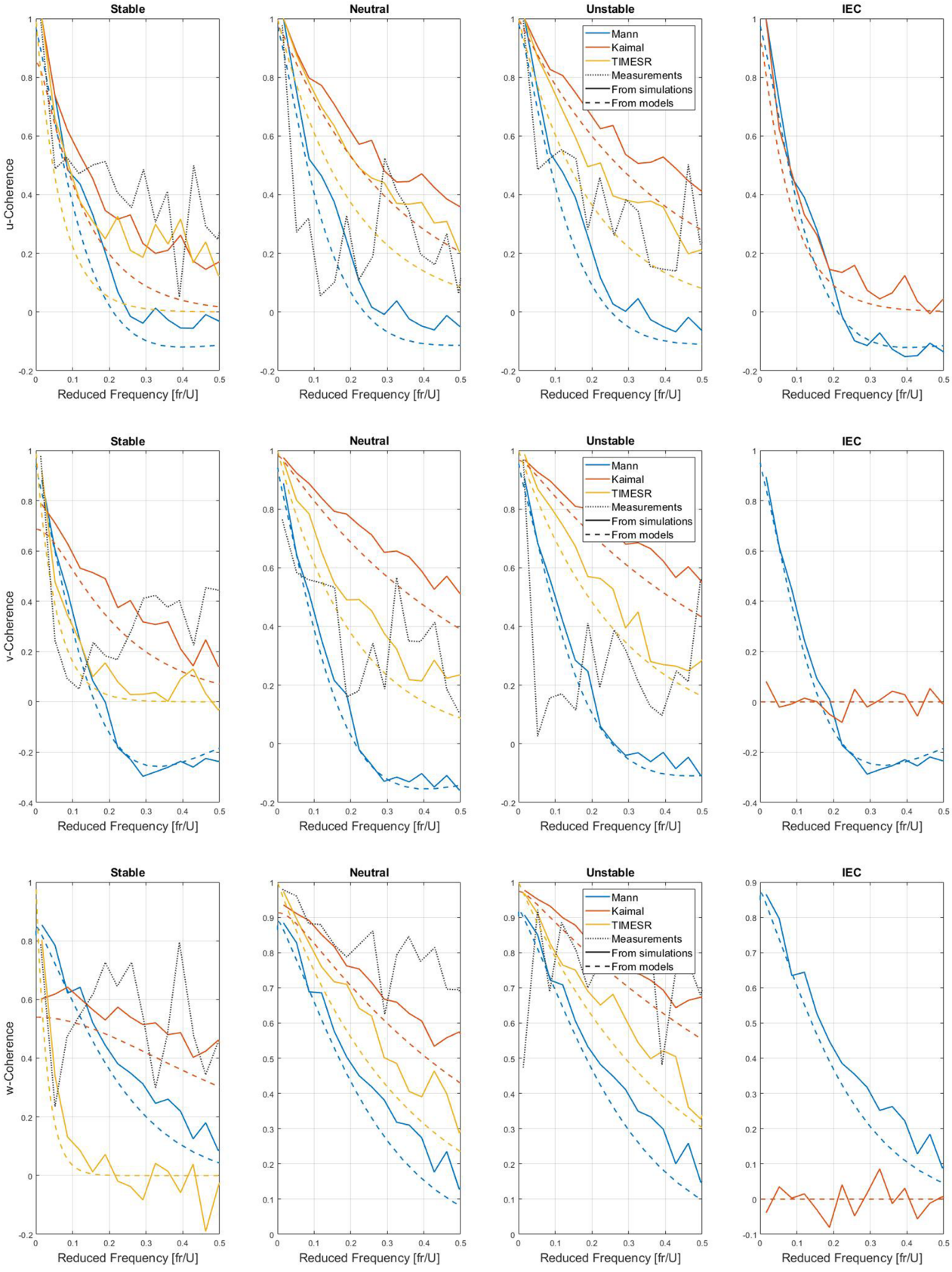


Figure C.1: *Coherence in three directions between hub height and 20 meters below the hub at 7.5 m/s as a function of reduced frequency*

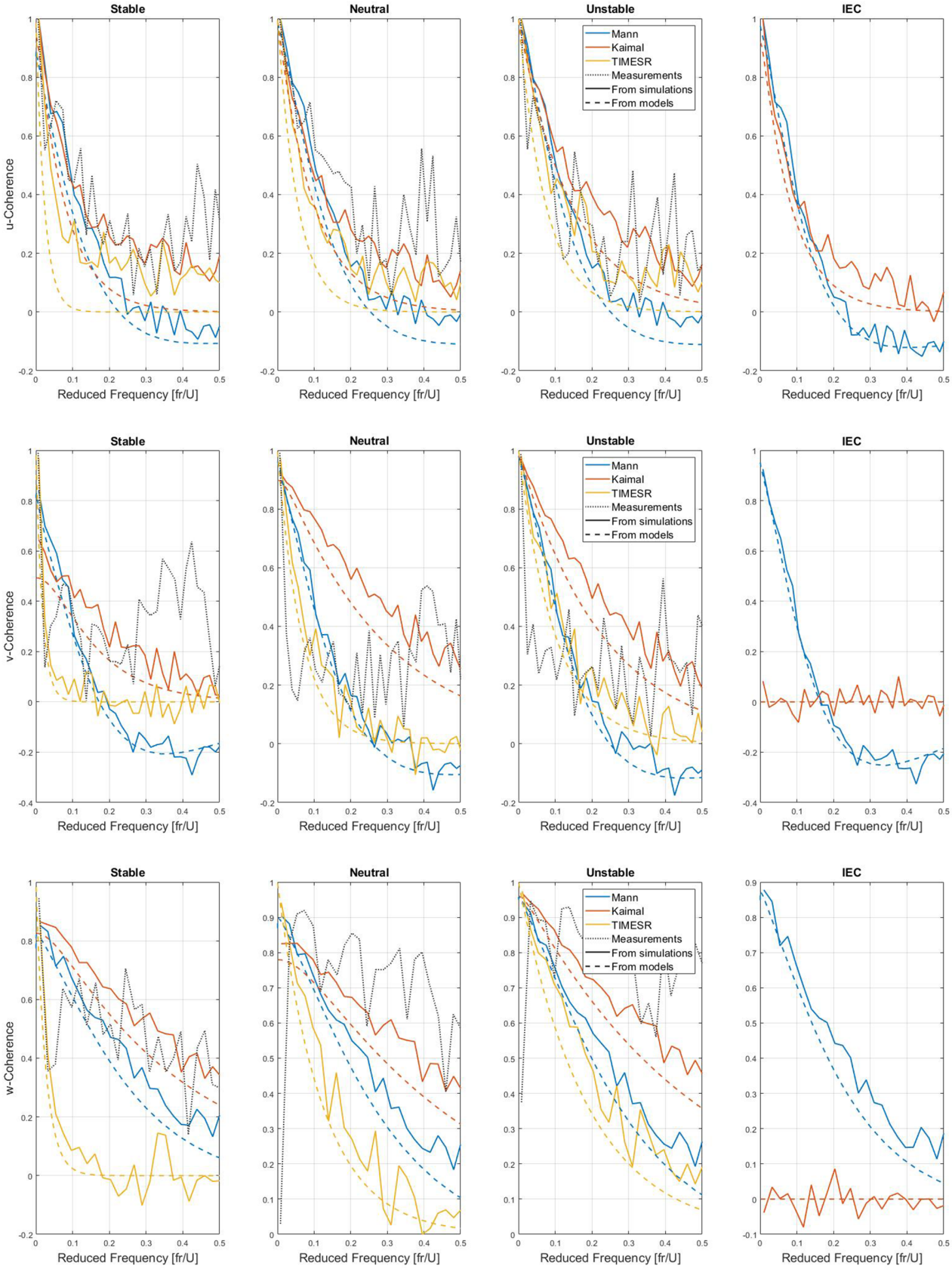


Figure C.2: *Coherence in three directions between hub height and 20 meters below the hub at 16 m/s as a function of reduced frequency*

# APPENDIX D

## Quad-coherence

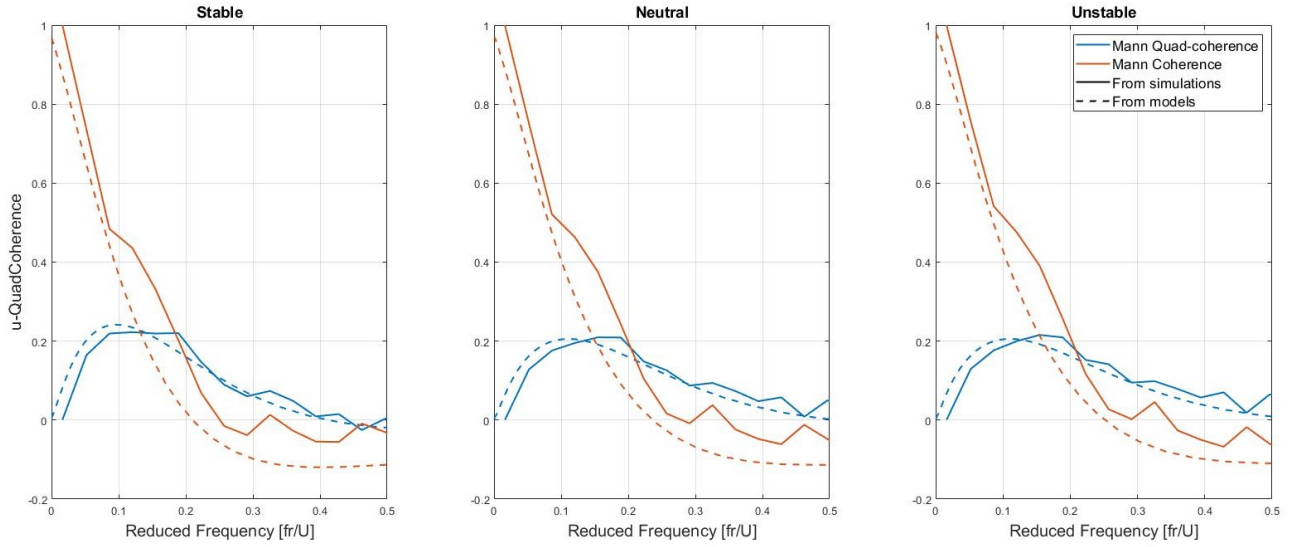


Figure D.1: *Quad-coherence in the longitudinal direction between hub height and 20 meters below the hub at 7.5 m/s as a function of reduced frequency*

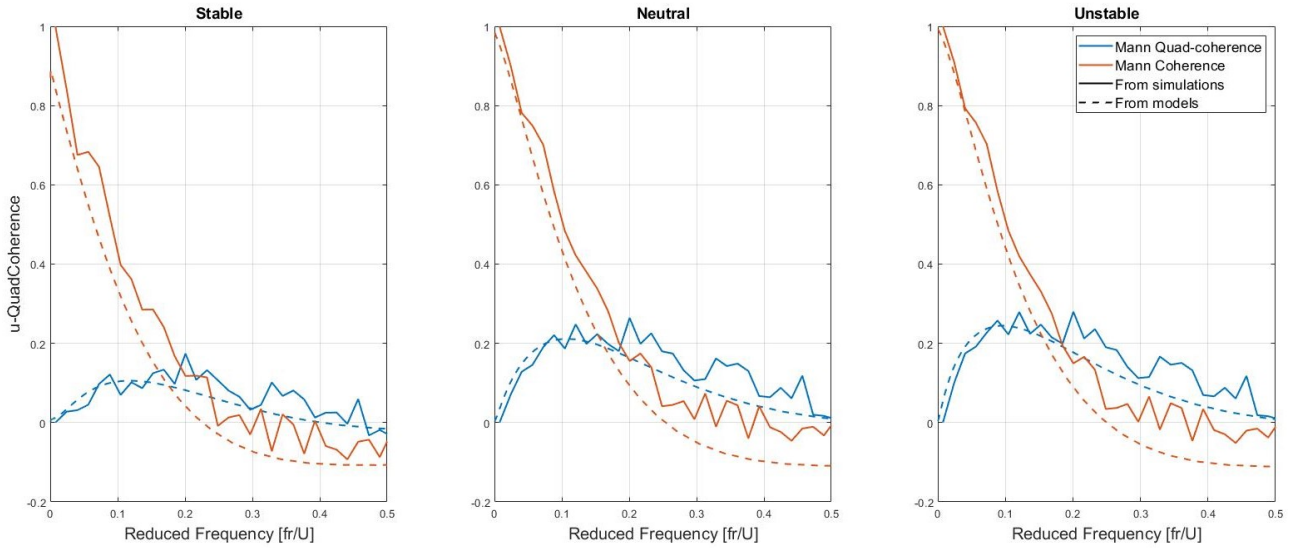


Figure D.2: *Quad-coherence in the longitudinal direction between hub height and 20 meters below the hub at 16 m/s as a function of reduced frequency*

# APPENDIX E

## Lateral coherence

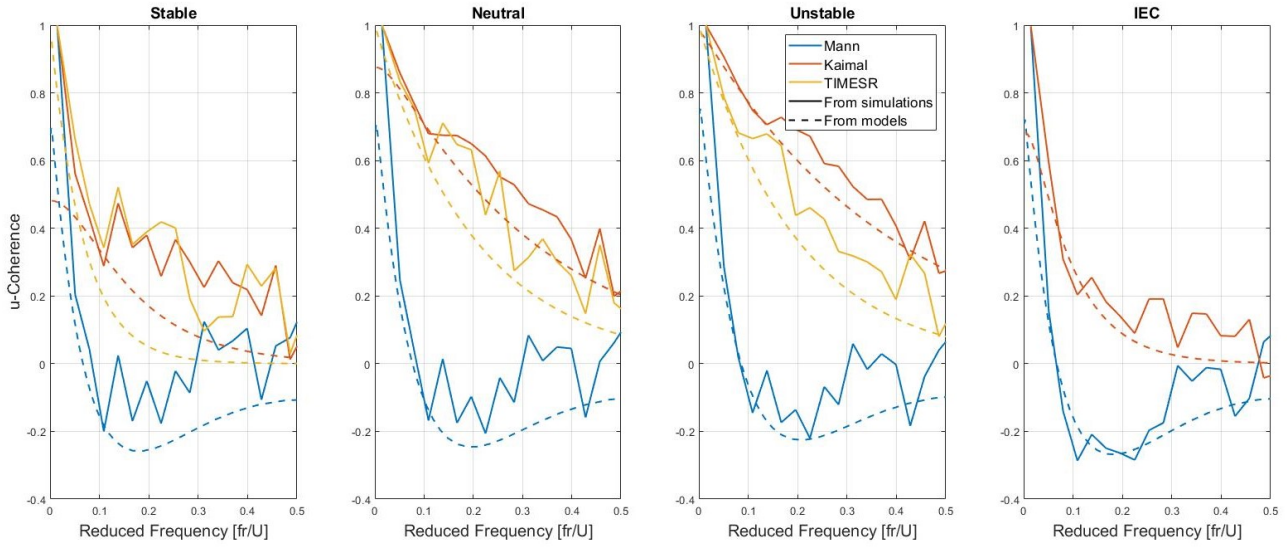


Figure E.1: *Lateral coherence in the longitudinal direction at 1/2 diameter separation distance at 7.5 m/s as a function of reduced frequency*

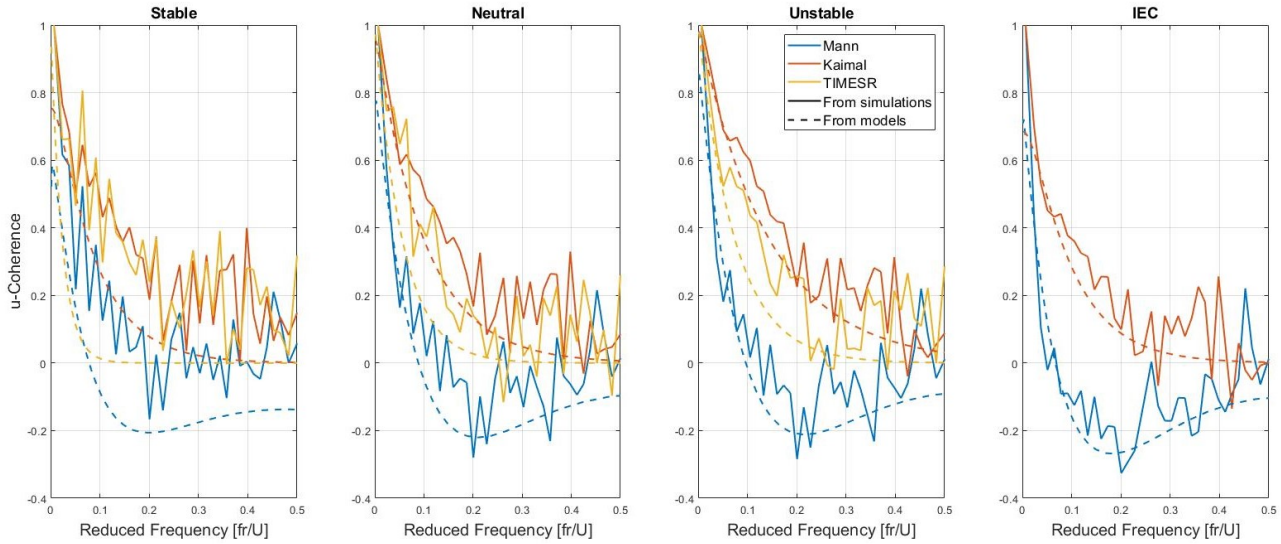


Figure E.2: *Lateral coherence in the longitudinal direction at 1/2 diameter separation distance at 16 m/s as a function of reduced frequency*

# APPENDIX F

## PSDs motions

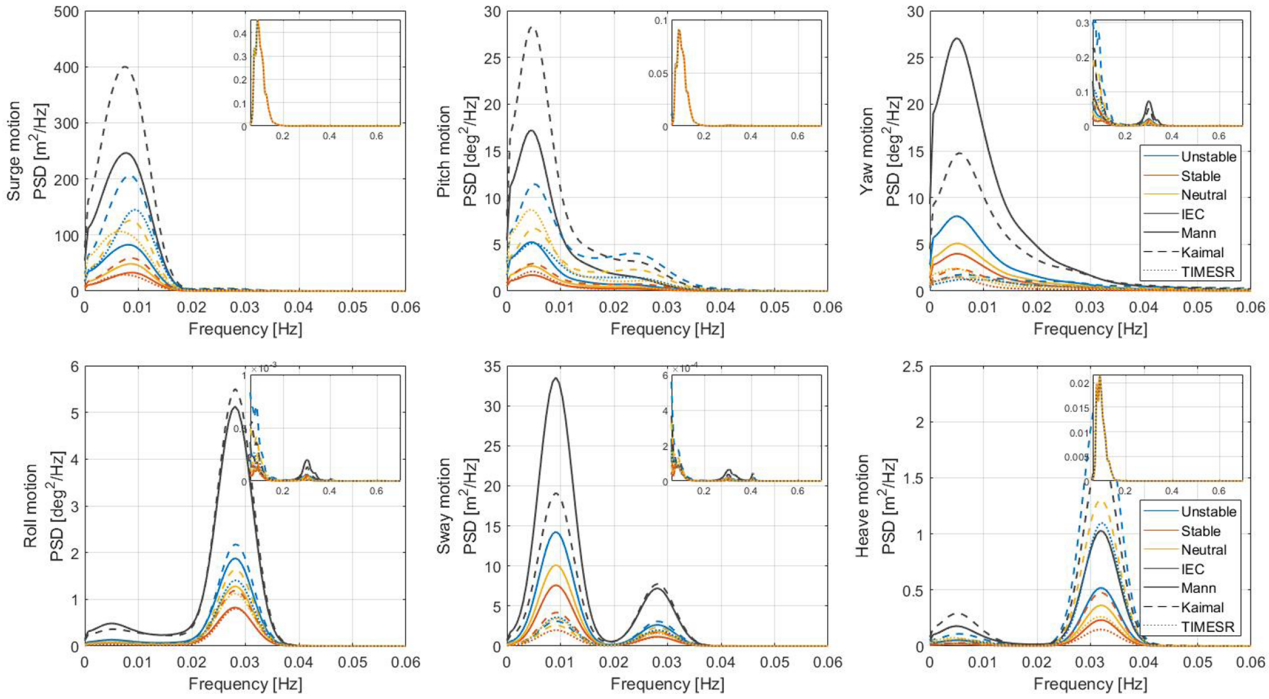


Figure F.1: *Platform motions PSDs at 7.5 m/s*

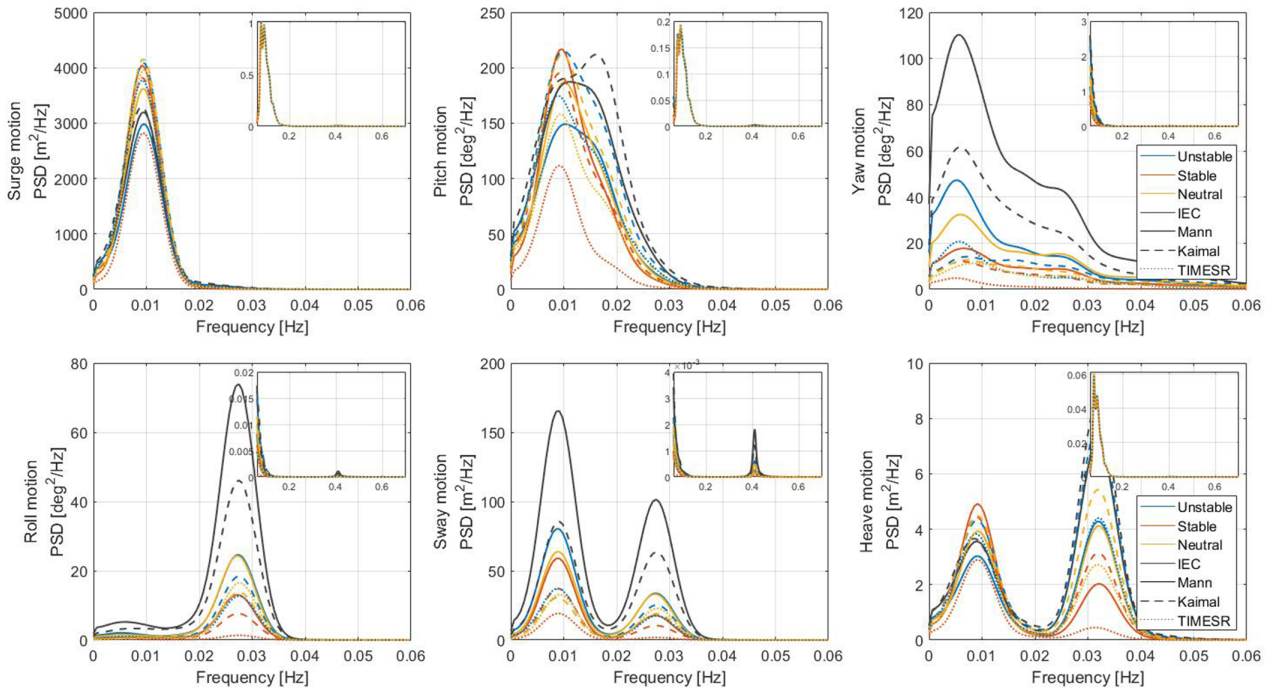


Figure F.2: *Platform motions PSDs at 12 m/s*

# APPENDIX G

## Platform motion percent differences for stability conditions

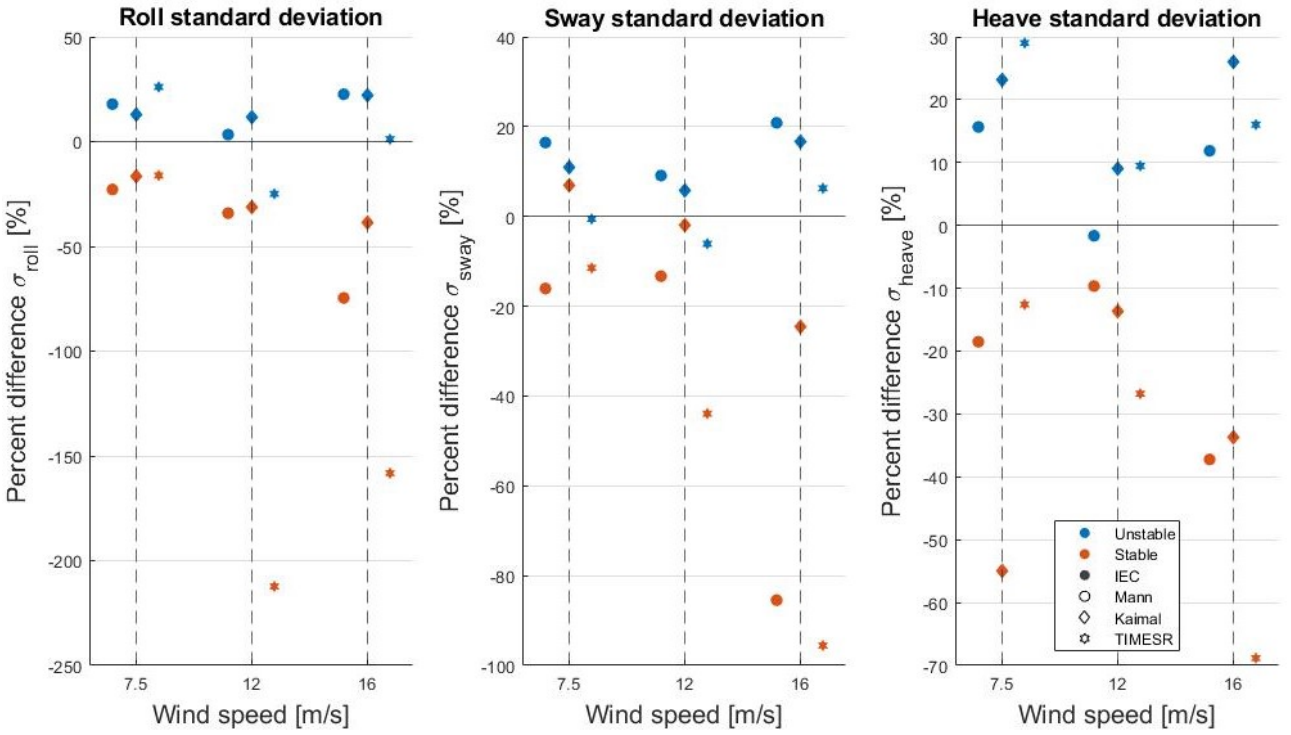


Figure G.1: *Platform roll, sway, and heave motion percent difference standard deviations between stability conditions and neutral conditions as a function of* $\overline{u}_{hub}$

# APPENDIX H

## Damage equivalent loads with filtering

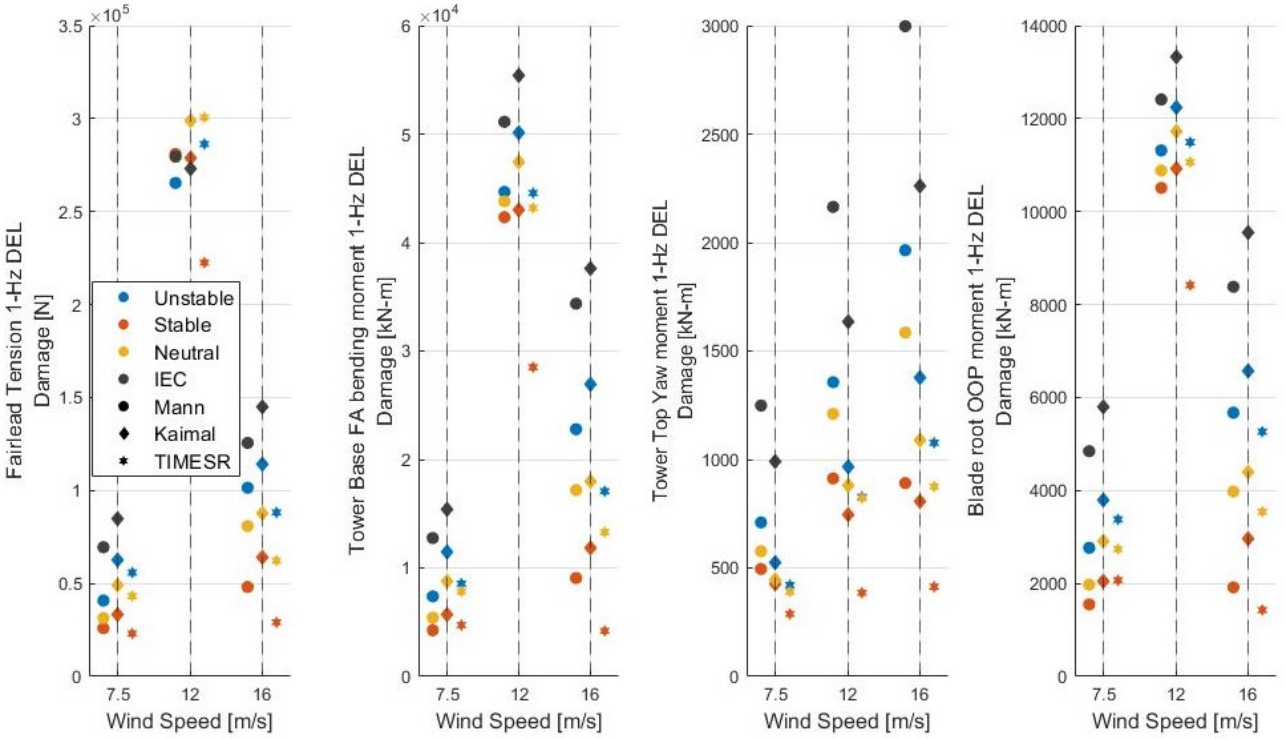


Figure H.1: *Damage-equivalent loads in the low frequency range as a function of* $\overline{u}_{hub}$

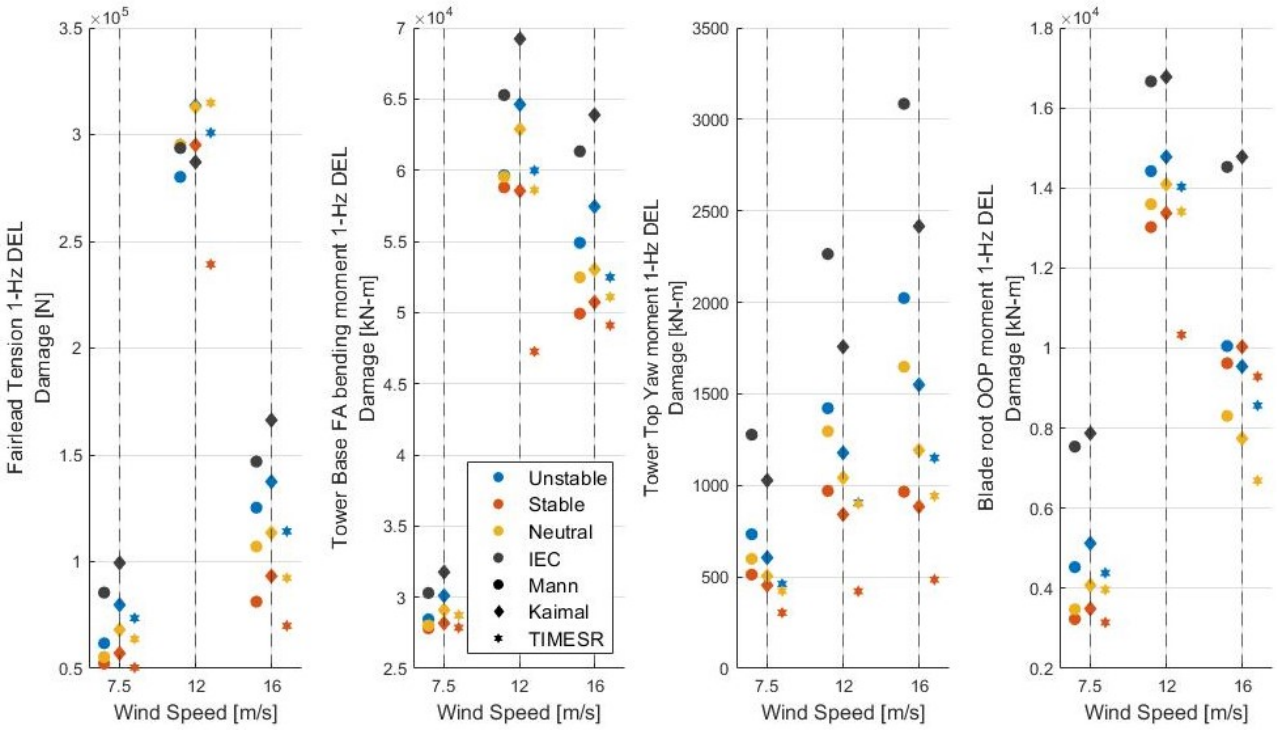


Figure H.2: *Damage-equivalent loads in the low frequency range plus the wave frequency as a function of* $\overline{u}_{hub}$

# Bibliography


[1] X. Wenfei, "Design , numerical modelling and analysis of a spar floater supporting the DTU 10MW wind turbine," no. June, pp. 1–109, 2016. [Online]. Available: core.ac.uk/download/pdf/154676062.pdf

[2] N. E. Komite, *IEC 61400-21-1:2019*, 2019.

[3] BSH, "FINO1 - research platform in the North Sea and the Baltic No. 1." [Online]. Available: https://www.fino1.de/en/

[4] NREL, "OpenFAST Documentation."

[5] G. J. Hayman, "MLife Theory Manual for Version 1.00," no. October, p. 12, 2012.

[6] C. Walsh, "Offshore wind in Europe," *Refocus*, vol. 3, no. 2, pp. 14–17, 2019. [Online]. Available: https://windeurope.org/wp-content/uploads/files/about-wind/statistics/WindEurope-Annual-Offshore-Statistics-2019.pdf

[7] v. F. Christoph, "Derivation of Trace Gas Information combining Differential Optical Absorption Spectroscopy with Radiative Transfer Modelling," 2003. [Online]. Available: https://www.researchgate.net/publication/33427973_Derivation_of_Trace_Gas_Information_combining_Differential_Optical_Absorption_Spectroscopy_with_Radiative_Transfer_Modelling

[8] E. L. Petersen, N. G. Mortensen, L. Landberg, J. Højstrup, and H. P. Frank, "Wind Power Meteorology," *Wind Energy*, vol. 1206, no. December, pp. 2–22, 1997. [Online]. Available: http://citeseerx.ist.psu.edu/viewdoc/download?doi=10.1.1.123.5357&rep=rep1&type=pdf

[9] M. Türk and S. Emeis, "The dependence of offshore turbulence intensity on wind speed," *Journal of Wind Engineering and Industrial Aerodynamics*, vol. 98, no. 8-9, pp. 466–471, 2010.

[10] IEC, "IEC 61400-21-3:2019."

[11] R. J. Barthelmie, M. J. Churchfield, P. J. Moriarty, J. K. Lundquist, G. S. Oxley, S. Hahn, and S. C. Pryor, "The role of atmospheric stability/turbulence on wakes at the Egmond aan Zee offshore wind farm," *Journal of Physics: Conference Series*, vol. 625, no. 1, 2015.

[12] A. Sathé, J. Mann, T. Barlas, W. A. A. M. Bierbooms, and G. J. W. van Bussel, "Influence of atmospheric stability on wind turbine loads," *Wind Energy*, vol. 16, pp. 1013–1032, 2013.

[13] J. M. Jonkman and M. L. Buhl, "Development and Verification of a Fully Coupled Simulator for Offshore Wind Turbines: Preprint," Tech. Rep., 2007. [Online]. Available: http://www.osti.gov/bridge

[14] A. S. Wise and E. E. Bachynski, "Wake meandering effects on floating wind turbines," *Wind Energy*, vol. 23, no. 5, pp. 1266–1285, 2020.

[15] DNV, "DNV-OS-J101 Design of Offshore Wind Turbine Structures," *May*, no. May, pp. 212–214, 2014.

[16] M. de Maré and J. Mann, "Validation of the Mann spectral tensor for offshore wind conditions at different atmospheric stabilities," *Journal of Physics: Conference Series*, vol. 524, p. 12106, 6 2014.

[17] B. Jonkman, "TurbSim CPU Times - NWTC." [Online]. Available: https://wind.nrel.gov/forum/wind/viewtopic.php?t=1168

[18] IRENA, *Renewable Energy Statistics 2020. Renewable hydropower (including mixed plants)*, 2020. [Online]. Available: www.irena.org

[19] "Hywind Scotland - equinor.com." [Online]. Available: https://www.equinor.com/en/what-we-do/floating-wind/hywind-scotland.html

[20] "Principle Power, Inc. - Globalizing floating wind," 2020. [Online]. Available: https://www.principlepowerinc.com/en/home/interactive-windfloat

[21] P. Doubrawa, M. J. Churchfield, M. Godvik, and S. Sirnivas, "Load response of a floating wind turbine to turbulent atmospheric flow," *Applied Energy*, vol. 242, pp. 1588–1599, 5 2019.

[22] A. Jacobsen and M. Godvik, "Influence of wakes and atmospheric stability on the floater responses of the Hywind Scotland wind turbines," *Wind Energy*, vol. 24, no. 2, pp. 149–161, 2021.

[23] E. E. Bachynski and L. Eliassen, "The effects of coherent structures on the global response of floating offshore wind turbines," *Wind Energy*, vol. 22, no. 2, pp. 219–238, 2019.

[24] M. Godvik, "Influence of wind coherence on the response of a floating wind turbine Background I," Tech. Rep.

[25] A. Peña, S. E. Gryning, and J. Mann, "On the length-scale of the wind profile," *Quarterly Journal of the Royal Meteorological Society*, vol. 136, no. 653, pp. 2119–2131, 2010.

[26] A. Nybø, F. G. Nielsen, J. Reuder, M. J. Churchfield, and M. Godvik, "Evaluation of different wind fields for the investigation of the dynamic response of offshore wind turbines," *Wind Energy*, vol. 23, no. 9, pp. 1810–1830, 2020.

[27] E. Cheynet, "Numerical implementation of the uniform-shear model by Mann (1994)." [Online]. Available: https://github.com/ECheynet/MannModel1994

[28] L. Eliassen and C. Obhrai, "Coherence of Turbulent Wind Under Neutral Wind Conditions at {FINO}1," *Energy Procedia*, vol. 94, pp. 388–398, 9 2016.

[29] M. H. Myrtvedt and A. N. F. G. Nielsen, "The dynamic response of offshore wind turbines and their sensitivity to wind field models," *Journal of Physics: Conference Series*, vol. 1669, p. 12013, 10 2020.

[30] "Atmospheric Science - 2nd Edition." [Online]. Available: https://www.elsevier.com/books/atmospheric-science/wallace/978-0-12-732951-2

[31] G. North, J. Pyle, and F. Whang, "Encyclopedia of Atmospheric Sciences - 2nd Edition," 2014. [Online]. Available: https://www.elsevier.com/books/encyclopedia-of-atmospheric-sciences/north/978-0-12-382225-3

[32] A. M. Obukhov, "Turbulence in an atmosphere with a non-uniform temperature," *Boundary-Layer Meteorology*, vol. 2, no. 1, pp. 7–29, 1971.

[33] S. E. Gryning, E. Batchvarova, B. Brümmer, H. Jørgensen, and S. Larsen, *On the extension of the wind profile over homogeneous terrain beyond the surface boundary layer*, 2007, vol. 124, no. 2.

[34] D. Norske Veritas, "RECOMMENDED PRACTICE ENVIRONMENTAL CONDITIONS AND ENVIRONMENTAL LOADS," Tech. Rep., 2010. [Online]. Available: http://www.dnv.com

[35] C. Obhrai, S. Kalvig, and O. T. Gudmestad, "A review of current guidelines and research on wind modeling for the design ofoffshore wind turbines," *Boundary-Layer Meteorology*, 2012.

[36] D. Golder, "Relations among stability parameters in the surface layer," *Boundary-Layer Meteorology*, vol. 3, no. 1, pp. 47–58, 9 1972. [Online]. Available: http://link.springer.com/10.1007/BF00769106

[37] S. E. Larsen, S. E. Gryning, N. O. Jensen, H. E. Jorgensen, and J. Mann, "Mean Wind and Turbulence in the Atmopsheric Boundary Layer," 2007.

[38] R. Stull, "An Introduction to Boundary Layer Meteorology," 1988. [Online]. Available: https://www.springer.com/gp/book/9789027727688

[39] R. M. Harrison, Ed., *Pollution*. Cambridge: Royal Society of Chemistry, 2007. [Online]. Available: http://ebook.rsc.org/?DOI=10.1039/9781847551719

[40] J. Twidell and G. Gaudiosi, "Offshore Wind Power," *Wind Engineering*, vol. 34, no. 1, pp. 123–123, 1 2010.

[41] A. N. F. G. Nielsen, J. Reuder, M. J. Churchfield, and M. Godvik, "Evaluation of different wind fields for the investigation of the dynamic response of offshore wind turbines," *Wind Energy*, vol. 23, no. 9, pp. 1810–1830, 5 2020.

[42] C. Obhrai, J. Jakobsen, and R. Putri, "Uncertainties in Turbulent Wind Modelling for Floating Offshore Wind Turbines," 2020.

[43] J. C. Kaimal, J. C. Wyngaard, Y. Izumi, and O. R. Coté, "Spectral characteristics of surface□layer turbulence," *Quarterly Journal of the Royal Meteorological Society*, vol. 98, no. 417, pp. 563–589, 1972.

[44] J. Mann, "Wind field simulation," *Probabilistic Engineering Mechanics*, vol. 13, no. 4, pp. 269–282, 1998.

[45] ——, "The Spatial Structure of Neutral Atmospheric Surface-Layer Turbulence," *Journal of Fluid Mechanics*, vol. 273, pp. 141–168, 1994.

[46] DTU, "Mann 64bit turbulence generator." [Online]. Available: https://www.hawc2.dk/Download/Pre-processing-tools/Mann-64bit-turbulence-generator

[47] A. S. Chougule, "Influence of atmospheric stability on the spatial structure of turbulence," 2013.

[48] B. J. Jonkman, "TurbSim user's guide v2.00.00," *National Renewable Energy Laboratory*, no. October 2014, p. 103, 2016. [Online]. Available: www.nrel.gov/publications

[49] K. Saranyasoontorn, L. Manuel, and P. S. Veers, "A Comparison of Standard Coherence Models for Inflow Turbulence With Estimates from Field Measurements," *Journal of Solar Energy Engineering*, vol. 126, no. 4, pp. 1069–1082, 11 2004.

[50] A. Robertson, L. Sethuraman, J. Jonkman, and J. Quick, "Assessment of Wind Parameter Sensitivity on Ultimate and Fatigue Wind Turbine Loads," Tech. Rep., 2018. [Online]. Available: http:/www.osti.gov/scitech

[51] A. G. Davenport, "The spectrum of horizontal gustiness near the ground in high winds," *Quarterly Journal of the Royal Meteorological Society*, vol. 87, no. 372, pp. 194–211, 4 1961.

[52] E. Cheynet, "The parameters of the Uniform Shear Model are estimated in the least-square sense." [Online]. Available: https://github.com/ECheynet/fitMann1994

[53] W. Yu, K. Müller, and F. Lemmer, "D4.2 Public Definition of the Two LIFES50+ 10MW Floater Concepts," pp. 1–105, 2018.

[54] J. M. Jonkman and D. Matha, "Dynamics of offshore floating wind turbines-analysis of three concepts," *Wind Energy*, vol. 14, no. 4, pp. 557–569, 5 2011. [Online]. Available: http://doi.wiley.com/10.1002/we.442

[55] R. M. Putri, C. Obhrai, and J. M. Knight, "Offshore Wind Turbine Loads and Motions in Unstable Atmospheric Conditions," *Journal of Physics: Conference Series*, vol. 1356, no. 1, 2019.

[56] C. Bak, "The DTU 10-MW Reference Wind Turbine," *DTU*, 2013.

[57] T. J. Larsen and T. D. Hanson, "A method to avoid negative damped low frequent tower vibrations for a floating, pitch controlled wind turbine," *Journal of Physics: Conference Series*, vol. 75, no. 1, 2007.

[58] J. Jonkman, "Definition of the Floating System for Phase IV of OC3," no. May, p. 31, 2010. [Online]. Available: http://www.osti.gov/bridge

[59] L. Li, Z. Gao, and T. Moan, "Joint Environmental Data At Five European Offshore Sites for," *32nd International Conference on Ocean, Offshore and Artic Engineering*, pp. 1–12, 2013.

[60] Fraunhofer IWES, "RAVE: Research at alpha ventus." [Online]. Available: https://www.rave-offshore.de/en/start.html

[61] A. Nybø, A. Nielsen, and J. Reuder, "Processing of sonic anemometer measurements for offshore wind turbine applications," *Journal of Physics: Conference Series*, vol. 1356, p. 12006, 10 2019.

[62] E. Cheynet, . J. B. Jakobsen, J. Snaebjörnsson, H. ⊠. Agústsson, and K. Harstveit, "Complementary use of wind lidars and land-based met-masts for wind measurements in a wide fjord," Tech. Rep.

[63] J. M. Wilczak, S. P. Oncley, and S. A. Stage, "Sonic anemometer tilt correction algorithms," *Boundary-Layer Meteorology*, vol. 99, no. 1, pp. 127–150, 2001.

[64] E. Cheynet, J. B. Jakobsen, and J. Reuder, "Velocity Spectra and Coherence Estimates in the Marine Atmospheric Boundary Layer," *Boundary-Layer Meteorology*, vol. 169, no. 3, pp. 429–460, 8 2018.

[65] S. Emeis and M. Turk, "Comparison of Logarithmic Wind Profiles and Power Law Wind Profiles and their Applicability for Offshore Wind Profiles," in *Wind Energy*. Berlin, Heidelberg: Springer Berlin Heidelberg, 2007, pp. 61–64. [Online]. Available: http://link.springer.com/10.1007/978-3-540-33866-6_11

[66] P. D. Welch, "The Use of Fast Fourier Transform for the Estimation of Power Spectra: A Method Based on Time Averaging Over Short, Modified Periodograms," *IEEE Transactions on Audio and Electroacoustics*, vol. 15, no. 2, pp. 70–73, 1967.

[67] A. Nybø, F. G. Nielsen, and M. Godvik, "Analysis of turbulence models fitted to site , and their impact on the response of a bottom fixed wind turbine," 2021.

[68] G. I. Taylor, "The Spectrum of Turbulence," *Proceedings of the Royal Society A: Mathematical, Physical and Engineering Sciences*, vol. 164, no. 919, pp. 476–490, 2 1938. [Online]. Available: https://royalsocietypublishing.org/doi/10.1098/rspa.1938.0032

[69] P. S. Veers, "Three-dimensional wind simulation." no. January, 1988.

[70] M. I. Kvittem and T. Moan, "Time domain analysis procedures for fatigue assessment of a semi-submersible wind turbine," *Marine Structures*, vol. 40, pp. 38–59, 1 2015.

[71] P. Brodtkorb, P. Johannesson, G. Lindgren, I. Rychlik, J. Rydén, and E. Sjö, "WAFO - a Matlab toolbox for analysis of random waves and lods," in *10th International Offshore and Polar Engineering conference*, Seattle, 2000, pp. 343–350.

[72] G. J. Hayman and M. Buhl, "MCrunch User's Guide MLife User's Guide for Version 1.0," no. October, 2012. [Online]. Available: http://www.osti.gov/bridge

[73] S. Davoust and D. Von Terzi, "Analysis of wind coherence in the longitudinal direction using turbine mounted lidar," in *Journal of Physics: Conference Series*, vol. 753, no. 7. Institute of Physics Publishing, 10 2016, p. 072005. [Online]. Available: https://iopscience.iop.org/article/10.1088/1742-6596/753/7/072005https://iopscience.iop.org/article/10.1088/1742-6596/753/7/072005/meta

[74] K. Saranyasoontorn, L. Manuel, and P. S. Veers, "A comparison of standard coherence models for inflow turbulence with estimates from field measurements," *Journal of Solar Energy Engineering, Transactions of the ASME*, vol. 126, no. 4, pp. 1069–1082, 11 2004. [Online]. Available: http://asmedigitalcollection.asme.org/solarenergyengineering/article-pdf/126/4/1069/5626604/1069_1.pdf

[75] H. A. Panofsky and I. A. Singer, "Vertical structure of turbulence," *Quarterly Journal of the Royal Meteorological Society*, vol. 91, no. 389, pp. 339–344, 7 1965. [Online]. Available: http://doi.wiley.com/10.1002/qj.49709138908

[76] N. Dimitrov, A. Natarajan, and J. Mann, "Effects of normal and extreme turbulence spectral parameters on wind turbine loads," *Renewable Energy*, vol. 101, pp. 1180–1193, 2 2017.

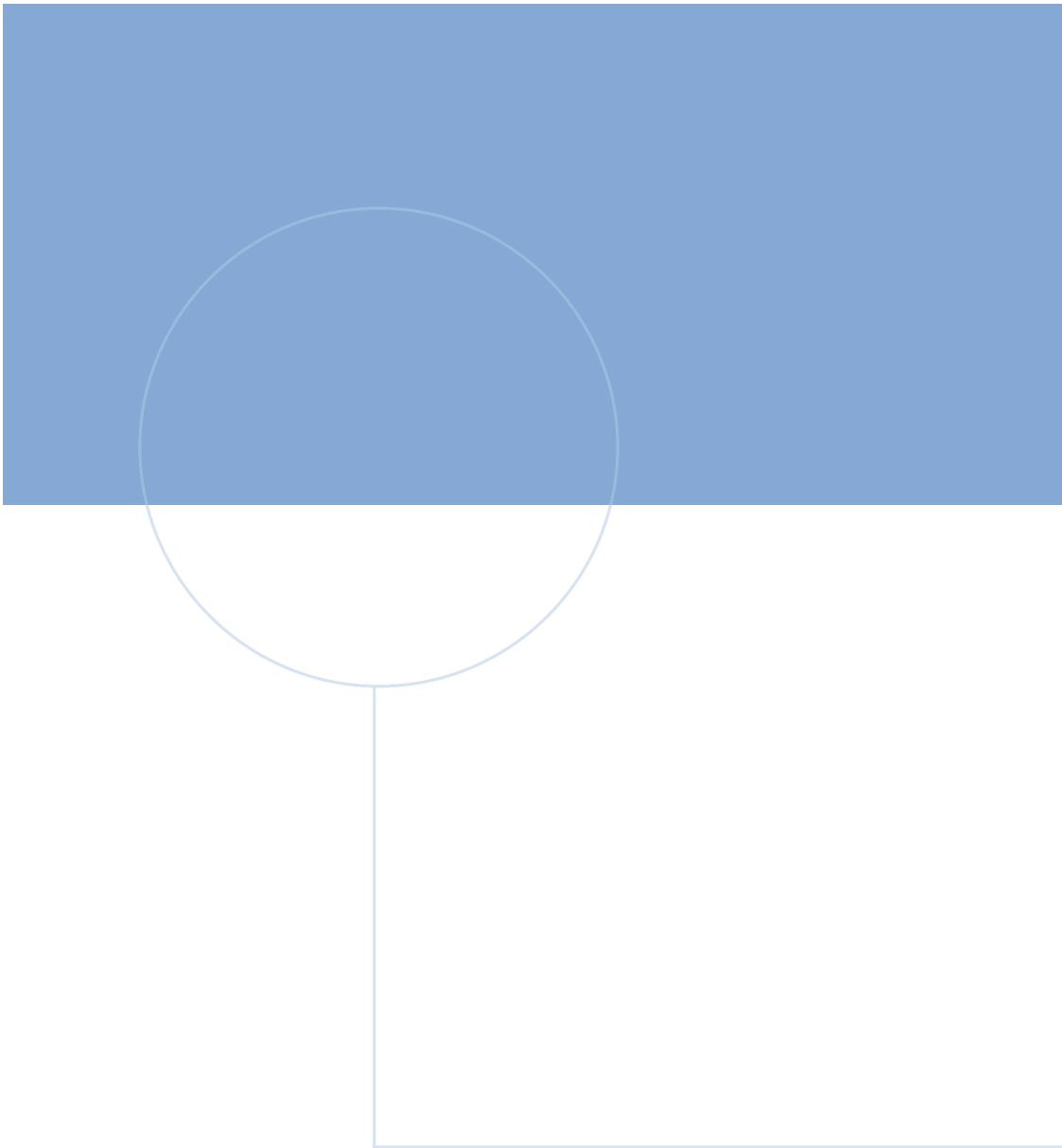

NTNU
Norwegian University of
Science and Technology

TU Delft
Delft University of Technology